Nanoparticle-membrane interactions

Inaugural-Dissertation

zur

Erlangung des Doktorgrads

der Mathematisch-Naturwissenschaftlichen Fakultät

der Universität zu Köln

vorgelegt von

Qingfen Yu

aus Guangdong, China

Jülich 2017

Berichterstatter: Prof. Dr. Gerhard Gompper
(Gutachter)

Prof. Dr. Jan K. G. Dhont

Tag der mündlichen Prüfung: 15 Dezember 2017

Abstract

Biologische Membranen sind dünne, flüssige Filme, die aus Lipidmolekülen, Proteinen, und Zuckern aufgebaut sind. Vesikelbildung ist wichtig für den Materialtransport zwischen den Organellen und der Plasmamembran in biologischen Zellen. Nanopartikel sind eine spezielle Art von Material, das mit kontrollierter Struktur, Zusammensetzung und physikochemikalischen Oberflächeneigenschaften hergestellt werden kann. Nanoteilchen können über Membranen durch Endozytose und Exozytose transportiert werden. Die genauen mechanischen Mechanismen hierbei sind jedoch noch nicht komplett verstanden. In der Literatur ist bekannt, dass das Einwickeln von Nanoteilchen durch Lipidmembranen durch Größe, Form und den Oberlflächeneingenschaften der Teilchen, sowie durch die biophysikalischen Eigenschaften der Membran bestimmt wird. Für gekrümmte Membranstrukturen, z. B. Vesikel und Röhren, wird das Einwickeln auch stark durch die Membrankrümmung vor der Wechselwirkung mit dem Teilchen beeinflußt. In ähnlicher Weise beeinflußt die Membrandeformation durch teilweise eingewickelte Teilchen in der Nähe das Einwickeln eines Nanoteiclhens. Desweiteren ist in der Literatur bekannt, dass teilweise eingewickelte Nanoteilchen sich, durch die Membrandeformation vermittelt, gegenseitig anziehen.

In dieser Arbeit wird die Membran durch eine mathematische Fläche beschrieben, deren krümmungselastische Eigenschaften mit Hilfe des Helfrich-Modells berechnet werden. Die Biegesteifigkeit, das Gauß'sche Biegemodul, und die spontane Membrankrümmung sind die Materialparameter der Membran. Das Modell kann Membranen auf Mikrometerskalen beschreiben, auf denen die molekularen Eigenschaften der Lipidmoleküle nicht mehr direkt berücksichtigt werden müssen. In dieser Arbeit wird die Deformationsenergie numerisch mit Hilfe von triangulierten Flächen berechnet, auf der Grundlage der beiden Hauptkrümmungen in jedem Punkt der Fläche.

Für Nanoteilchen an nicht kugelförmigen Vesikeln wurde die Rolle der Teilchen-größe, der Vesikelgröße, der Vesikelform, und der spontanen Krümmung der Membran für das Einwickeln der Teilchen und die Vesikelform systematisch untersucht. Für die Stomatozyten, Oblaten und Prolaten ist nicht nur die lokale Membran-krümmung an dem Punkt wichtig an dem das Teilchen bindet, sondern auch die Krümmungsenergie der freien Membran. Bei gegebenem

Vesikelvolumen und Membranfläche, wird komplexes Einwickelverhalten, bei dem das Einwickeln der Teilchen und die Form der Vesikel sich gegenseitig beinflussen, beobachtet. Insbesondere stabilisieren teilweise eingewickelte Teilchen oblate und stomatozyte Vesikelformen für Teilchen, die von außen an die Membran binden, und prolate und stomatozyte Formen für Teilchen, die von innen an die Membran binden. Wenn sich das Vesikelvolumen während des Einwickeln von Teilchen verändern kann, führt das Vorhandensein von gelösten Stoffen sowohl im innern als auch außerhalb des Vesikel zu einem Kompressionsenergiebeitrag zur Vesikeldeformationsenergie. Die Kompressionsenergie stabilisiert teilweise eingewickelte Teilchenzustände, sowohl für Nanoteilchen innerhalb als auch außerhalb der Vesikel. Bei hohen Konzentrationen der Lösungen wride der Übergang zwischen dem teilweise und dem vollständig eigewickeltem Zustand diskontinuerlich. Abschließend werden Systeme mit Teilchen und Membranröhren untersucht. In diesem Fall werden sowohl die Einwickel-Übergänge, als auch die membran-vermittelte Wechselwirkung zwischen zwei teilweise eingewickelten Teilchen berechnet. Im Gegensatz zur Literatur wird sowohl eine anziehende als auch eine abstoßende Wechselwirkung zwischen den Teilchen gefunden, abhängig vom Teilchenabstand und von der Adhäsionsstärke zwischen den Teilchen und der Membran.

Die Ergebnisse dieser Arbeit tragen zum besseren Verständnis der mechanischen Mechanismen beim Einwickeln von Nanoteilchen durch Lipidmembranen bei. Insbesondere wurden die Einwickelübergänge der Teilchen, die Formveränderungen der Vesikel und membran-vermittelte Wechselwirkungen zwischen Teilchen für stark gekrümmte Membranen berechnet. Solche Strukturen sind inzwischen durch verbesserte Mikroskopietechniken experimentell beobachtbar und wurden in verschiedenen Bereichen biologischer Zellen gefunden.

Abstract

Biological membranes are fluid thin films composed of lipids, proteins and sugars. They participate in cargo trafficking between membrane-bounded organelles and the plasma membrane via budding and vesicle formation. Nanoparticles are one specific nano-scale cargo that can be engineered with controlled structure, composition, and physicochemical surface properties. They can be transported across a membrane by endocytosis and exocytosis. However, the mechanical mechanisms for nanoparticle-membrane interactions are still debated. Previous studies show that nanoparticle wrapping by membranes depends on nanoparticle size, shape, and surface functionalisation, as well as the membranes' biophysical properties. For highly-curved membrane structures, such as vesicles and tethers, nanoparticle wrapping is strongly dependent on the membrane curvature prior to wrapping. Similarly, wrapping is affected by the membrane deformations due to nearby partial-wrapped nanoparticles, and partial-wrapped nanoparticles have been reported to mutually attract each other via membrane deformation.

The membrane is described as a mathematical surface and use the continuum membrane model based on the Helfrich Hamiltonian to characterize its mechanical properties. Here, the curvature-elastic properties of the membrane are characterized using three material parameters, the bending rigidity, the spontaneous curvature, and the Gaussian saddle-splay modulus. The model can describe membranes on large scales up to micrometers, where molecular details can be neglected. In this thesis, the membrane deformation energy for nanoparticle-wrapping is calculated numerically using triangulated membranes based on the principal curvatures of the surface at every point.

For the interaction of nanoparticles with non-spherical vesicles, the role of particle size, vesicle size and shape, and membrane spontaneous curvature on both nanoparticle wrapping and vesicle shape is studied. For non-spherical vesicle shapes, such as stomatocytes, oblates, and prolates, not only the local curvature at the point where the particle attaches but also the deformation energy of the free membrane is important. For fixed vesicle volume and membrane area, complex wrapping behavior, where particle wrapping transitions and vesicle shape transitions can be coupled, is found. Furthermore, partial-wrapped membrane-bound particles impose boundary conditions for

the free membrane that stabilize oblates and stomatocytes for particle entry, and prolates and stomatocytes for particle exit. If the vesicle volume can vary upon nanoparticle wrapping, the presence of solute inside the vesicle gives rise to a compression energy contribution to the vesicle deformation energy. For the first time, an osmotic pressure contribution is taken into account for nanoparticle-wrapping calculations. The deformation-induced osmotic pressure difference stabilizes partial-wrapped states for both nanoparticles entering and exiting vesicles. For high solute concentrations, the transition between the partial-wrapped and the complete-wrapped state becomes discontinuous. Finally, wrapping of nanoparticles at membrane tubes is investigated. Here, both wrapping transitions and membrane-mediated particle-particle interactions are studied. Contrary to the literature, both mutual attraction and repulsion between nanoparticles are observed, depending on their separation and on the adhesion strength between the nanoparticle and the membrane.

The results presented in this thesis contribute to the understanding of mechanical mechanisms for membranes wrapping nanoparticles. In particular, wrapping transitions, shape transitions, and membrane-mediated iterations between partial-wrapped nanoparticles are predicted for highly-curved membrane structures. Such structures recently became experimentally observable due to improved microscopy techniques, and have been found to be abundant in biological cells.

Contents

Chapter 1

Introduction

1.1 Motivation

Nanoparticles are colloidal particles with sizes on the nanometer scale. They are ubiquitous in both natural and artificial environments. A lot of familiar examples of nanoparticles are found around us, including viruses and proteins [1], inorganic nanoparticles (e.g., titanium dioxide (TiO_2)) in sunscreens and paints [2], and silica nanoparticles used as solid lubricants [2]. In many cases, the shapes or structures are single crystals with platonic shapes (cubes, octahedra, and spheres), and spherical or ellipsoidal. They also have more complicated architectures, including the so-called "lamellar twinned particles" (LTPs) or "Multiply-Twinned Particles" (MTPs) containing two, five or twenty single crystal units, and icosahedral, decahedral, and more complex "polyparticles" with polyicosahedral structures [3]. In addition to different components, sizes, and shapes, specific physicochemical properties of nanoparticles including optical, electronic, mechanical and surface properties play an important role in their applications [4].

With their well-controlled properties, engineered nanoparticles can be used for diagnostic and therapeutic applications, for example, they are candidates for drug delivery systems, as well as for tumor-cell targeting [4–6]. The first essential step for nanoparticles function in human bodies is the interactions of nanoparticles with the membranes of vesicles and cells. Biological membranes are very fluid films with thicknesses of $4-5\,\mathrm{nm}$. For cellular membranes, such fluid films are composed of amphipathic lipid molecules, various proteins, and carbohydrates. These components assemble according to the so-called "Fluid-Mosaic Membrane Model (F-MMM)" [7] for plasma membranes, in which the proteins are either embedded in or floated on the amphipathic lipid bilayer, and carbohydrates facilitate the connections of lipids and proteins to cellular matrix and cytoskeleton. Biological membranes display specific mechanical properties, such as bending, stretching, and shape elasticity [8]. The important

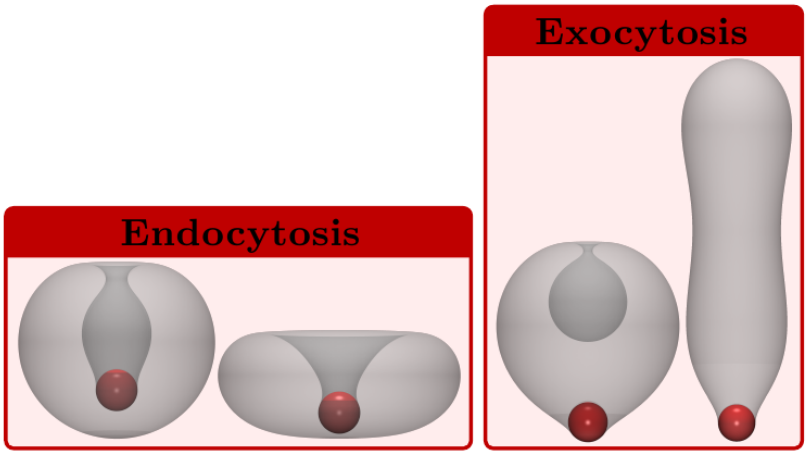

Figure 1.1: Spherical nanoparticles (red) entering and exiting vesicles (gray) via endocytosis and exocytosis. The shapes for the vesicles from left to right are stomatocyte, oblate, stomatocyte, and prolate.

functions for biological membranes are to separate different environment and to control the cargo trafficking across the membranes to maintain the balance of cellular environments. In general, cargoes like drug-loaded nanoparticles can translate through membranes via endocytosis and exocytosis [9, 10], see Fig. 1.1. These processes in biological cells are usually very complicated, and can be affected by a large numbers of factors including active processes.

For large nanoparticles with sizes above 15 nm, a thorough investigation of nanoparticle translocation by wrapping is required for understanding membrane-associated nanoparticle transport. A large amount of theoretical [11–13], computational [14–16], and experimental [17, 18] studies have focused on this challenging topic, but the mechanical mechanisms are still not well understood, as wrapping and adhesion of nanoparticles at membrane depend on a multitude parameters, such as components and the structure of the membrane, as well as on the solutions properties. Here we use the continuum model based on the Helfrich Hamiltonian [19, 20] to investigate the engulfment of nanoparticles by membranes, for which a large number of biophysical details can be ignored. We consider the elastic energies and deformation shapes associated with nanoparticle uptake by membranes, in order to reveal the mechanical mechanisms for nanoparticle-membrane interactions. We aim at providing some meaningful predictions for more efficient and less toxic nanoparticle transport via membrane budding.

1.2 Membranes

Biological membranes are extremely fascinating soft matter systems. Different from the rigid surfaces, they are fluid and can form specific structures, such as enclosed vesicles with different shapes, see Fig. 1.1. The shapes result from the biochemical components of the membrane and properties of its environment. For membrane formation, lipid molecules aggregate spontaneously into "leaflets" where the molecules are jointed together by the weak non-covalent forces. These bilayers are able to extend in the lateral dimensions of up to 10 micrometers, which is considerably larger than the thickness of the membrane of only a few nanometers [7, 21, 22]. The big variation in the length scale allows us to regard the biological membrane as two-dimensional surface embedded in three-dimensional space. Here, detailed biophysical characteristics are negligible. These flexible membranes are controlled by their properties on the mesoscale; we particularly focus on their elastic properties for the membrane deformations, such as thickness change, shearing, stretching, bending. Other important physical aspects regarding the geometric shapes of the membranes are also introduced briefly.

1.2.1 Composition

Biological membranes are composed of lipids and proteins [7, 23]. The lipids are amphiphilic molecules that consist of a polar hydrophilic head group and a non-polar hydrophobic tail. In cell membranes, different lipids are found, such as phospholipids, glycolipids, and other sterols. Depending on the types of cells and organelles, the fractions of each lipid can be varied. The most abundant lipid constituents are phospholipids in most biological membranes. The phospholipids in a cell include phosphatidic acid (phosphatidate) (PA), phosphatidylcholine (lecithin) (PC), phosphatidylethanolamine (cephalin) (PE), phosphatidylserine (PS), phosphatidylinositol (PI), sphingomyelin (SM), cardiolipin (CL) [23, 24], see Tab. 1.1.

The phospholipids are different from each other relying upon the hydrocarbon tail length, i.e., the number of carbon atoms in tails, and the saturation, i.e., the presence of carbon-carbon double bonds [25]. PC is a lipid with a cylindrical shape, for which the volumes for the head and the tail groups are approximately the same. For PE, the tail part area is larger compared to the head part, therefore the lipid displays a conical shape. PA has an inverse conical shape as the lipids have large tail and small head moieties.

Furthermore, phospholipids with different head groups are able to influence the chemical properties of the leaflet surface, and to execute various functions in the cells [23–25]. For instance, PC is a key component for membrane-mediated cell signaling and molecule transport; PE plays an important role in membrane fusion, as well as in regulating the membrane curvature. PA

Compartment	Plasmamembrane		Endoplasmatic Reticulum	Golgi	Lysosome	Nuclear Membrane	Mito-chondria	Nerve Cells	
Lipid	human erythrocyte	rat liver						Neurons[5]	Myelin[6]
phosphatidyl-cholin	20	18	48	25	23	44	38	48	11
phosphatidy-ethanolamine	18	12	19	9	13	17	29	21	17
phosphatidyl-serine	7	7	4	3		4	0	5	9
phosphatidyl-inositol	3	3	8	5	6	6	3	7	1
sphingomyelin	18	12	5	7	23	3	0	4	8
cardiolipin	—	—	—	—	≈ 5	1	14	—	—
glycolipid	3	8	traces	0		traces	traces	3	20[7]
others	11	21[1]	10[2]	43[3]	16[4]	15	13	1	6
cholesterol	20	19	6	8	14	10	3	11	28

Footnotes: [1]These include 6% free fatty acid, 2.5% lyso PC, 2.5% cholesterol esters, 7% triglycerides.
[2]These include 5% triglycerides.
[3]These include 10% triglycerides, 18% free fatty acid and 5% cholesterol esters.
[4]These include 3% triglycerides and 8% cholesterol esters.
[5]Average lipid composition of rat brain neurons.
[6]Bovin brain myelin.
[7]Essentially ceramides.

Table 1.1: A summary of lipid compositions of various organelles, plasma membranes, and cells. Reprinted from Ref. [23].

is important for both membrane signaling and regulating curvature. Similar to the heads, hydrocarbon tails with different structures can also change the membrane properties. One example is unsaturated lipids that increase the fluidity of lipid bilayers [26].

In addition to lipid molecules, biological membranes contain a variety of proteins. Around $20-30\%$ of the biological genes encode such membrane proteins [27, 28]. The considerable advancements in the experimental methodology for structural biology, such as X-ray diffraction, solution nuclear magnetic resonance (NMR), and, more recently, single-particle cryo-electron microscopy (cryo-EM), or electron cryomicroscopy, lead to high-resolution structures of the membrane proteins [29, 30]. There are over $2,500$ protein structures stored in the protein data base (PDB), and they are divided into over 700 different protein species [30].

One important species of the membrane proteins are those that generate and regulate membrane curvature, and they are therefore involved in the changes of membrane shapes and even in topological changes like creation of the pores [31, 32]. These proteins can be classified into two different groups; one group can change the lipid composition of the two leaflets to induce the asymmetry of the membrane, such as the phospholipid flippase and the lipid modifying enzymes [31, 33]. The other group generates and sustains the membrane curvature by the mechanical interactions between the proteins and membrane monolayer [31]. Relying on the diverse qualitative features, the curvature-associated mechanisms [31, 32, 34], which are not mutually exclu-

sive, include:

(a) protein scaffolding [35]: the protein domain, the protein monomer or oligomer, and even multiple proteins with an intrinsic curvature aggregate on the membrane and bend the underlying membrane surfaces facing them;

(b) hydrophobic insertion [36]: the protein stabilizes the membrane curvature by virtue of the insertion of the hydrophobic residues into the local domains in amphipathic lipid molecules. The insertion process of the proteins are also known as "wedging";

(c) oligomerization [35, 36]: specific proteins, instead of generating and regulating the membrane curvature individually, can oligomerize to form the polymerized coat proteins linked to the outer monolayer. The cooperativity of the oligomerized proteins can amplify curvature sorting on membranes with different curvatures.

(d) steric effects [37]: the steric protein-protein interactions are found for proteins which have no intrinsic curvature effects, such as scaffolding effects, membrane-inserting domains, and ligomerization properties. They are crowed in the local membrane and induce the curvature by mutual steric interactions.

A large variety of membrane curvature-associated proteins are found experimentally. The most-widely studied proteins are Bin-Amphiphysin-RVs (BAR) domain-containing proteins [35–37]. BAR domains have banana shapes and bind to the membrane through the concave surface of the lipid-binding regions. They are found to induce the cylindrical curvature. The BAR protein family is further subclassified into classical BAR, N-BAR, F-BAR, and other BAR proteins relying upon the detailed structures. N-BAR proteins contribute to the membrane-curvature via the scaffolding mechanism, while F-BAR proteins are characterized by the hydrophobic insertion region and can induce membrane tubulation upon binding. Classical BAR proteins, such as arfaptin, can also form the highly-curved tubular membrane without hydrophobic insertion. Furthermore, both N-BAR and F-BAR domain proteins can oligomerize on curved membranes and result in the striated, attice-like protein coats on the bilayers. For crowding eripheral proteins, they can sence and regulate membrane bending via the nonspecific steric interactions. Other membrane-curvature associated proteins include coat protein complex I (COPI) and II (COPII), epsin N-terminal homology (ENTH) and AP180 N-terminal homology (ANTH) domain-containing proteins, small G proteins such as Arf1, and C2 domain proteins [35–37].

In addition to the mechanisms mentioned above, the interactions between membrane and specific lipids, the "packing defects" in curved lipid bilayers [38], the demixing of lipid molecules with various spontaneous membrane curvatures [39], and cytoskeletal polymerization and motor proteins pulled tubules are suggested to explain the formation and stability of the membrane curvatures [36]. Despite the various studies and theories on membrane curvature, the

relative significance of the potential contributions from different mechanisms is still hotly debated.

A third important component is the carbohydrates. Membrane carbohydrates contribute $5 - 10\%$ to the membrane mass. Most of them are located on the the extracellular side of the cell membrane and bind to the lipids and proteins via glycosylation [40]. Glycosylation is a common chemical reaction in cell in which a carbohydrate is covalently linked to the functional group of the membrane molecules. After such a chemical modification, the resulting components are called glycoconjugate, including oligosaccharides, proteoglycans, glycolipids and glycoproteins [41]. The neutral sugars in cells are glucose, galactose, mannose, fucose, as well as N-acetyl galactosamine, and they are abundant in the glycoconjugates [41, 42].

1.2.2 Structure

After the comprehensive understanding in the membrane components, a natural question is what a whole structure these different component can arrange into. The structure must be capable to explain the existing research data, such as fluidity and dynamics of the membrane, and to predict the outcomes for future experiments. In 1972, S. J. Singer and G. L. Nicolson first introduced the Fluid-Mosaic Membrane Model (F-MMM) of biological membrane structure [7]. The basic micro-structure of the F-MMM was based on the concept of hydrophobic interaction and its effect on the thermodynamics of the protein structures. Hydrophobic interaction is the tendency of hydrophobic moieties of molecules to self-aggregate to exclude water molecules, and the tendency of hydrophilic moiety to associate with the aqueous solution. The lipid molecules, the most important constituent of the biological membrane, are amphiphilic substances. They assemble to lipid bilayers driven by the hydrophobic effect as well as van der Waals forces in aqueous environment. For membrane proteins, their attachment or insertion into lipid bilayers also result from the hydrophobic effect between the hydrophobic tail groups of lipids and the hydrophilic acid residues of proteins. Meanwhile, the hydrophilic groups of the proteins protrude into the aqueous environment around the lipid bilayers [1].

Based on the consideration on the hydrophobic interactions between lipids and proteins, the F-MMM model states that the cell membrane is a completely fluid two-dimensional lipid bilayer that contains globular integral proteins and specific integral protein complexes which are indiscriminately scattered in the membrane. In 1976, the original F-MMM was improved by reflecting the constraints from extracellular and intracellular substances on the lateral spreading and moving of membrane constituents, in particular integral proteins, glyco-

[1] This claim for the protein-lipid arrangement holds true only for some membrane proteins, including integral or intrinsic proteins.

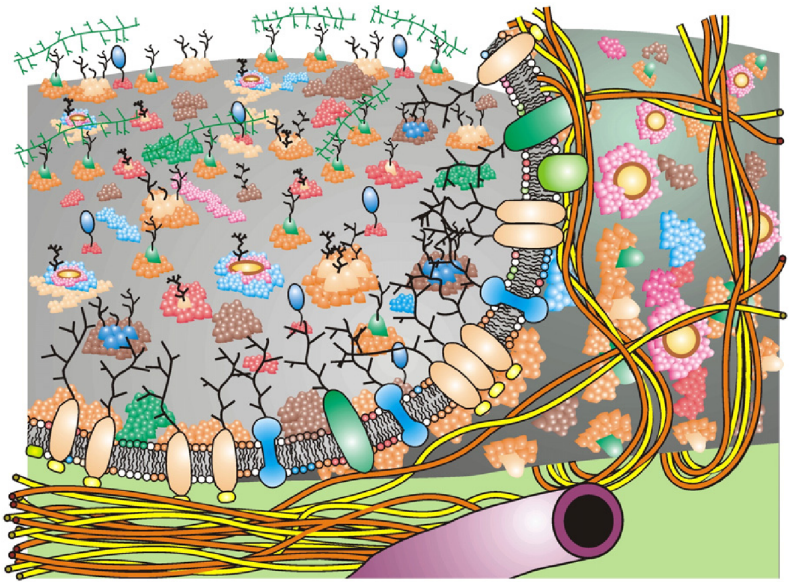

Figure 1.2: Updated Fluid-Mosaic Membrane Model contains lipid bilayers, proteins, gloycoproteins, cytoskeletal and extracellular matrix. Different molecules are labeled by different colors. Reprinted from Ref. [7].

proteins, and protein complexes [43]. Some restricted and semi-restricted regions are from the specific interactions of lipid-lipid, and lipid-protein on the membrane, which can advance the development of protein complex and lipid rafts. The reduced mobility of the integral transmembrane glycoproteins and protein complexes are related to link of the cell membrane with the cytoskeleton filaments as well as the extracellular matrix.

Many other important descriptions for the thermodynamics associated with the membrane structure were introduced since the F-MMM has been proposed in 1970s. One special characteristic are the deformation of the membrane. For instance, the elastic modulus depends on the weak energies of lipid tilting and splaying [21, 22]. How the deformation energy result in different membrane structures on large length scales will be discussed further in the subsequent Chapter "Methods". In addition, the plasma membrane is, often, asymmetric with thousands of different lipid molecules or proteins heterogeneously distributed in the two monolayers. For example, PC is abundant in the extracellular monolayer, whereas PE and PS are exclusively localized in the intracellular monolayer [7, 23]. The generation and maintenance of the asymmetry of the lipid bilayers can be mediated with the passive transbilayer motion (flip-flop) and active energy-consuming bilayer scrambling [44]. The transbilayer motion, or flip-flop, occurs when single lipid molecules spontaneously flip between the monolayers of the bilayer. Bilayer scrambling refers to the behavior of a bundle of lipid molecules, and translocations are less frequent as large free

energy change is required. As a result, a perfectly symmetric structure of the cell membrane is rarely found. A third critical consideration for refining the F-MMM is taking into account "hydrophobic mismatch" [45]. The thickness of the intermediate hydrophobic regions of the transmembrane proteins can be (approximately) equal, longer, and shorter than the biological membranes' thickness. In order to prevent the unfavorable contact of the hydrophobic regions of lipids and proteins with the hydrophilic regions of lipids, proteins, or the aqueous environment, the biological membranes can make a few adaptations to the hydrophobic mismatch. The mattress model proposed by Mouritsen and Bloom in 1984 [46] was used to describe the phase diagrams of the mixing of amphiphilic lipids and proteins in aqueous environment. The elastic properties, and the indirect or direct interactions, such as van der Waals-like interactions, for the cell membrane in included in the model. The mismatch effect can influence the protein aggregation, local orientational changes, and conformational adjustments of proteins and lipids in the membrane.

Biological membranes, such as the cell membrane, are made up of a large number of different lipids and proteins (see the updated F-MMM presented in the Fig. 1.2). Model lipid bilayer membranes consisting of lipid molecules only are also found. Common examples are lipid bilayers, vesicles, and micelles [47, 48]. Lipid bilayers is the thin, flat, and fluid two-monolayer membrane, and is the basic structure of cellular membranes. Vesicles are structures with an encapsulating 'bag' shape, and are in biological systems naturally produced for material-transport associated processes, e. g. exocytosis and endocytosis. A variety of vesicles are present within a cell, including exosomes, microvesicles, apoptotic blebs or vesicles, phagosomes, and COPI and COPII coated vesicles. If vesicles are created artificially via lipid molecules, they are known as liposomes. Liposomes that are enclosed by many phospholipid bilayer, are multilamellar liposomes; with one layer only they are called unilamellar. Micelles, or micellae, are aggregates of phospholipids in aqueous solutions. They exist in equilibrium with spherical shapes. For non-polar solvents, the hydrophobic tail groups of lipids are pointing to the external solvent, while the hydrophilic head groups are gathered in the core. In this case, the structures are called inverse or reverse micelles. Some typical lipid structures are shown in Fig. 1.3.

1.2.3 Elastic properties

Biological and physical properties are important for membrane-mediated interactions, deformations, and shape fluctuations [8, 21, 22], they include:

(a) thickness change: biological membranes contain many embedded proteins and glycoproteins, which can be related to the compressibility of the membrane. Furthermore, the heterogeneous compositions of membranes in-

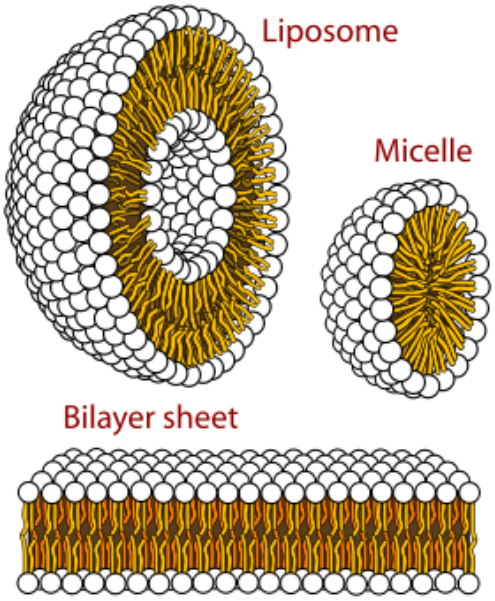

Figure 1.3: Representative structures for lipid bilayer and vesicles (liposome and micelle). Taken from public domain: Wikipedia.

fluence their peristaltic motions, or thickness changes, of the lipid bilayers. However, the fluctuations of the thickness are limited because of the small compressibility of lipid membrane. The amplitude of the thickness change for the lipid membrane is determined by the experiment, the value is as small as 4 Å [49]. The thickness change is essential for many biological events, such as the shape change for the erythrocytes with high flexibility.

(b) stretching: stretching the lipid bilayer can change the area per lipid, which may lead to the exposure of the hydrophobic regions like the lipid chains to the aqueous environment. The contacts for hydrophobic groups and water molecules are energy unfavorable, thus stretching is sub-dominant to bending for membrane deformations.

(c) shearing: the lipid bilayer is a fluid thin film, for which any types of shear forces are ruled out in the lipid membrane. The deformation of the shearing is likely to occur if the lipid membrane is linked to an external scaffold structure, such as the lattice structure and the cytoskeleton.

(d) bending: for the shape fluctuations of the lipid membrane, bending is the most important contribution to the deformation of the membrane. The bending energy is associated with the bending rigidity and membrane curvatures. For some particular systems, other factors such as surface tension and geometric contributions (van der Waals or Coulomb) are also significant for the membrane deformation.

(e) compression: instead to describe the biological membrane as a perfect

single sheet structure (for instance the midplane), we can add the microscopic details regarding the membrane compression to the membrane structure. For the lipid membranes which are bent, the physical properties of the two leaflet are different. For the upper leaflet, the stretching dominants the membrane changes; for the lower leaflet, the compression of the surface occurs. For incompressible membranes, the equilibrium shapes have minimal bending energy; for compressible membranes, the combined bending and stretching energy determine the stable states for the membrane.

(f) tilting: the lipid molecules are not necessarily perpendicular to the neutral plane[2] of the membrane. Experiments show that the angle of tilt of the lipid molecule on the dipalmitoylphosphatidyl-choline (DPPC) bilayer can be as large as 30° (degree) [50] with respect to the normal vector of the neutral plane. Tilting of the lipid molecules is also found for the membranes in the fluid lamellar phase via X-ray scattering. The lipid tilting is associated with a variety of biological processes, including the membrane fusion and inverted amphiphilic mesophases. For low temperatures, the lipid tilting is not relied upon the membrane curvature. Thus it can be coupled into the description of membrane shape as an independent degree of freedom with additional physics implications.

The important structures of the biological membranes include lipid monolayer and bilayer with different biophysical properties. Both of them can be mathematically represented as a thin two dimensional flat sheet embedding in the space for large length scale, refer to the following Chapter "Methods" for further discussions. For lipid bilayers, if the lipid molecules cannot exchange from different leaflets. The lipid area difference for two monolayers is constant, as a result, the associated large-scale bending dominant Hamiltonian is same for both monolayer and bilayer structures. Figure 1.4 shows the four major biophysical properties contributing to membrane deformation. The structures and fluctuations of the lipid membranes are common in a cell, and play a key role in various membrane functions.

1.2.4 Function

Biological membranes, e.g., cell membrane or plasma membrane, surrounds the local spaces or compartments in which different chemical or biochemical substances are contained. In the cytoplasm of a cell, membranes define specialized subunits that are individually enclosed by the lipid bilayers, so-called "membrane-bound" organelles. The cellular transport of molecules and particles among different organelles and plasma membrane is essential for diverse functions in a cell. Two fundamental biological processes for cellular trafficking

[2] A neutral plane is the unstrained surface in the middle of the bent lipid bilayers with a constant area.

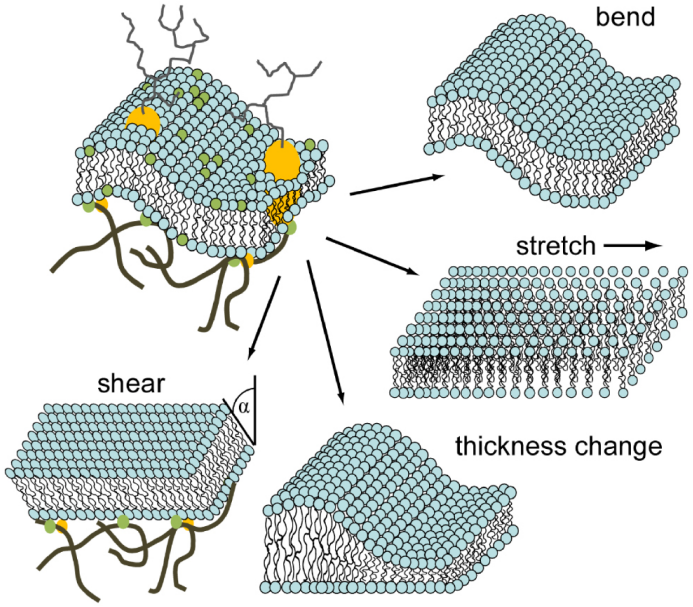

Figure 1.4: Elastic properties contribute to membrane deformations: thickness change, shearing, stretching and bending. Reprinted from Ref. [8].

are endocytosis and exocytosis [9, 10, 51]. In the following sections, we will introduce the main pathways for endo- and exocytosis, and their underlying roles for cell functions.

Endocytosis is a process through which molecules, proteins, and particles are engulfed by the cell membrane [9, 10]. Usually, it is energy-consuming for a cell to absorb and internalize biological substances. Three typical pathways are found for endocytosis: classical endocytosis [52], kiss-and-run endocytosis [53], and bulk endocytosis [54]. Classical endocytosis includes clathrin- and caveolae-dependent and -independent pathways. Clathrin-dependent endocytosis is a receptor-mediated pathway, which is the predominant process in most cells. Caveolae-dependent endocytosis is a common way of cells to uptake small biomolecules, and the invaginations are flask shapes. The clathrin- and caveolae-independent endocytosis have endocytic-like membrane intermediates, such as irregular depth inclusions, and coated or uncoated pits. Examples for this endocytosis are lipid raft and ARF6 (a small molecular weight GTPase) associated pathways. In kiss-and-run endocytosis, a vesicle (e.g. a synaptic vesicle) from extracellular environment contacts the plasma membrane in a short time (kiss), and releases the contained biomolecules by the small transiently-open fusion pores. The vesicle is not collapsed on the membrane and can be retrieved from the plasma membrane after the fusion pore is closed (run). For bulk endocytosis, large endosome-like structures or cisternae are found in a cell, which are deep invaginations internalized from a large area of plasma membrane. Multiple vesicles can bud off from the membranes of

the large structures. Endocytosis plays a key role in mediating cell functions, such as membrane curvature generation, vesicle formation and maintenance, as well as cell movement and division.

Exocytosis, the counterpart of endocytosis, is an active energy-cost process in which biological material is transported out the cell when a vesicle fuses with the plasma membrane [9, 10]. Exocytosis includes three important pathways: full-collapse fusion [55], kiss-and-run exocytosis [53], and compound exocytosis [56]. Kiss-and-run exocytosis is similar to kiss-and-run endocytosis, the main differences is in exocytosis, a domestic vesicle expels the biomolecules out of the plasma membrane. Full-collapse fusion, different from the kiss-and-run endocytosis where a vesicle is in contact, a vesicle completely fuses with the plasma membrane, the whole vesicle disappears as the large fusion pore leads to flattening into the plasma membrane. Compound exocytosis refers to the fusion of small $(20-50\,\mathrm{nm})$ or large $(300-2,000\,\mathrm{nm})$ [57] vesicles which come from the fusion of multiple vesicles, or vesicles with preformed giant vesicles with fused but not collapsed membranes. Exocytosis is important for synaptic strength and plasticity, vesicle replenishment, and multivesicle release.

For cellular trafficking in both endocytosis and exocytosis, the membrane or protein mediated budding from a donor membrane to an acceptor membrane is generally the first important step [58]. For protein-driven membrane budding, one most significant process is the creation of the coated vesicle-like structure. Clathrin, an important protein in membrane budding, can generate different types of basket-shape or lattice-shape coated vesicles with radii of $30-50\,\mathrm{nm}$ [59]. On plasma membranes, clathrin binds to the flat platform-shape adaptor proteins and facilitates the budding of protein-attached membrane in clathrin-dependent endocytosis. The coat protein complex I (COPI) and II (COPII) [60, 61] are responsible for the membrane budding for the coated vesicle carrier from the endoplasmic reticulum (ER) to the Golgi apparatus. Similar to clathrin, vesicle-like basket or lattice invaginations are formed, which are not strongly dependent on the lipid composition.

While protein-dominant membrane budding is characterized by the formation of the coated vesicles, membrane-mediated budding is related to the phase separation in heterogeneous lipid bilayers synthesized in micron length scale. Depending on lipid composition and temperature, the lipid mixtures can exist in either the liquid or the solid ("gel") phase. At given temperature, both liquid and solid phases can be coexistent for spatially separated different lipid clusters [62]. Furthermore, the unsaturated lipids are abandon in liquid disordered (L_d) phase, while the liquid ordered (L_o) phase contains more saturated lipids [63]. As a result, the thickness of the lipid membrane in L_o phase is larger than that in L_d phase. The energetically unfavorable hydrophobic contacts between the amphipathic lipid molecules for the two liquid states lead to line tension, which is the energy cost per length. In order to minimize the line

tension energy, the membrane domains tend to come together to from some circular zones, which are known as "microdomains". Most microdomains in membrane budding are rich in sterol- and sphingolipid molecules, or the so-called "lipid rafts" [58]. When the sizes of the microdomains are large enough for which the line tension energies exceed the Helfrich deformation energies (see the further introduction in Chaper "Methods"), the membrane will bud out and form distorted vesicles to reduce the contact sizes, and the vesicles can even detach from the membrane as the line tension energies are extremely high [64]. For some viruses toxins, such as shiga toxin B [65], can give rise to the arrangements of L_o microdomians, which leads to the formation of negative-curvature favorable tubular vesicles.

1.3 Nanoparticles

Depending on the specific applications of nanoparticles, the definition and viewpoint of them can vary. The meanings of nanoparticles and nanomaterials are different for different organizations [66]. The common characteristic of nanoparticles is that they are materials (natural or artificial) in nanoscale (e.g., $1\,\mathrm{nm} = 10^{-9}\,\mathrm{m}$). They have different components and shapes, see Figs. 1.5 and 1.6. Such small particles can enter the cells via endocytosis. After exerting their functions, they can be expelled out by virtue of exocytosis. A large effort has been devoted to the studies of the interactions between nanoparticles and membranes, like the budding mechanism [67, 68], to understand how nanoparticles are wrapped by the membranes. However, owing to the complexity of biological membranes in structures, components and elastic properties, the elucidations of specific mechanisms for nanoparticle wrapping are still big challenges. For the following sections, we will introduce some typical types of nanoparticles, as well as their important roles in different potential applications.

1.3.1 Types

Nanoparticles are made from a variety of materials including, but no limited to, lipids (e.g. phospholipids and chelesterol), polymers and inorganic materials (e.g. metals, composites, and ceramics), see Figs. 1.5 and 1.6. Nanoparticles gained from these three types of materials is enormous; just list some of them: liposomes, dendrimers, micelles, polymeric drug conjugates, carbon based structures, and metallic nanoparticles [5, 6, 66]. In the following parts, I will introduce one or two important nanoparticles from these three types, as well as their potential applications.

(a) liposomes: the phospholipid molecules of liposomes can self-assemble to closed vesicles in aqueous environments, which can be used to encapsu-

late biotech drug molecules. Liposomes are a leading and most intelligent drug delivery system for both active and passive membrane transport [69, 70]. Many liposome-based drug carriers used for clinical applications are already in market, such as ambisome, daunoXome, inflexal V. Liposomes have enormous advantages rendering them as suitable drug delivery systems. First, liposomes are made of lipid molecules with good biocompatibility, which are easily available for formulating and can display specific biological, chemical, and mechanical aspects. Second, the amphiphilic character of liposomes allows to capture both hydrophilic and hydrophobic agents in their structures. Last, the modifications of the physicochemical properties (size, charge, and surface ligands) of liposomes lead to more functionally favorable carriers. For instance, the stealth liposomes with attached polyethylene glycol-units (PFG) are able to survive longer in the body.

(b) micelles: in micelles, water-insoluble drugs can be linked covalently to their hydrophobic inner cores shielded by amphiphilic groups of the component molecules [4, 70]. Such spheroidal shapes of micelles can also be "core-shell" structures with radii $5 - 50\,\text{nm}$ [5], see Fig. 1.3. A hydrophilic shell can protect the micelles from phagocytosis by macrophages or uptake by reticuloendothelial systems (RES), as the water-bound regions form "splayed" structures such as "polymer brushes". As a result, micelle drug delivery systems can have a prolonged lifetime. Another good aspect of micelle drug-delivery systems is their high efficiency in accumulation at target drug sites [6, 66]. One common example is polymeric micelles, see Fig. 1.5.

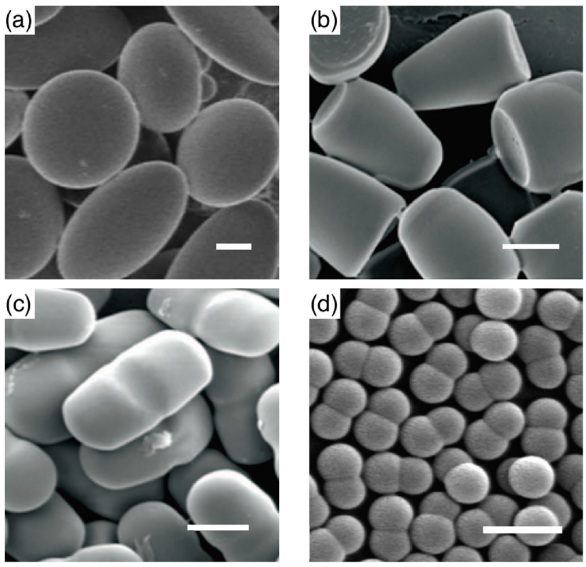

Figure 1.5: Representative structures for polymeric nanoparticles for (a) oblate, disk shape, (b) bullet shape, and (c) pill shape, and (d) dumbbell shape. Reprinted from Ref. [71].

(c) silicon: silicon nanoparticles are engineered by the methods that are used in semiconductors and micro-electromechanical systems (MEMS) [5]. Typical techniques are photolithography, etching, and deposition [72]. Popular silicon-based materials are porous silicon and silica, and silicon dioxide. The structures include calcified nanopores, porous nanoparticles, and nanoneedles. By controlling the nanopore diameter and density, the substances (e.g., biomolecules and drugs) stored in pores can pass through the pores with a specific rate. One of the important silicon-based materials is porous hollow silica nanoparticles, which can deliver cargoes in cells.

(d) metal: metallic nanoparticles are fabricated from different metals, such as gold (Au), silver (Ag), platinum (Pt), and palladium (Pd) [4, 5], see Fig. 1.6. The metallic nanoparticles have been used for a long time. For example, in 4th century AD, Lycurgus cups were fabricated with many small-sized ($\sim 20\,\mathrm{nm}$) nanoparticles [66], which reflect special optical characteristics. Nowadays, one important application of metallic nanoparticles is in biomedicine and biomembrane. Usually, metal covers a core material (e.g. a silica particle) and form a very thin shell around the core. On these hollow metallic covers, a large number of ligands, for instance, nucleic acids, lipid molecules, small proteins, as well as sugars, can be easily anchored to the nanoparticles. The connections between metallic nanoparticles and biological materials can be implicated by a variety of conjugation means, such as bifunctional linkages, lipophilic interaction, silanization (self-assembly with organofunctional alkoxysilane molecules), electrostatic attraction, and nanobead interactions.

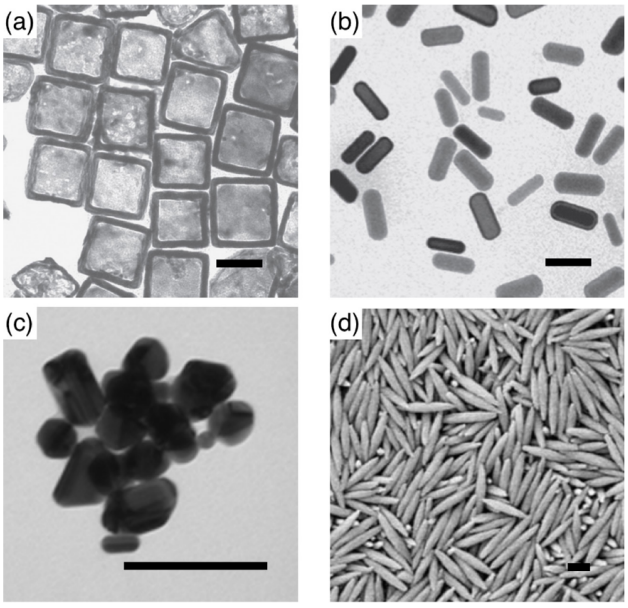

Figure 1.6: Representative structures for (a) cube-like and (b) rod-like gold nanoparticles, (c) irregular silver nanoparticles, and (d) hematite nanospindles. Reprinted from Ref. [71].

1.3.2 Mechanical properties

Nanoparticles have many distinct mechanical properties, which are associated with interfacial forces, including hardness, elastic modulus, stress and strain, adhesion and friction, and movement [4, 73]. An better understanding of these properties of nanoparticles provides significant aids in nanotechnology, and the evaluations for the functions of nanoparticles.

(a) hardness and elastic modulus: the hardness and elastic properties of nanoparticles are tested by microindentation and nanoindentation techniques. In particular, atomic force microscopy (AFM) is helpful to characterize the deformability of nanoparticles. For nanoparticles with sizes smaller or approximate to hundreds of nanometers, the hardness and elastic modulus can vary, depending on the components and shapes of nanoparticles. For instance, for silicon nanoparticles, the elastic modulus increase with decreasing sizes of nanoparticles. For metallic nanoparticles, the dislocations inside the nanoparticles are found during deformations.

(b) adhesion and friction of nanoparticles: in addition to vertical deflection of AFM cantilever, the torsional deflection of cantilever and colloidal-probe techniques are used for investigating the adhesion and friction of nanoparticles on the substance. Research shows that the adhesion force is linearly dependent on the radii of nanoparticles, and the hydrophobic interfaces strongly decrease the adhesion for particles and substances. Meanwhile, the friction forces between nanoparticles and substances increase with particle radius, and is proportional to the contact areas.

(c) movement: the movement of nanoparticles due to different forces such as Brownian motion force, medium and environment is difficult to quantify. Recently, two main methods are used to study the movements of nanoparticles, one is particle tracking with the fluorescence technique, the other one is dynamic light scattering (DLS) technique. Study shows that during movement, the rotating speeds of nanoparticles is much slower than velocities. Nanoparticles with sizes comparable to the length of liquid molecules tend to self-assemble in the medium.

1.3.3 Applications and toxicological risks

Relying upon the components, sizes, shapes, and mechanical properties of nanoparticles, they can be used in various fields, such as nanomedicine, food sciences, chemical and cosmetics. Here we focus on the applications of nanoparticles in the fields of biology, biochemistry, and medicine. We also discuss potential negative side effects related to their applications, such as toxicities.

The most important function for nanoparticles in biological cell is they can serve as delivery systems. As mentioned above, both liposomes [69, 70] and polymeric micelles [5] are suitable drug delivery systems as they have specific

lipid components, vesicular structures, and biochemical characteristics, which guarantees unique advantages in drugs delivery. Among these drug-delivery systems, the nanoparticle-based structures carrying drugs for brain or the central nervous system (CNS) need more attention [5]. The difficulty for brain drug delivery is due to the blood-brain barrier (BBB), an extremely complicated structure composed of impermeable endothelial cells with tight junctions, enzyme catalysis, and efficient efflux-transport. As a result, only a few small molecules (ions and peptides) and a very limited number of macromolecules are able to pass the barrier. It has been shown that poly(butylcyanoacrylate) based nanoparticles can transport several agents, such as dalargin, hexapeptide, doxorubicin, into the brain. These drug-carrying agents are transported across BBB by through of protein-mediated endocytosis [74, 75]. In addition to drugs, nanoparticle delivery systems for peptides, proteins, and genes [76, 77] have been reported. For instance, polymer-based nanoparticles, such as polymeric micelles, encapsulate insulin in the hydrophobic core and preserve the activity of insulin from hydrolytic and enzymatic degradation [78]. Poly(DL-lactide-co-glycolide) (PLGA) nanoparticles are used to transport the therapeutic genes for bone healing [79].

Another significant function for nanoparticles is efficient targeting [80, 81]. The special optical properties of nanoparticles, e.g. metallic nanoparticles, are used as markers for distinct biological tissues and cells, as well as for photo-targeting thermal therapy [82]. Nanoparticles can also be used for tumor targeting, either by passive targeting or active targeting [5, 80]. In passive targeting, an enhanced vascular permeability and retention (EPR) effect are found in tumors, which result from aggregation of therapeutic agents in tumor cells. The accurate targeting is possible due to the high selectivity for agents and ligands that can be linked to nanoparticles. Nanoparticles with sizes of $50 - 500\,\mathrm{nm}$, such as liposomes, micelles, and dendrimers, can deliver drugs to tumor tissue in this way. In active targeting, the ligands (peptides, growth factors, transferrin, antibodies and small compounds) of drug-loaded nanoparticles are directly recognized by the receptors expressed on tumor cells, which initiates the active ligand-receptor binding mediated endocytosis. For example, folate, a small compound, is easily conjugated to the nanoparticles and selectively bind to the carcinomas of the ovary, breast, lung, kidney and brain. The accuracy and efficiency of nanoparticle targeting depends also on their physiochemical properties, such as size, shape and surface charge.

In addition, nanoparticles have potential applications in stem cell therapy, and stimulate immune response. However, besides the rapid developments and wide applications of nanoparticles, toxicity and side effects of nanoparticles are also found [4, 5]. It has been reported that they affect lungs, skin, intestinal tract, and other organs. Adverse health risks of nanoparticles are associated with the binding and wrapping by both targeted and normal cells. For

the nanoparticles in lungs, the poisonous biological outcomes depend strongly on the size of the nanoparticles. Ultrafine nanoparticles, contrary to larger nanoparticles, are able to induce more severe adverse effects, including the development of inflammation and even tumors [83].

Chapter 2

Methods

2.1 Membrane models for different length and time scales

Biological membranes are very thin fluid layers which are composed of hundreds of amphiphilic phospholipids and/or embedded proteins. The typical thickness of a lipid-bilayer membrane is $d \approx 5\,\mathrm{nm}$. This is by far smaller compared to the lateral dimension of the membrane, which can be as large as $10\,\mu\mathrm{m}$. Also, the biophysical processes associated with lipid membranes vary in time scale. For instance, small molecules (ions and water molecules) diffuse across the membrane as rapid as a few nanoseconds [84], and membrane fusion of giant lipid vesicles is shown to occur on a longer time-scale as microsecond [85]. Thus a variety of membrane models covering a wide range of dimensions, from nanometer to micronmeter, are required.

Depending on the question concerned, one can choose the most appropriate computing models to describe the biological phenomena on different length and time scales. Generally speaking, the details of the membrane structure and molecular interactions are usually investigated on nanometer scale, while the morphologies of biological vesicles and membrane self-assemblies are micrometer scales. Membrane models corresponding to different scales from microscopic to be macroscopic are classified to quantum models, all-atom, coarse-grained models, supra-coarse-grained models, and continuum models such as triangulated membrane and mesh-less models [86–90], as shown in Fig. 2.1. Quantum, atomistic and coarse-grained models, and the continuum models, in particular the triangulated membrane model, will be introduced in the following.

Quantum models

On the quantum mechanics level, electronic structure and atomic nuclei are explicitly included in the theoretical models. It is feasible to obtain information

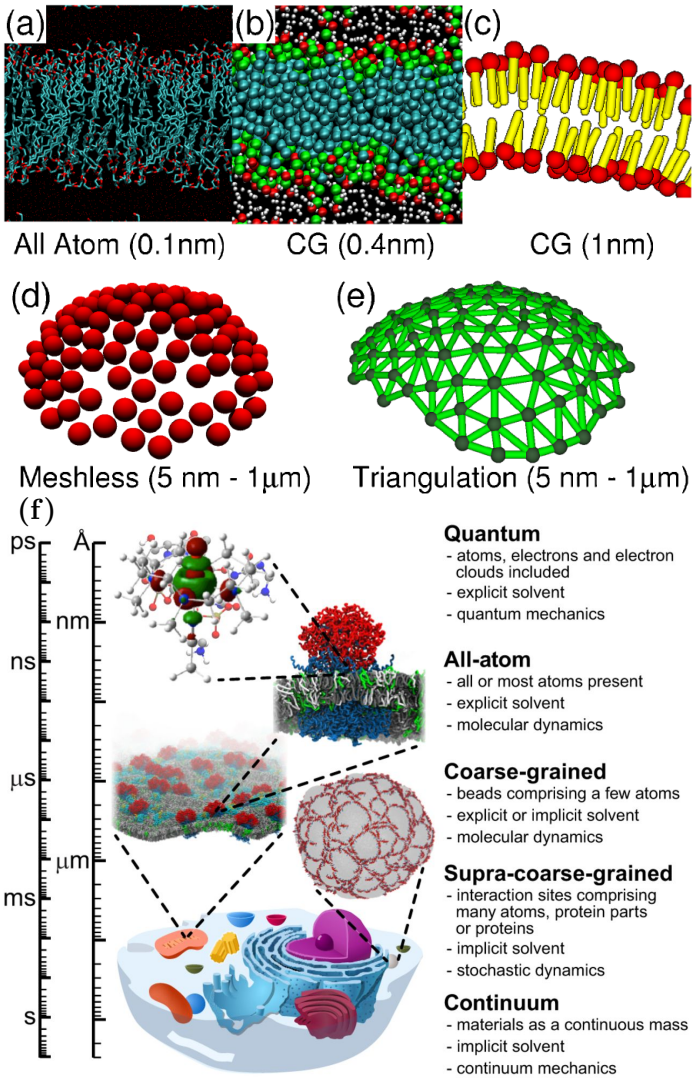

Figure 2.1: Different length-scale representations for (a) all atom molecular dynamics simulation, (b) coarse-grained (CG) model in explicit solvent, (c) coarse-grained model (CG) in implicit solvent, (d) meshless model, (e) triangulation of membrane. Reprinted from Ref. [86], and (f) different length- and time-scale representations from small to large for quantum mechanics, all-atom, coarse-grained, supra-coarse-grained simulations, and a cell. Reprinted from Ref. [87].

about the interaction between electrons, charge transfer, chemical bonds, as well as the band structure of materials with chemical accuracy [89, 91, 92].

The most accurate technique to calculate the electronic structure is wave function-based calculations. However, the computational costs for dealing with wave functions are huge for large molecules [91, 92]. Instead, for large-scale biological systems, the quantum chemical properties can be obtained using density functional theory (DFT) with high accuracy and lower computational

costs [89, 91, 92]. The chemical information for small molecules, obtained using quantum mechanical calculations, can help for atomistic molecular dynamic simulations [87, 89, 91, 92].

All-atom models

A great number of biophysical processes can be understood at an atomistic level, such as receptor-ligand binding [93, 94], protein-membrane interactions [95, 96], protein-nucleic acid interactions [97, 98], as well as protein folding [99]. Atomistic molecular dynamics simulations can be divided into two different categories, depending on whether each atom is independently included in the models [100, 101]. One category is all-atom simulations, where all atoms are simulated in explicit-solvent systems. The other category is united-atom simulations, where a few atoms are integrated into one united-atom, also called pseudo-atom, which can approximately represent the chemical properties of a group of atoms and which is only slightly larger than a single atom.

In molecular dynamic simulations, the dependence of the free energy of the biological system on the coordinates of the molecules is often described by potentials, usually referred to as force field [90, 92, 102]. The mathematical parameters for the (inter-)atomic potential energy can be obtained from *ab initio* or quasi-quantum mechanics calculations, or from experimental methods like X-ray diffraction, nuclear magnetic resonance (NMR), and neutron spectroscopy. A typical empirical force field has two different energy contributions, one component is the intramolecular or local energy including bond stretching, dihedral angles, and angle bending; the other one is intermolecular interactions, which can be hydrophobic repulsion and van der Waals interactions.

Coarse-grained models

For coarse-grained molecular dynamics simulations, at least three heavy atoms are integrated into one pseudo-atom [88]. A biological molecule in a coarse-grained model can be represented by a hybrid of individual atoms and pseudo-atoms, or by pseudo-atoms alone. As a result, a large number of atoms "have vanished", and the number of degrees of freedom for calculating intramolecular, intermolecular interaction potentials is reduced. Because of the high speed of the hydrogen bond vibrations, the simulated time step for all-atom molecular dynamics simulation is limited to $1-2\,\mathrm{fs}$. For coarse-grained molecular dynamics simulations, the time step is about $10-1000$ times longer than than all-atom molecular dynamics simulations [103–106].

Generally speaking, there are two main philosophies to design coarse-grained models for different molecular systems[1]: bottom-up and top-down approaches

[1]The other approaches are 'knowledge-based' model, which rely on experimentally determined structures.

[107–109]. For bottom-up approaches, the molecular descriptions for the coarse-grained models are obtained from a more detailed model, for instance, a classical, empirical atomistic model. For top-down approaches,the molecular descriptions are based on experimental data, usually thermodynamic or macroscopic properties.

Coarse-grained molecular dynamics simulations have been used to investigate the biophysical processes on a larger scales, such as the protein aggregation mediated by lipid molecules [110, 111], membrane fusion and fission [112, 113], and protein-protein interactions [114]. In addition, the information obtained using coarse-grained models can help to bridge the gap between micro- and macroscopic descriptions.

Supra coarse-grained models

In 'supra' coarse-grained models, also referred to as 'highly', 'ultra', and 'shaped-based' coarse-grained models, much more atoms, molecules, and even some parts of proteins and membranes are integrated into a single pseudo-molecule [115, 116]. Therefore, they are even more coarse models compared to coarse-grained models. Supra coarse-grained systems can be combined with particle-based hydrodynamic methods, such as multiparticle collision (MPC), dissipative particle dynamics (DPD), and Brownian dynamics (BD) [86, 87, 117, 118]. Therefore, supra coarse-grained models can treat large of biological molecules in implicit-solvent simulations with increased speed, but decreased accuracy. Examples are large-scale membrane-mediated Bin-Amphiphysin-Rvs proteins (BAR) interactions [119, 120], and aggregated amyloid fibrils in Alzheimer's disease [121, 122].

Triangulated-membrane models

A mesh model made up of several polygon meshes (vertices, edges, and faces) and is typically used to describe the geometric surface and membrane modeling [123–125], a common example is the dynamics triangulated membrane model, which is based on the continuum model for which detailed descriptions can be found in the following Sec. 2.2.

Meshless membrane models

The meshless membrane model is also dependent on the continuum model. For such model, the potential interactions, instead of the meshes, control the assembly of the particles for the fluid membranes. There are three main types of potentials, including soft-core repulsion, anisotropic attractions, and hydrophobic muti-body interactions [126]. Most of the meshless models are simulated in solvent-free environment, and are used to study the bending deformation of membranes [86, 127], as well as the membrane dynamics in flows [128, 129].

2.2 Continuum model

From the previous introduction, we know that lipid-bilayer can laterally extend up to the micrometer length scale, which is significantly larger than the bilayer thickness. Therefore, lipid-bilayer membranes can be described as a two-dimensional fluid surface embedded in the three-dimensional space. We first look back to important concepts and definitions of differential geometry that are used to describe the curves and surfaces for the membranes parametrized in Monge gauge, and extend the geometric description to the implicit model. Subsequently, we will introduce and discuss the Helfrich Hamiltonian in some depth, followed by the Gauss-Bonnet theorem that is usually exploited to deal with the integral over the Gaussian curvatures. Finally, we will discuss the methods used for energy minimization.

2.2.1 Monge gauge

We start to consider the membrane as an one-sheet model where the lipid bilayers is regarded as a mathematical surface [21, 22]. In Monge gauge, the surface can be described using a height function $h(x, y)$ in a three-dimensional Cartesian coordinate system. A simple case is the spherical surface shape, it can be parametrised in Monge gauge as

$$z = \pm h(x, y) = \pm\sqrt{R^2 - x^2 - y^2}\,, \tag{2.1}$$

where the radius of the sphere is R. The plane $\{x, y\}$ is the reference surface, and $z = h(x, y)$ is the height function. The sign $\pm$ refers to the upper (positive) and below (negative) half of the sphere.

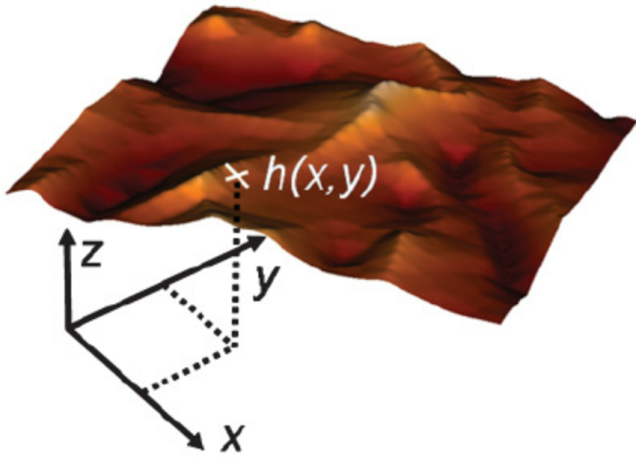

Figure 2.2: A surface parametrized in by Monge gauge. The membrane is defined mathematically as $\{x, y, z\}$ such that $z = h(x, y)$. Reprinted from Ref. [130].

For each point on the reference plane, we can find a specific height function $h(x, y)$, which maps each pair of the reference coordinates $\{x, y\}$ to a point in the embedding three-dimensional space, see Fig. 2.2. For a specific geometric surface parametrized by Monge gauge,

$$\mathbf{r}(x, y) = \begin{pmatrix} x \\ y \\ h(x, y) \end{pmatrix} , \tag{2.2}$$

where the coordinate pairs $(x, y) \in \mathbb{R}^2$, and $\mathbf{r}$ refers to a vector for the point in $\mathbb{R}^3$.

Followed by the parametrized surface, the tangent vectors along the coordinate system axes can be obtained by

$$\mathbf{e}_x = \begin{pmatrix} 1 \\ 0 \\ h_x \end{pmatrix} , \mathbf{e}_y = \begin{pmatrix} 0 \\ 1 \\ h_y \end{pmatrix} , \tag{2.3}$$

where the partial derivatives of the height field in the x and y directions are $h_x = \partial h/\partial x$ and $h_y = \partial h/\partial y$, respectively. The vector set $\{\mathbf{e}_x, \mathbf{e}_y\}$ are tangent to the geometric surface, and the directions of these two vectors are along the axes of the coordinate system. Both vectors, $\mathbf{e}_x$ and $\mathbf{e}_y$, span a local tangent surface space for every point of the surface.

The two vectors $\mathbf{e}_x$ and $\mathbf{e}_y$ are tangent to the surface represented by the Monge gauge parameterization, but they are not always perpendicular to each other. We use the "metric tensor" or "metric" of the surface to reflect if they are orthogonal in the embedding space,

$$g_{xy} = \mathbf{e}_x \cdot \mathbf{e}_y = \begin{pmatrix} 1 + h_x^2 & h_x h_y \\ h_x h_y & 1 + h_y^2 \end{pmatrix} . \tag{2.4}$$

Here, the metric tensor g_{xy} is not a 2×2 matrix, but a twofold covariant vector, and if it contracts with the corresponding contravariant vector g^{xy}, gives rise to the unit matrix. The g^{xy} is found to be

$$g^{xy} = \frac{1}{1 + h_x^2 + h_y^2} \begin{pmatrix} 1 + h_y^2 & -h_x h_y \\ -h_x h_y & 1 + h_x^2 \end{pmatrix} . \tag{2.5}$$

The tensor g_{xy} is also referred as the first fundamental form of the surface.

As the two vectors, $\mathbf{e}_x \mathrm{d}x$ and $\mathbf{e}_y \mathrm{d}y$, describe an immeasurably small local tangent part of to the surface, the area element in Monge gauge is

$$\begin{aligned} \mathrm{d}A &= |\mathbf{e}_x \mathrm{d}x \times \mathbf{e}_y \mathrm{d}y| = \sqrt{\mathbf{e}_x^2 \mathbf{e}_y^2 - (\mathbf{e}_x \cdot \mathbf{e}_y)^2}\, \mathrm{d}x \mathrm{d}y \\ &= \sqrt{|g_{xy}|} \mathrm{d}x \mathrm{d}y \, , \end{aligned} \tag{2.6}$$

where $|g_{xy}|$ is the determinant of the metric tensor g_{xy},

$$|g_{xy}| = 1 + h_x^2 + h_y^2 = 1 + \nabla^2 h, \tag{2.7}$$

with Laplace operator $\nabla^2 = (\partial_x^2, \partial_y^2)$.

From the two tangent vectors, $\mathbf{e}_x$ and $\mathbf{e}_y$, we can define the surface normal vector as

$$\begin{aligned} \mathbf{n} &= \frac{\mathbf{e}_x \times \mathbf{e}_y}{|\mathbf{e}_x \times \mathbf{e}_y|} = \frac{\mathbf{e}_x \times \mathbf{e}_y}{\sqrt{|g_{xy}|}} \\ &= \frac{1}{\sqrt{1 + (\nabla h)^2}} \begin{pmatrix} -h_x \\ -h_y \\ 1 \end{pmatrix} \end{aligned} \tag{2.8}$$

to get a local three-dimensional coordinate system. The normal vector $\mathbf{n}$ is normalized to unit length. The second fundamental form K_{xy} of the surface is obtained from the normal vector $\mathbf{n}$ as [2]

$$\begin{aligned} K_{xy} &= -\mathbf{e}_y \cdot \partial_x \mathbf{n} = \mathbf{n} \cdot \partial_x \mathbf{e}_y = \mathbf{n} \cdot \partial_{xy} \mathbf{r} \\ &= \frac{1}{1 + (\nabla h)^2} \begin{pmatrix} h_{xx} & h_{xy} \\ h_{xy} & h_{yy} \end{pmatrix} . \end{aligned} \tag{2.9}$$

The tensor K_{xy} is also known as the "extrinsic" curvature tensor, as it requires the normal vector, which can embed the surface into a higher-dimensional space. According to the definition, the extrinsic tensor K_{xy} essentially measures the changes of the local curvature when the normal vector walks along the surface.

The curvature tensor K_{xy} is a quadratic form, two nonzero eigenvalues and eigenvectors can be found. In fact, two eigenvectors are known as the principle directions and point into the directions along which the minimal and maximal curvatures of the surface are found. The corresponding eigenvalues are called as principle curvatures, denoted as c_1 and c_2, see Fig. 2.3. The trace of the curvature tensor K_{xy} is a constant scalar variable, which gives rise to the mean curvature H of the surface,

$$\begin{aligned} H &= \frac{g^{xy} K_{xy}}{2} = \frac{c_1 + c_2}{2} \\ &= \nabla \cdot \left(\frac{\nabla h}{\sqrt{1 + (\nabla h)^2}} \right) \\ &= \frac{(1 + h_x^2) h_{yy} + (1 + h_y^2) h_{xx} - 2 h_x h_y h_{xy}}{2(1 + h_x^2 + h_y^2)^{3/2}} . \end{aligned} \tag{2.10}$$

[2] Here, the curvature of the surface is positive if the normal vector points outward, otherwise it is negative. The mathematical books tend to define the curvature oppositely.

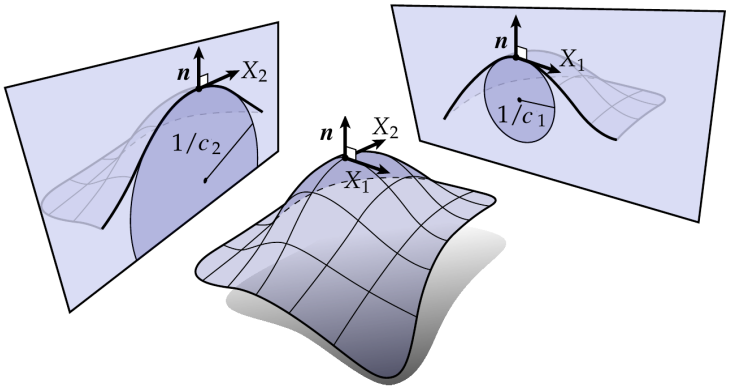

Figure 2.3: Illustrations of the normal vectors, principle directions and principle curvatures. The unit eigenvectors $\mathbf{X}_1$ and $\mathbf{X}_2$ along which the minimal and maximal curvatures of the surface, c_1 and c_2, are found. The reciprocals of the principle curvatures, $1/c_1$ and $1/c_2$, denote the radii of the osculating circles, the normal vector $\mathbf{n}$ is perpendicular to the principle vectors. Reprinted from Ref. [131].

The other important constant scalar associated with the curvature tensor is called the Gaussian curvature, K, and it is obtained by the determinant of the tensor,

$$\begin{aligned} K &= \det(K_x^y) = c_1 c_2 \\ &= \frac{\det[\partial^2 h]}{(1+(\nabla h)^2)^2} \\ &= \frac{h_{xx}h_{yy} - h_{xy}^2}{(1+h_x^2+h_y^2)^2}\,, \end{aligned} \tag{2.11}$$

with the Hessian $\partial^2 h$ of the height function $h(x, y)$.

The principle curvatures, c_1 and c_2, determine the local geometry of the surface [131]. The special cases are the zero-curvature surfaces. For instance, the surface with zero Gaussian curvature, $K = 0$, is a piece of flat plane, or a curved cylinder. This surface is known as "developable surface" owning to the "developed" or extended characteristics in the plane. The mean curvature surface with $H = 0$ is called "minimal surface" for which the minimal area is achieved. Such surfaces always have local, saddle-like shape deformations. If both local curvatures are positive, the surface is a convex semi-sphere, and the surface is a concave semi-sphere for negative curvatures (figure not shown), see Fig. 2.4.

2.2.2 Implicit model

In Monge gauge, a surface is mathematically described as an one-sheet surface in the parametric form, $\mathbf{r}(x, y)$, in a three-dimensional Cartesian coordinate

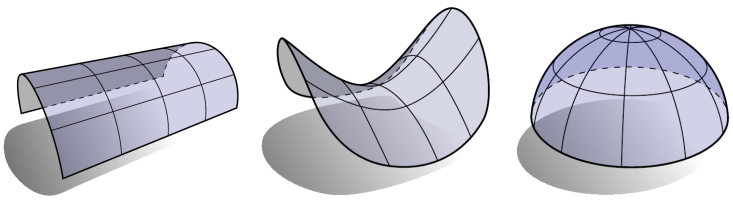

Figure 2.4: Representative shapes for a "developable surface" (curved cylinder) with Gaussian curvature $K = 0$, a "minimal surface" (saddle-like) with mean curvature $H = 0$, and a convex hemisphere with principle curvatures $c_1 > 0$ and $c_2 > 0$. Reprinted from Ref. [131].

system, as shown in Eq. (2.2). For a small patch of planar membrane for which there are no overhangs, the Monge gauge parameterization is always applicable. For a more general surface model of the fluid membrane, the geometric function for the shape can be given in the implicit form, $F(\mathbf{r}) = 0$, where $\mathbf{r} = \mathbf{r}(x, y, z) \in \mathbb{R}^3$. For instance, the geometric surface can be written as $F(\mathbf{r}) = h(x, y) - z = 0$ in a Cartesian coordinate system. The subsequent discussion of the implicit model is based on the Ref. [132].

Any two tangent vectors can form a basis for the local tangent plane of the surface. Suppose x and y are on the reference plane, the tangent vectors respective to x and y are

$$\mathbf{e}_x = \frac{\partial \mathbf{r}}{\partial x}\,, \mathbf{e}_y = \frac{\partial \mathbf{r}}{\partial y}\,, \tag{2.12}$$

for which the normal vector at each point of the surface is given by

$$\mathbf{n} = \frac{\nabla F}{|\nabla F|} = \frac{\mathbf{e}_x \times \mathbf{e}_y}{|\mathbf{e}_x \times \mathbf{e}_y|}\,, \tag{2.13}$$

where the direction of the gradient of F is the direction of the normal vector $\mathbf{n}$. The curvature tensor, $\mathbf{C}$, describes the change of the normal vector $\mathbf{n}$,

$$\mathrm{d}\mathbf{n} = \mathbf{C} \cdot d\mathbf{r}\,, \tag{2.14}$$

when it walks along the surface. For Cartesian coordinate system,

$$\begin{pmatrix} \mathrm{d}\mathbf{n}_x \\ \mathrm{d}\mathbf{n}_y \\ \mathrm{d}\mathbf{n}_z \end{pmatrix} = \begin{pmatrix} \partial\mathbf{n}_x/\partial x & \partial\mathbf{n}_x/\partial y & \partial\mathbf{n}_x/\partial z \\ \partial\mathbf{n}_y/\partial x & \partial\mathbf{n}_y/\partial y & \partial\mathbf{n}_y/\partial z \\ \partial\mathbf{n}_z/\partial x & \partial\mathbf{n}_z/\partial y & \partial\mathbf{n}_z/\partial z \end{pmatrix} \begin{pmatrix} \mathrm{d}x \\ \mathrm{d}y \\ \mathrm{d}z \end{pmatrix}\,, \tag{2.15}$$

and

$$\mathbf{C} = \frac{1}{|\nabla F|}(F_{i,j} + \frac{F_i|\nabla F|_j}{|\nabla F|})\,, \tag{2.16}$$

for $i, j \in \{x, y, z\}$.

From the 3×3 matrix $\mathbf{C}$, in general, up to three linearly independent eigenvalues and eigenvectors can be determined. However, the surface model

for the membrane in the implicit form is a function of only two independent parameters, e.g. x and y. Therefore, the two eigenvalues, c_1 and c_2, and the corresponding eigenvectors of the tensor $\mathbf{C}$ are those of the extrinsic curvature tensor K_{xy}.

Two invariants of the curvature tensor are the mean curvature, $H = (c_1 + c_2)/2$, and the Gaussian curvature, $K = c_1 c_2$, which can be obtained by the trace and the determinant of the curvature tensor, respectively [3]. In a Cartesian coordinate system, the mean curvature and the Gaussian curvature are expressed as

$$H = \frac{1}{2|\nabla F|^3}(F_{xx}(F_y^2 + F_z^2) - 2F_x F_y F_{xy} + \text{Perm}), \tag{2.17}$$

and

$$K = \frac{1}{|\nabla F|^4}(F_{xx}F_{yy}F_z^2 - F_{xy}^2 F_z^2 + 2F_{xz}F_x(F_y F_{yz} - F_z F_{yy}) + \text{Perm}), \tag{2.18}$$

respectively, where Perm stands for permutations of the previous terms.

For surface shapes represented by Monge gauge parameterization, the mean curvature, H, and the Gaussian curvature, K, are specific cases in the implicit model, see Eqs. (2.10) and (2.11), respectively. If we now suppose the lipid membrane is almost planar, for which only weak enough deviations from the reference plane can be found, such that $h_x \ll 1$ and $h_y \ll 1$, the expressions for the mean curvature H and the Gaussian curvature K can be simplified to

$$H \approx \frac{\text{Tr}[\partial^2 h]}{2} = \frac{\nabla^2 h}{2} = \frac{h_{xx} + h_{yy}}{2}, \tag{2.19}$$

and

$$K \approx \det[\partial^2 h] = h_{xx}h_{yy} - h_{xy}^2, \tag{2.20}$$

respectively. The reduced form is known as "linearized Monge gauge", and it has been widely employed in a good many of theoretical and analytical models for fluid membranes.

2.2.3 Helfrich Hamiltonian

If we consider a patch of a lipid-bilayer membrane that is sufficiently small in atomistic dimensions, hundreds of thousands of degrees of freedom for molecules have to be taken into account in the theoretical models. However, many important biophysical events happen on large scales. Quantum and atomistic models are not applicable to study the membrane on these scales. A large number of analytical and numerical methods have been developed to

[3] The third invariant scalar for the curvature tensor is, $\det(\mathbf{C}) = 0$.

focus on the physical aspects of the lipid membrane on an adequately large length scale. In particular, the separation of the length scales for the membrane thickness and the lateral dimension enables us to investigate the system on the mesoscopic scale. The material parameters such membrane Hamiltonian are connected with the curvature tensors, and independent of the local, atomistic details. In other words, on large length scale, the primary soft mode is the curvature deformation. The seminal works on this geometric Hamiltonian for the lipid membrane from the 1970s are from Canham [20], Helfrich [19] and Evans [133].

To study the biconcave shapes of erythrocytes [20], Canham found that the summation of the squares of the principal curvatures of the local surfaces determines the bending energy density of the plasma membrane. The stable geometries and the lowest bending energies deviated from the expression can well describe the representative shape profiles of red blood cells. Helfrich proposed that for the non-spherical shapes of enclosed vesicles, the curvature elasticity is the key parameter for the deformation of the lipid bilayers; and an asymmetry of the lipid bilayers, represented by the spontaneous curvature, can influence the elastic rigidity of the membrane [19]. Evans suggested that even small changes of the interfacial chemical free energy densities, or the surface tension, can significantly affect the the membrane curvature [133].

On the mesoscopic length scale, the Helfrich Hamiltonian is found to be only associated with the geometric curvatures of the plasma membrane [19, 20, 133, 134]. The energy density at each point of an almost planar membrane, with weak enough deviations from the reference plane, can be expanded to quadratic order in the principle curvatures, c_1 and c_2, as

$$E_{\mathrm{b}} = \int \mathrm{d}A \left\{ \alpha_1 + \alpha_2 c_1 + \alpha_3 c_2 + \alpha_4 c_1^2 + \alpha_5 c_2^2 + \alpha_6 c_1 c_2 + O[c^3] \right\}, \tag{2.21}$$

where the integral is calculated over the entire membrane area. In fact, only four independent expansion parameters are found for the curvatures up to quadratic order, as the fluid membrane has no special directions, such that $\alpha_2 = \alpha_3$ and $\alpha_4 = \alpha_5$. The equations in Eq. (2.21) can thus be altered to the famous form of "Helfrich Hamiltonian",

$$\begin{aligned} E_{\mathrm{b}} &= \int \mathrm{d}A \left\{ 2\kappa (\frac{c_1 + c_2}{2} - c_0)^2 + \bar{\kappa} c_1 c_2 + \sigma + O[c^3] \right\} \\ &= \int \mathrm{d}A \left\{ 2\kappa (H - c_0)^2 + \bar{\kappa} K + \sigma + O[c^3] \right\}, \end{aligned} \tag{2.22}$$

with the elastic parameters σ, c_0, κ and $\bar{\kappa}$.

Before introducing the physical meaning of these four different parameters, we first look at the mathematical properties of the energy function. It is obvious that all different components in the Helfrich Hamiltonian are Galileo-invariant, as only curvatures enter the expression. This indicates that the

bending energy is constant for the translated and rotated membranes. In addition, the energy functional is independent of the parametrized coordinate system, for both the trace and the determinant of curvature tensor, the mean curvature, H, and the Gaussian curvature, G, are invariants.

The coefficients associated with the Helfrich Hamiltonian have direct physical meanings [21, 22]:

- Membrane tension σ. The independent thermodynamic variable, σ, is always considered as an elastic constant, and the associated energy term σA is proportional to the total (or projected) area A of the membrane. The coefficient σ can also be used as Lagrange multiplier to fix the membrane area when minimizing the deformation energy of the membrane.

- Spontaneous curvature c_0. The preferred curvature c_0 reflects the "lack of symmetry" of a lipid-bilayer. The two monolayers of the lipid membrane are not symmetric for spontaneous curvature $c_0 \neq 0$. This can, for example, result from the differences in the kinds and the components of the lipid molecules and proteins.

- Curvature modulus κ. The elastic coefficient κ is the "bending modulus" or "bending rigidity", the energy needed to bend the planar membrane. The bending rigidity κ can be measured via finer-scale theories of the membrane and experimental methods, and the typical value is $\kappa \sim 20 k_B T$ [135, 136]. The bending rigidity κ will be discussed in detail for the following chapters.

- Curvature modulus $\bar{\kappa}$. The constant $\bar{\kappa}$ is the "Gaussian curvature modulus" or "saddle-splay modulus". The two constants κ and $\bar{\kappa}$ are of the same order of magnitude. The value of $\bar{\kappa}$ is difficult to find as the membrane shape is irresponsible to this modulus, and it only matters for topological changes, such as fission and fusion. The role of the saddle-splay modulus $\bar{\kappa}$ is further discussed in the subsequent section "Gausss-Bonnet theorem".

We can see from the introduction above that for deformations of a lipid-bilayer membrane, the elastic bending rigidity κ is the most important parameter to calculate the lowest bending energy shapes. The surface tension σ are often neglected for amphiphilic membranes, as the area of the membrane is fixed by the number of lipid molecules. If the lipid membrane is symmetric, the spontaneous curvature is $c_0 = 0$. Finally, the integral over the Gaussian curvature keeps constant for a system without topological changes.

2.2.4 Gauss-Bonnet theorem

The Gaussian energy term in the Helfrich Hamiltonian, Eq. (2.21), is the integral of the Gaussian curvature K over the total membrane area A,

$$E_{\mathrm{k}} = \bar{\kappa} \int \mathrm{d}A\, K\,, \tag{2.23}$$

with the constant Gaussian saddle-splay $\bar{\kappa}$. The Gauss-Bonnet theorem relates the value of this integral to the topology of the membrane [137, 138]. In particular, for a closed surface, the integral over the Gaussian curvature K is

$$\int \mathrm{d}A\, K = 2\pi\chi_A\,, \tag{2.24}$$

where χ_A is Euler characteristic of the geometric surface. This shows that the Gaussian saddle-splay modulus $\bar{\kappa}$ dose not contribute to energy deformations for geometric shape of the surface. The characteristic Euler for a polyhedral surface is

$$\chi_A = V - E + F\,, \tag{2.25}$$

with the vertices V, edges E, and facets F of the polyhedra. The Euler characteristic χ_A can also be obtained from

$$\chi_A = 2(n - g)\,, \tag{2.26}$$

where n and g are the numbers of objects and handles, respectively. Figure 2.5 shows some typical systems to illustrate the Euler characteristic χ_A. For example, for a sphere, $\chi_A = 2$ given by Eq. (2.26); for a cube, according to (2.25), $V = 8$, $E = 12$, $F = 6$, and $\chi_A = 2$. Both the sphere and the cube have the same Euler characteristic, they are, in fact, topological equivalents with different geometric shapes. For a torus, $n = 1$, $g = 1$, and $\chi_A = 0$, see Eq. (2.26). Similarly, one planar membrane has Euler characteristic $\chi_A = 0$, and two connected planar membranes have $\chi_A = -2$.

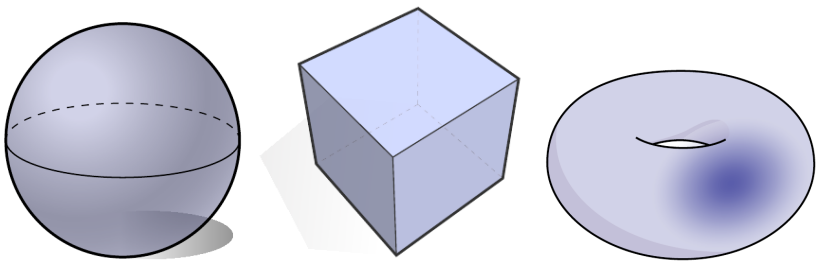

Figure 2.5: The Euler characteristic for the sphere, the cube, and the torus are $\chi_A = 2$, 2, and 0, respectively. The sphere and the cube are topological equivalents with the same Euler characteristic. Reprinted from Ref. [131].

For different vesicles with different areas, volumes and spontaneous curvatures, their shapes can be spheres, stomatocytes, oblates, and prolates, the Gaussian energy term E_k is identical as long as the Gaussian saddle-splay modulus $\bar{\kappa}$ is identical. Similarly, for red blood cells, the different shape fluctuations are not related to the the Gaussian energies E_k, as there is no topological changes in red blood cells. Furthermore, E_k is independent of the thermal fluctuations of the membrane.

2.3 Energy minimization

There are three different kinds of methods which are used to determine stable shapes with the lowest deformation energies for membranes [16, 137].

First of all, one can directly try to solve the Euler-Lagrange equations, also referred to as shape equation. For those axisymmetric shapes, the Euler-Lagrange equation is changed to a set of one-dimensional non-linear ordinary differential equations up to second order, and the optimal shapes can be obtained by solving the partial differential equations. Here, the arc-length parametrization is used to describe the axisymmetric shapes, and the numerical solutions can be obtained with constraints for membrane area, and vesicle volumes. This method works provides high degree of efficiency and accuracy. It has therefore been used for a large number of studies. For instance, the wrapping of spherical particles by the fluid membranes [139–141], and shape deformations of lipid bilayers that wrap the infinitely long cylinders have been calculated using shape equations [139, 142]. But this method cannot be taken into account for the non-axisymmetric shapes.

The second approach is the so-called variational method, which is based on the Gibbs-Bogoliubov-Feynman inequality. The aim of the variational method is to find a reference system, for which the energy can be calculated using a model Hamiltonian with free parameters that can be optimized. If membrane curvature energy for both the reference Hamiltonian and Hamiltonian of interest are equal, the free energy of the system of interest is not larger than of the reference system, according to the Gibbs-Bogoliubov-Feynman inequality. By choosing optimal parameter values, we can obtain an upper bound to the energy of the system of interest. Examples of this method include employing Cassini ovals [20], spherical harmonics [143], and Fourier functions to parametrize the membrane shapes [144].

The last brute-force method is to use triangulated membranes to minimize the deformation energy [16, 124, 145]. The membranes are constructed using triangulations of the surfaces. The positions of the vertices are used to calculate the discretized expression form of the mean curvatures integrals. Triangulated membranes give rise to a large amount of parameter freedoms to calculate deformation and energies, for which the required computing time and memory

for minimization can be extensive. However, the triangulated membrane model provides a high degree of flexibility, and it can be used to calculate integrals for non-axisymmetric systems. We use the freely available software "Surface Evolver" [146] to investigate the nanoparticle-membrane interaction. In brief, this package employs a finite-element code to predict the stable shapes of surfaces which are initially defined as a simplicial complex.

Continuum membrane models and energy minimisation have been successfully applied to predict interactions of membranes with particles of different shapes and sizes. A spherical nanoparticle at an infinitely large membrane, for example, is non-wrapped for small adhesion strengths; wrapping occurs if the adhesion-energy gain overcomes the bending-energy cost [16, 140]. Stable partial-wrapped states are found for spherical particles that interact with patches of planar membranes which have finite surface tensions [140, 147], for non-spherical particles [15, 16], for particles at curved membranes [14], and for particles or membranes with spontaneous curvature [13, 71]. For spherical vesicles and for out-to-in wrapping (e.g. endocytosis), the membrane is bent in the opposite direction as the curvature prior to wrapping, and the transition from the non-wrapped to the complete-wrapped state is discontinuous with an energy barrier. For in-to-out wrapping (e.g. exocytosis), partial-wrapped states are found over a wide range of particle-membrane adhesion strengths. Partial-wrapped particles move on pre-wrapping membrane curvature gradients towards places where the membrane is curved most in the direction of the particle [148], similar to aggregation and cooperative budding of spherical-cap inclusions [149–151].

Chapter 3

Nanoparticle wrapping by non-spherical vesicles

The biological membranes are natural barriers to nanoparticles when they are wrapped by living organisms. For nanoparticles getting into and out of vesicles and cells, they interact with the lipid bilayer membranes, membranous organelles, such as the endoplasmic reticulum and the Golgi apparatus, the nucleus, and intracellular and extracellular vesicles, such as autophagosomes, lysosomes, and exosomes. Extracellular vesicles have lead to an increasing interest in scientific study, as they are functionally involved in the transmission of biological signals, and as intrinsic regulators for physiological and pathological processes; they are also able to be applied as potential targeted-drug-delivery systems that work accurately and efficiently. Exosomes, small vesicles containing proteins, mRNA, and miRNA, that are released by cells into the extracellular environment have been suggested to participate in tumor metastasis. The interactions between nanoparticle and membrane have been shown to rely upon particle shape, size, orientation, surface functionalization, membrane curvature-elastic properties, and particle-membrane adhesion. We systematically characterize the wrapping behaviors of nanoparticles that enter and exit vesicles, taking into account particle size, vesicle size, reduced volume, and membrane spontaneous curvature. We find complicated wrapping diagrams where nanoparticle wrapping transitions and vesicle shape transitions are coupled. In particular, for large particle-to-vesicle size ratios the shape changes of the free membrane contribute significantly to the deformation energy upon wrapping. Furthermore, partial-wrapped membrane-bound particles impose boundary conditions on the membrane that affect vesicle shapes and stabilise oblates and stomatocytes for particle entry, and prolates and stomatocytes for particle exit. Our calculations provides an insight into the wrapping mechanisms for nanoparticle-vesicle interactions, and the results suggest that nanoparticles may stimulate autophagocytic engulfment,

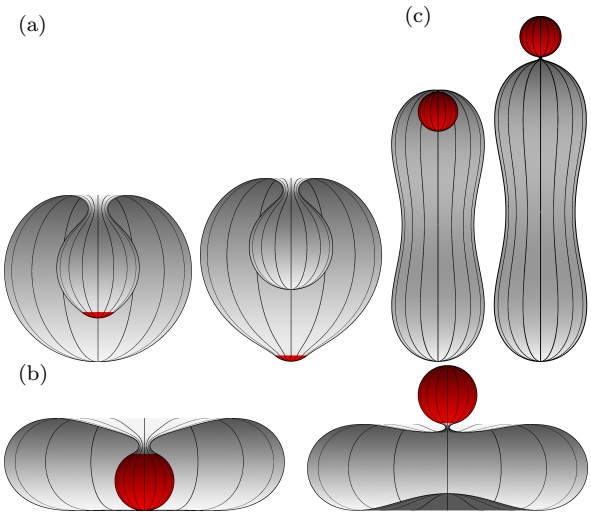

Figure 3.1: Representative snapshots for (a) stomatocyte, (b) oblate, and (c) prolate vesicles and spherical nanoparticles with wrapping fractions $A_{\mathrm{ad}}/A_{\mathrm{p}} = 0.12$, 0.95 and 0.99 for particle-to-vesicle size ratio $R_{\mathrm{p}}/R_{\mathrm{v}} = 0.25$, reduced volume $v = 0.6515$, and spontaneous curvature-to-particle curvature ratio $c_0/c_{\mathrm{p}} = -0.032$ (for the right subfigure in (b) $A_{\mathrm{ad}}/A_{\mathrm{p}} = 0.98$ and $c_0/c_{\mathrm{p}} = -0.063$). A_{p} is the area of the particle, A_{ad} is the adhered membrane, colored in red. The free membrane of the vesicle is colored in white. Membrane area and vesicle volume are constant. All left subfigures show out-to-in wrapping (endocytosis), all right subfigures show in-to-out wrapping (exocytosis).

which would facilitate transport of the nanoparticles into lysosomes and would lead to subsequent degradation of nanoparticle-attached proteins.

3.1 Introduction

The adhesion and wrapping of nanoparticles by lipid-bilayer membranes of biological cells are the first essential steps for their application in biophysics, medicine, nanotechnology and other aspects. Nanoparticles have been used as targeted drug delivery [152, 153], as heat sources for cancer therapy [154], as markers for imaging [155], and as "glue" for wound healing [156] because they are extremely small in size. There is no doubt that nanoparticles are a kind of materials which are widely used for our daily lives, therefore a systematic and comprehensive understanding of their interactions with cellular membranes is considerably important to assess potential nanotoxicological risks and biosafety problems exerted by the nanoparticles. A large variety of engineered nano- and microparticles can nowadays be fabricated from various materials, for example, small polymers, dendrimers, silica and gold. Also a wide range of shapes of nanoparticles including spherical, cylindrical, discoidal, nanoworm and nanorod (elongated cylindrical) structures are designed for specific functions. In biological systems, analogies from parasites and viruses to

non-spherical particles can be drawn. Viruses have sizes of about 100 nm and can have bullet-like or filamentous shapes [67, 157, 158]. Malaria parasites, also called merozoites, can be modeled as egg-shaped microparticles [159].

Different small vesicles, whose sizes that can be comparable to those of nanoparticles, have very important functions for signaling, material transport, and degradation occur in biological systems. For instance, synaptic vesicles (or neurotransmitter vesicles) are essential for propagating chemical messengers and biological signals between neurons. Exosomes, small vesicles released directly from the cytoplasmic membranes and indirectly from the cells, function as important messengers for genetic contents as well as specific targets for preventing cancer metastasis. Similar to many other biological vesicles, they can have heterogeneous morphologies (round, elongated, and tubular shapes) [160, 161] in extracellular environment. Mammalian autophagosomes with spherical structures digest material from inside the cell, and lysosomes are involved in a large number of processes including degradation. Finally, engineered small vesicles can be used as delivery systems, for example for targeted drug delivery [162–164] with a high degree of accuracy and efficiency.

In addition to the principle curvature of the particle surface, also the curvature of the membrane prior to wrapping has to be taken into account for the description of particle wrapping. For spherical particles that interact with vesicles with constant membrane areas and freely adjustable volumes, numerical calculations show that for out-to-in wrapping, where the particles are initially located outside the vesicles, an energy barrier separating the non-wrapped from the complete-wrapped state is found; for in-to-out wrapping, where the particles are initially located inside the vesicle, partial-wrapped states are stable over a wide range of particle-membrane adhesion strengths [14].

A theoretical model for budding and wrapping of elastic particles shows that the ranges of adhesion strength and particle-to-vesicle size ratios, for which stable partial-wrapped states are found, increase with increasing particle deformability [165]. For vesicles with non-spherical shapes, partial-wrapped particles move on pre-wrapping membrane curvature gradients towards places where the membrane is curved most in the direction of the particle [148], similar to aggregation and cooperative budding of spherical-cap inclusions [149–151].

A third curvature-related parameter that affects particle wrapping is the spontaneous curvature of the membrane. The spontaneous curvature is a preferred curvature provided by the lipid asymmetry between the two monolayers of the lipid bilayer. The hydrophobic mismatch of various lipid constituents and integral proteins attributes to the asymmetry of the membrane. Also the different chemical structures of lipid molecules induce the plasma membrane to exhibit slightly positive and negative curvatures. Scientific research shows that spontaneous curvatures of single lipids are typically in the range $(0.1-1)\,\mathrm{nm}^{-1}$ [166–168], such that differences in the mole fractions of lipids between the

monolayers of few percent can induce spontaneous membrane curvatures in the range $-10^{-3}\,\mathrm{nm}^{-1} \leq \mathrm{c}_0 \leq 10^{-3}\,\mathrm{nm}^{-1}$. Stable partial-wrapped states are found for spontaneous curvatures opposite to the curvature of the particle surface, while energy barriers between the non-wrapped and the complete-wrapped states are predicted for spontaneous curvatures towards the particles [13]. Spontaneous membrane curvature may serve as explanation for the experimentally observed size selectivity for nanoparticle wrapping [13, 169], which is an alternative approach to receptor diffusion-based selectivity [170, 171].

In this chapter, we systematically investigate the interaction of spherical particles with vesicles with different reduced volumes v. In addition to the ratios of the vesicle curvature c_v to the particle curvature c_p, the reduced particle size $\tilde{R}_\mathrm{p} = c_\mathrm{v}/c_\mathrm{p} = R_\mathrm{p}/R_\mathrm{v}$, and of the spontaneous curvature c_0 of the membrane to the particle curvature, the reduced spontaneous curvature $\tilde{c}_0 = c_0/c_\mathrm{p}$, we also consider different reduced volumes of the vesicles. The reduced volume is the actual volume of the vesicle divided by the maximal volume that can be enclosed with the same membrane area. Vesicles with $c_0 = 0$ have prolate shapes for reduced volumes $v > 0.6515$, oblate shapes for reduced volumes $0.5915 < v < 0.6515$, and stomatocyte shapes for reduced volumes $v < 0.5915$ [172]. In addition to the wrapping transitions between non-wrapped, partial-wrapped, and complete-wrapped states of the particles, also shape transitions for the vesicles between stomatocytes, oblates, and prolates are observed. Figure 3.1 shows some examples of particle-vesicle systems for stomatocytes, oblates and prolates. Our main results show that both wrapping and shape transitions occur during nanoparticle-wrapping of vesicles and that both transitions can be coupled.

3.2 Model and calculation technique

3.2.1 Calculating deformation and adhesion energies

Determined by the different lengths of the research systems in interest, a variety of simulated models and calculations techniques have to be used. For instance, to study the nanoparticles with sizes that are comparable to or smaller than the membrane thickness ($d \approx 5\,\mathrm{nm}$) and nanoparticle aggregates with very irregular shapes, coarse-grained molecular dynamics simulations or other particle-based techniques that account for the finite thickness of the lipid bilayer can be apply[51, 173–176]. For particles with radii of $10 - 20\,\mathrm{nm}$ and above, continuum models where lipid bilayers are described as elastic mathematical surfaces with curvature-elastic parameters are often the most powerful choice for systematic studies [172, 177–180].

Membranes are described as mathematical surfaces in continuum models, and the mechanical deformation energies are predicted by curvature-elastic

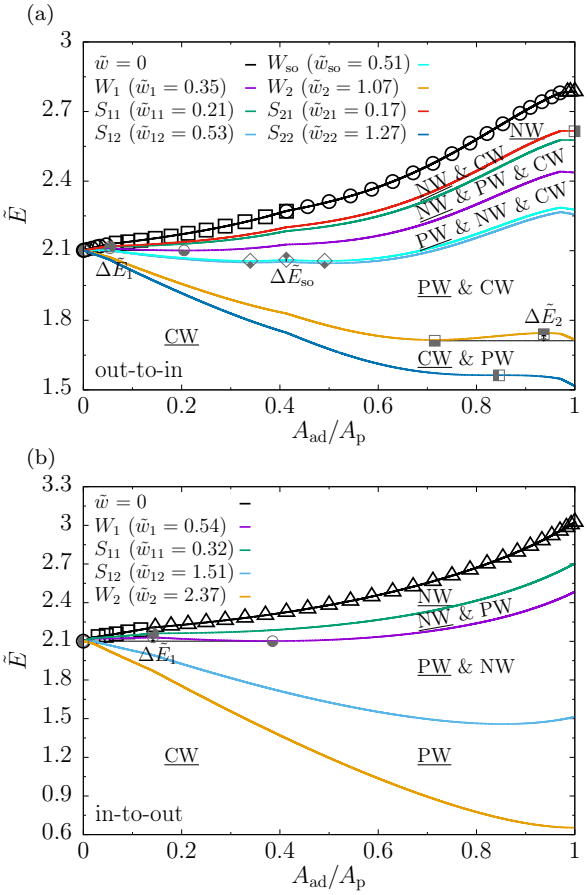

Figure 3.2: Reduced wrapping energies $\tilde{E}$ as function of the wrapping fraction A_{ad}/A_p for (a) out-to-in and (b) in-to-out wrapping. The reduced particle size is $\tilde{R}_p = 0.25$, the reduced volume is $v = 0.6515$, and the reduced spontaneous curvature is $\tilde{c}_0 = -0.032$. Different reduced adhesion strengths $\tilde{w}$ associated with wrapping or shape transitions are shown. The open squares, circles and triangles are numerical results for stomatocyte, oblate and prolate vesicles wrapping spherical particles, respectively. The black lines are fit functions. The labels for non-wrapped (NW), partial-wrapped (PW) and complete-wrapped (CW) states are underlined if the states are stable and not underlined if they are metastable. W_1 is the binding transition, W_2 is the envelopment transition, and W_{so} is the shape transition between stomatocytes and oblates. S_{11} and S_{12}, S_{21} and S_{22} are spinodals associated with W_1 and W_2, respectively. $\Delta\tilde{E}_1$ and $\Delta\tilde{E}_2$ are energy barriers between NW and PW for W_1, PW and CW for W_2, respectively; $\Delta\tilde{E}_{so}$ is the energy barrier between two PW states. For the transition W_1 / W_2, the partial-wrapped state that corresponds to the non-wrapped/complete-wrapped state is indicated by p_1 (◒) / p_5 (⬓) and the energy barrier by p_2 (◓) / p_6 (⬒). The energy barrier vanishes at p_3 (◐) / p_7 (◧) for spontaneous wrapping, and at p_4 (◑) / p_8 (◨) for spontaneous unwrapping. The two partial-wrapped states between that the shape transition takes place are indicated by ◈ and the energy barrier inbetween by ◈ .

properties. The bending energy is calculated using the Helfrich Hamiltonian

[19, 20]

$$E_{\mathrm{b}} = \int_A \mathrm{d}S \, \left[2\kappa(H - c_0)^2 + \bar{\kappa}K\right] , \tag{3.1}$$

as integral over the entire membrane area A. The elastic parameters are the bending rigidity κ, the spontaneous curvature c_0, and the Gaussian saddle-splay modulus $\bar{\kappa}$. Finite spontaneous curvatures originate from an asymmetry of the membrane or its environment, e.g. from different shapes or kinds of lipid molecules in the monolayers that form the bilayer [181]. The mean curvature $H = (c_1 + c_2)/2$ and the Gaussian curvature $K = c_1 c_2$ describe the local shape of the membrane, where c_1 and c_2 are the membrane's principle curvatures.

The total energy for particle wrapping is

$$E = 2\kappa \int_A \mathrm{d}S \, (H - c_0)^2 + pV + \gamma A - w \int_{A_{\mathrm{ad}}} \mathrm{d}S \, , \tag{3.2}$$

where the deformation-energy cost for the lipid bilayer has to be overcome by the adhesion-energy gain for contact of membrane and particle. The adhesion strength w contributes over the area A_{ad}, where the membrane is adhered to the particle. Here, we neglect the final step of pinching off the neck of a complete-wrapped particle when the topology of the system would change. According to the Gauss-Bonnet theorem, the contribution of the saddle-splay modulus is constant if the topology does not change and can therefore be neglected for the energy calculations. Equation (3.2) models the energy of a closed vesicle, where pressure p and membrane tension γ are the Lagrange multipliers that fix the volume V and the membrane area A of the vesicle. We use dimensionless parameters $\tilde{E} = E/(8\pi\kappa)$, $\tilde{w} = wR_{\mathrm{p}}^2/(2\kappa)$, $\tilde{c}_0 = c_0/c_{\mathrm{p}}$, and $\tilde{R}_{\mathrm{p}} = R_{\mathrm{p}}/R_{\mathrm{v}}$ for energy, adhesion strength, spontaneous curvature, and the reduced particle radius [1], respectively.

3.2.2 Calculating and characterizing wrapping and shape transitions

The vesicle shapes including stomatocyte, oblate and prolate are axisymmetric in our models, we calculate membrane bending energies as function of the wrapping fraction $A_{\mathrm{ad}}/A_{\mathrm{p}}$ for particles, where A_{p} is the total surface area of the particle; the initial contact points of the spherical particles with the membrane are the high-symmetry poles of the vesicles. Using triangulated membranes [12, 123, 145], we numerically obtain deformation energies for constant wrapping fractions of the particles with the help of the freely available

[1] We vary the reduced particle radius by changing the vesicle radius radius R_{v}.

software package "Surface Evolver" [182]. Figure 3.2 shows the total energies and the wrapping fractions for different adhesion strengths. Which vesicle shapes are stable depends on the wrapping fraction; we plot the energies for the shapes with the lowest energies. For example, in our calculations for out-to-in wrapping, see Fig. 3.2(a), oblates (open circles) are stable at small wrapping fractions, followed by stomatocytes (open squares), again oblates, and prolates (open triangles) with increasing wrapping fraction. For in-to-out wrapping, see Fig. 3.2(b), we find a shape sequence of stable oblates, stomatocytes, and prolates with increasing wrapping fraction.

The piecewise functions are used to fit the reduced deformation energies $\tilde{E}(A_{\mathrm{ad}}/A_{\mathrm{p}})$, the different pieces correspond to the different vesicle shapes. In each region, the fit functions are polynomials with degree six,

$$f\left(\frac{A_{\mathrm{ad}}}{A_{\mathrm{p}}}\right) = \sum_{i=0}^{6} a_i \left(\frac{A_{\mathrm{ad}}}{A_{\mathrm{p}}}\right)^i , \tag{3.3}$$

with fit parameters a_0, ..., a_6. The total reduced energy at finite reduced adhesion strength $\tilde{w}$ is

$$\tilde{E} = f\left(\frac{A_{\mathrm{ad}}}{A_{\mathrm{p}}}\right) - \tilde{w}\frac{A_{\mathrm{ad}}}{A_{\mathrm{p}}} . \tag{3.4}$$

The analysis of the extrema and the saddle points of the fit functions for various adhesion strengths generates stable states, energy barriers, wrapping and shape transitions, and spinodals.

For both out-to-in and in-to-out wrapping, the bending energies increase with increasing wrapping fraction, see Fig. 3.2. A globally stable non-wrapped state exists for small adhesion strengths. Partial-wrapped and complete-wrapped states are determined as usual [15, 16, 147]. For finite homogeneous adhesion strengths, the adhesion-energy gain increases linearly with the wrapping fraction. It is added to the numerically calculated deformation-energy costs. Subsequently, the global minimum of the total energy is determined. The binding transitions W_1 to a partial-wrapped state occur at a reduced adhesion strength $\tilde{w}_1$, where the deformation energies of the non-wrapped state and a partial-wrapped state are equal. Increasing the adhesion strength further, we find an envelopment transition W_2 between a partial-wrapped state and the complete-wrapped state at a reduced adhesion strength $\tilde{w}_2$. For $\tilde{w} < \tilde{w}_1$ the non-wrapped state is stable, for $\tilde{w}_1 < \tilde{w} < \tilde{w}_2$ a partial-wrapped state is stable, and for $\tilde{w} > \tilde{w}_2$ the complete-wrapped state is stable.

Besides the wrapping transitions between non-wrapped, partial-wrapped and complete-wrapped states, non-spherical vesicles can have different stable shapes. The shapes of vesicles without attached particles are completely determined by both the reduced volume [11, 183] of the vesicle and the spontaneous

curvature c_0 of the membrane. Here, $V_0 = 2\sqrt{\pi}A^{3/2}/3$ is the maximal volume that can be enclosed by the membrane area A. Particles effectively change the reduced volume and partial-wrapped particles in addition provide boundary conditions for the slope of the free membrane and therefore also stabilize certain vesicle shapes. Different stable shapes are separated by energy barriers, as indicated by the various symbols in Fig. 3.2.

$$v = \frac{V}{V_0} \leq 1 \tag{3.5}$$

For adhesion strength $\tilde{w}_1$, where the partial-wrapped state indicated by p_1 has the same energy as the non-wrapped state, the energy barrier $\Delta\tilde{E}_1$ for the binding transition is obtained by subtracting the energy at the minimum p_1 from the energy at the maximum p_2. The saddle points p_3 and p_4 correspond to the spinodals S_{11} and S_{12}, respectively, for the adhesion strengths $\tilde{w}_{11}$ and $\tilde{w}_{12}$ where the energy barrier vanishes. Analogously, for adhesion strength $\tilde{w}_2$ the partial-wrapped state is indicated by p_5 and the energy maximum that corresponds to $\Delta\tilde{E}_2$ by p_6. The wrapping factions indicated by p_7 and p_8 are the saddle points for the spinodals S_{22} and S_{21} at adhesion strengths $\tilde{w}_{21}$ and $\tilde{w}_{22}$, respectively.

For out-to-in wrapping and reduced particle size $\tilde{R}_\mathrm{p} = 0.25$, reduced volume $v = 0.6515$ and reduced spontaneous curvature $\tilde{c}_0 = -0.032$, as shown in Fig. 3.2(a), both binding and envelopment transitions W_1 and W_2 are discontinuous with energy barriers $\Delta\tilde{E}_1 = 0.01$ and $\Delta\tilde{E}_2 = 0.03$, respectively. A discontinuous shape transition between a stomatocyte and an oblate is found for $\tilde{w} = \tilde{w}_\mathrm{so}$ between two partial-wrapped states. A small energy barrier $\Delta\tilde{E}_\mathrm{so} = 0.005$ is associated with this shape transition W_so. For in-to-out wrapping, as shown in Fig. 3.2(b), the binding transition W_1 between the non-wrapped state and a partial-wrapped state is discontinuous and is characterized by an energy barrier $\Delta\tilde{E}_1 = 0.03$, whereas the envelopment transition W_2 between a partial-wrapped state and the complete-wrapped state is continuous without an energy barrier.

For adhesion strengths $\tilde{w}_{11} < \tilde{w} < \tilde{w}_1$, a metastable partial-wrapped state coexists with the stable non-wrapped state. For adhesion strengths $\tilde{w}_1 < \tilde{w} < \tilde{w}_{12}$, the metastable non-wrapped state coexists with a stable partial-wrapped state. An energy barrier $\Delta\tilde{E}_2$ between a partial-wrapped state and the complete-wrapped state indicates that the envelopment transition W_2 is discontinuous. S_{21} and S_{22} are spinodals; for adhesion strengths $\tilde{w}_{21} < \tilde{w} < \tilde{w}_2$, a stable non-wrapped or partial-wrapped state coexists with a metastable complete-wrapped state, for adhesion strengths $\tilde{w}_2 < \tilde{w} < \tilde{w}_{22}$ the stable complete-wrapped state coexists with a metastable partial-wrapped state.

3.3 Results

3.3.1 Wrapping diagrams

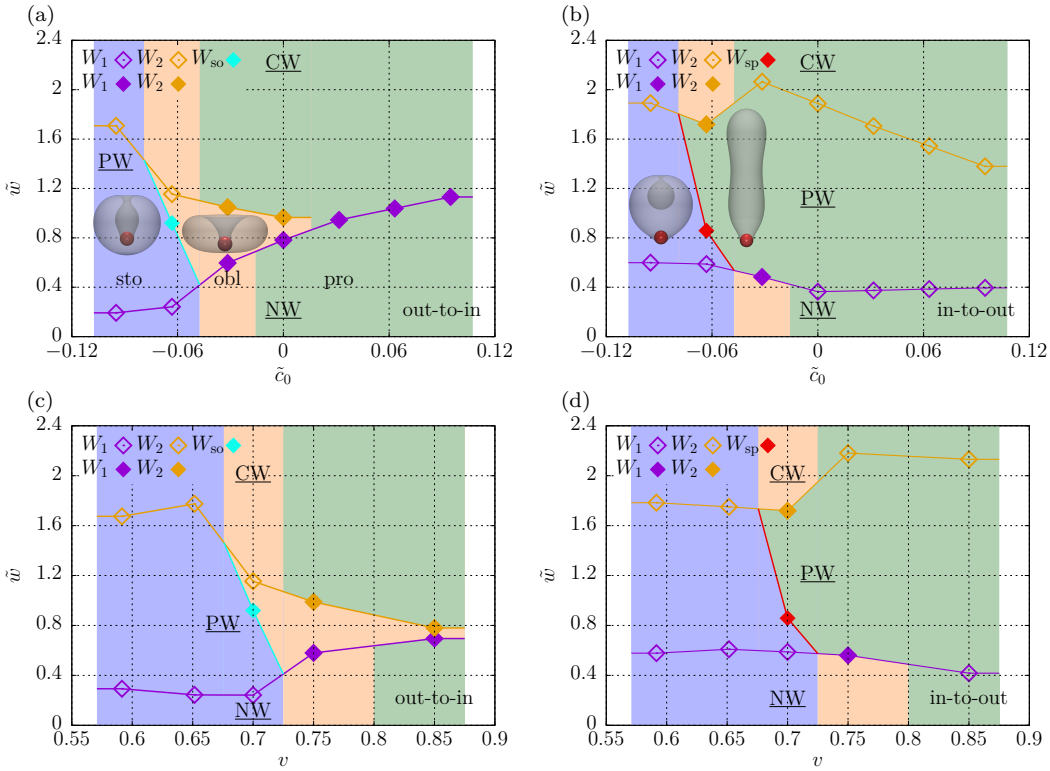

Figure 3.3: Reduced adhesion strengths $\tilde{w}$ for reduced particle size $\tilde{R}_\mathrm{p} = 0.2$, (a, b) for $v = 0.7$ as function of the reduced spontaneous curvature $\tilde{c}_0$, (c, d) for $\tilde{c}_0 = -0.063$ as function of the reduced volume v for out-to-in and in-to-out wrapping. The continuous and discontinuous wrapping transitions W_1 and W_2 without and with energy barriers are shown by open and solid diamonds, respectively. The stable stomatocyte, oblate, and prolate shapes are indicated by sky-blue, orange, and green background colors, respectively. The shape transitions W_so between stomatocytes and the oblates, and W_sp between stomatocytes and prolates are colored by cyan and red diamonds, respectively. The other labels are chosen analogously to Fig. 3.2; the non-wrapped (NW) state is stable below the W_1 transition, the partial-wrapped state (PW) between the W_1 and the W_2 transitions, and the complete-wrapped state (CW) above both transitions.

We first analyze the reduced adhesion strengths $\tilde{w}$ associated with wrapping and shape transitions for various reduced spontaneous curvatures and reduced volumes. Wrapping and shape transitions for reduced particle size $\tilde{R}_\mathrm{p} = 0.2$, reduced volume $v = 0.7$, and various values for reduced spontaneous curvatures $\tilde{c}_0$, as well as for $\tilde{c}_0 = -0.0632$ and various values of v are shown in Fig. 3.3 for both out-to-in and in-to-out wrapping. The transitions can be continuous, indicated by open diamonds, or discontinuous, indicated by solid diamonds.

For out-to-in wrapping, stable partial-wrapped states are found for $\tilde{c}_0 \leq 0$, see Fig. 3.3(a). The adhesion strengths $\tilde{w}_1$ associated with the binding or the binding-envelopment transition W_1 between the non-wrapped and a stable partial-wrapped or the complete-wrapped state increase with increasing $\tilde{c}_0$, while the values of $\tilde{w}_2$ for the envelopment transition W_2 between a stable partial-wrapped and the complete-wrapped state decrease with increasing $\tilde{c}_0$. For stable partial-wrapped states, the vesicle shapes are either stomatocytes or oblates. At $\tilde{c}_0 = -0.063$, the shape transition W_{so} takes place at $\tilde{w}_{\mathrm{so}} = 0.92$; stomatocytes are stable for more negative $\tilde{c}_0$, while oblates are stable for more positive $\tilde{c}_0$. The shape transitions for both the non-wrapped and the complete-wrapped states can be predicted based on Ref. [172], which we discuss in the subsection on shape transitions. Discontinuous binding and envelopment transitions, W_1 and W_2, are found for $\tilde{c}_0 = -0.032$ and $\tilde{c}_0 = 0$; the energy barriers mostly result from shape transitions. Also the combined binding-envelopment transitions W_1 between prolates are discontinuous.

Qualitatively the transitions depend in a similar way on the reduced volume v as on $\tilde{c}_0$, see Fig. 3.3(c). In the partial-wrapped state the vesicles are stomatocytes and oblates, and the wrapping transitions get closer to each other with increasing v. Discontinuous transitions are found for $v = 0.75$ and 0.85, which are mostly associated with shape transitions.

For in-to-out wrapping, partial-wrapped states are found for all values of $\tilde{c}_0$, see Fig. 3.3(b). The adhesion strengths $\tilde{w}_1$ for the binding transitions, and $\tilde{w}_2$ for the envelopment transitions are non-monotonic with $\tilde{c}_0$, which reflects shape transitions. The binding transition W_1 is discontinuous at $\tilde{c}_0 = -0.032$, and the envelopment transition W_2 is discontinuous at $\tilde{c}_0 = -0.063$; both are associated with shape transitions. For $\tilde{c}_0 = -0.063$, the shape transition W_{sp} between stomatocytes and prolates takes place at $\tilde{w}_{\mathrm{sp}} = 0.86$ between two partial-wrapped states. Stomatocytes are stable for more negative $\tilde{c}_0$, while prolates are stable for more positive $\tilde{c}_0$.

As shown in Fig. 3.3(d), the dependence of the adhesion strengths for the wrapping transitions on the reduced volume v is similar to that on $\tilde{c}_0$: both $\tilde{w}_1$ and $\tilde{w}_2$ are non-monotonic. For the partial-wrapped states, stomatocytes are stable for small v, and oblates are stable for large v. The discontinuous transitions coincide with shape transitions.

3.3.2 Wrapping transitions

Wrapping and shape transitions can be both continuous and discontinuous. The systems for $\tilde{R}_{\mathrm{p}} = 0.2$ and $v = 0.7$, marked by boxes in Fig. 3.4, have been discussed in detail in Fig. 3.3. The reduced adhesion strength $\tilde{w}_1$ for the binding transition W_1 increases both with increasing $\tilde{c}_0$ and with increasing reduced volume v for out-to-in wrapping and is non-monotonic for in-to-out

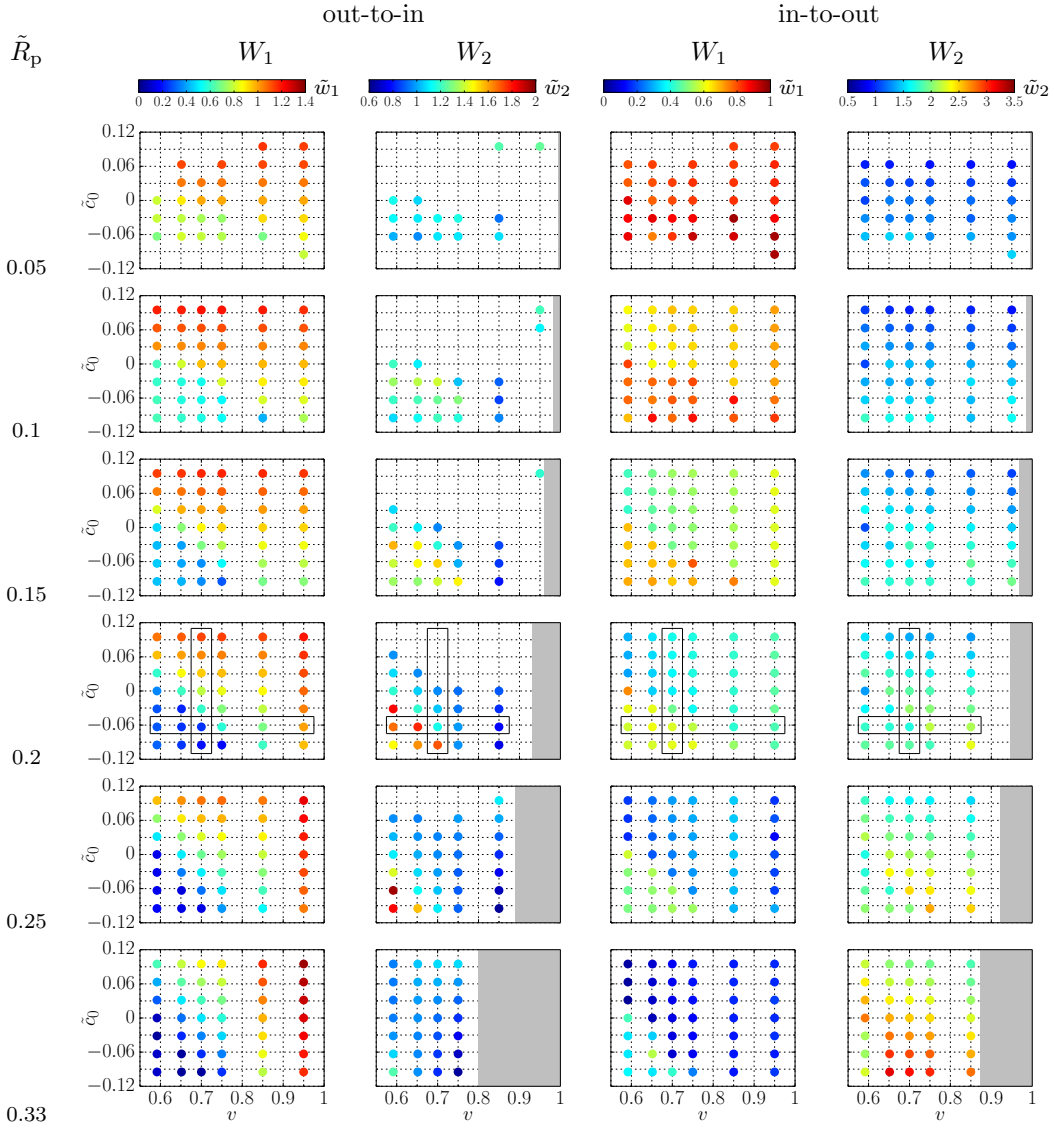

Figure 3.4: Reduced adhesion strengths $\tilde{w}_1$ and $\tilde{w}_2$ for the wrapping transitions W_1 and W_2, respectively. Data is shown for out-to-in and in-to-out wrapping and for various reduced particle sizes $\tilde{R}_\mathrm{p}$, reduced volumes v, and reduced spontaneous curvatures $\tilde{c}_0$. Complete-wrapped states are not accessible in the grey-shaded areas due to lack of membrane area. The wrapping transitions for $\tilde{R}_\mathrm{p} = 0.2$ and $v = 0.7$ shown in Figs. 3.3(a, b), and for $\tilde{c}_0 = -0.063$ shown in Figs. 3.3(c, d) are marked.

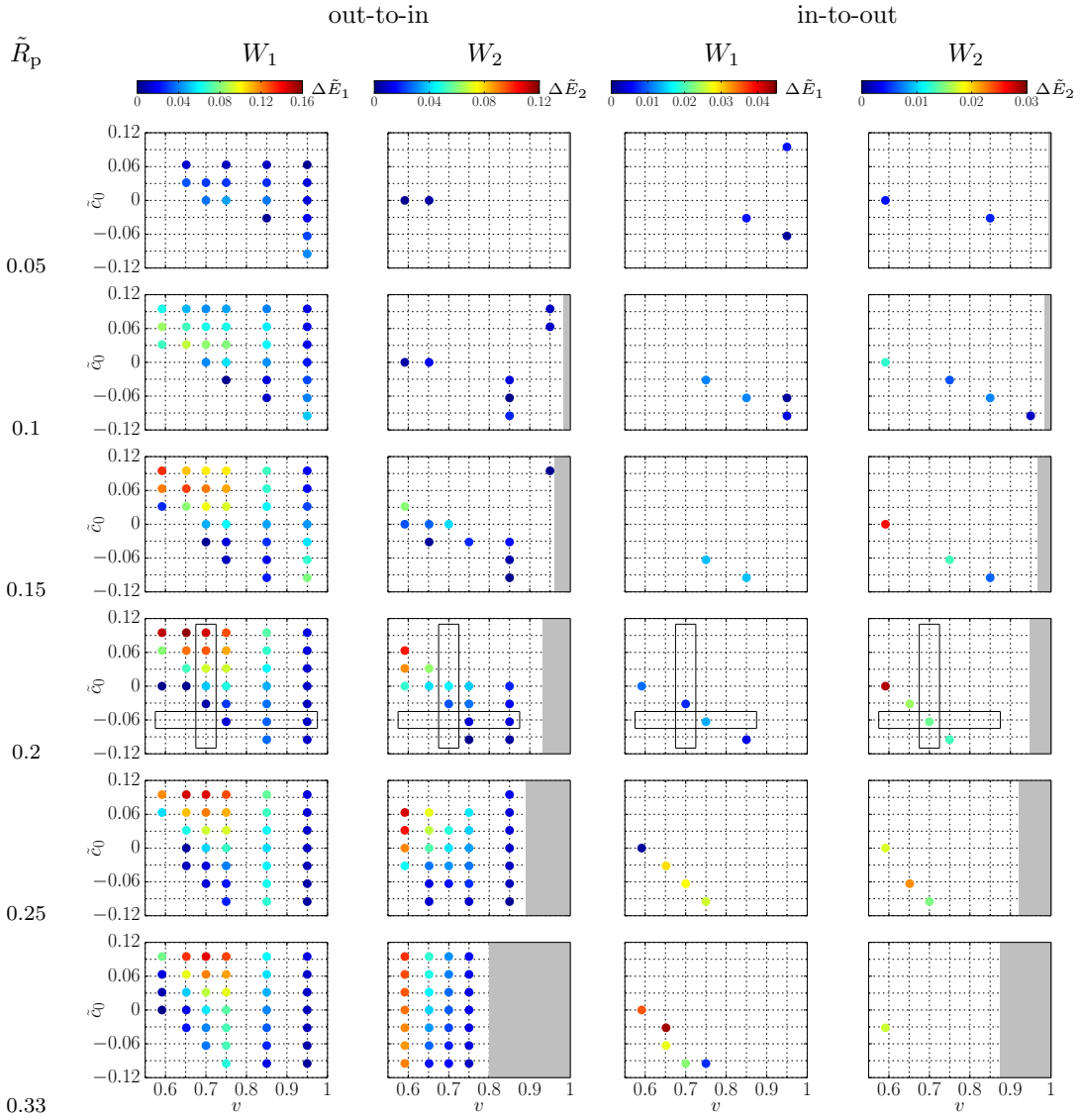

Figure 3.5: Energy barriers $\Delta\tilde{E}_1$ and $\Delta\tilde{E}_2$ for the wrapping transitions W_1 and W_2, respectively. Data is shown for out-to-in and in-to-out wrapping and for various reduced particle sizes $\tilde{R}_\mathrm{p}$, reduced volumes v, and reduced spontaneous curvatures $\tilde{c}_0$. Complete-wrapped states are not accessible in the grey-shaded areas due to lack of membrane area. The wrapping transitions for $\tilde{R}_\mathrm{p} = 0.2$ and $v = 0.7$ shown in Figs. 3.3(a, b), and for $\tilde{c}_0 = -0.063$ shown in Figs. 3.3(c, d) are marked.

wrapping. The reduced adhesion strength $\tilde{w}_2$ for the envelopment transition W_2 decreases with increasing $\tilde{c}_0$ for out-to-in wrapping and is non-monotonic with increasing $\tilde{c}_0$ and v in the other cases. Wrapping transitions without energy barriers are shown by open diamonds in Fig. 3.3, those with barriers by full diamonds. Figure 3.4 shows an overview over the wrapping transitions $\tilde{w}_1$ and $\tilde{w}_2$ for wide ranges of parameters: $0.05 \leq \tilde{R}_\mathrm{p} \leq 0.33$, $0.5915 \leq v \leq 0.95$, and $-0.095 \leq \tilde{c}_0 \leq 0.095$.

We first consider out-to-in wrapping. For large reduced particle sizes $\tilde{R}_\mathrm{p}$, small reduced volumes v, and small or negative spontaneous curvatures $\tilde{c}_0$, the reduced adhesion strengths $\tilde{w}_1$ for the binding transition W_1 are small; this indicates that the onset of wrapping is easy. A separate envelopment transition W_2 exists for large reduced particle sizes, small reduced volumes, and small or negative spontaneous curvatures. For small reduced particle sizes, large reduced volumes, and high spontaneous curvatures, we find a discontinuous, direct transition from the non-wrapped to the complete-wrapped state. The adhesion strength $\tilde{w}_1$ for combined binding-envelopment transition is higher than for transition from the non-wrapped to a partial-wrapped state.

For in-to-out wrapping, individual binding and envelopment transitions and stable partial-wrapped states exist for nearly all systems. For large $\tilde{R}_\mathrm{p}$, small v, and mostly small and positive $\tilde{c}_0$, the adhesion strength for the binding transition W_1 is small. High adhesion strengths for the envelopment transition W_2 are found in particular for large $\tilde{R}_\mathrm{p}$, small v, and small or negative $\tilde{c}_0$.

Energy barriers for out-to-in wrapping transitions are shown in Fig. 3.5. The binding transition W_1 is continuous for small reduced volumes v and for small or negative spontaneous curvatures $\tilde{c}_0$. The energy barrier for the binding transition is high for large $\tilde{R}_\mathrm{p}$, small and intermediate v, and positive $\tilde{c}_0$. The envelopment transition W_2 is continuous without an energy barrier for small v and for small $\tilde{c}_0$. The energy barrier for the envelopment transition is high in particular for small reduced volumes v. A higher energy barrier is found for $\tilde{R}_\mathrm{p} = 1/3$ or for very small v and very positive $\tilde{c}_0$.

For in-to-out wrapping, energy barriers are only found along lines in the $\tilde{c}_0$-v-plane that correspond to the boundaries where shape changes of vesicles occur, see Fig. 3.5. These energy barriers are only about 1/4 as high as those for out-to-in wrapping.

3.3.3 Shape transitions

The shapes of vesicles before and after particle wrapping are determined by the old and new reduced volumes and by membrane spontaneous curvature. In Fig. 3.6, we plot the reduced volumes of vesicles after complete wrapping for various initial reduced volumes and reduced particle sizes, see supporting information. For large reduced particle sizes and high reduced volumes, not

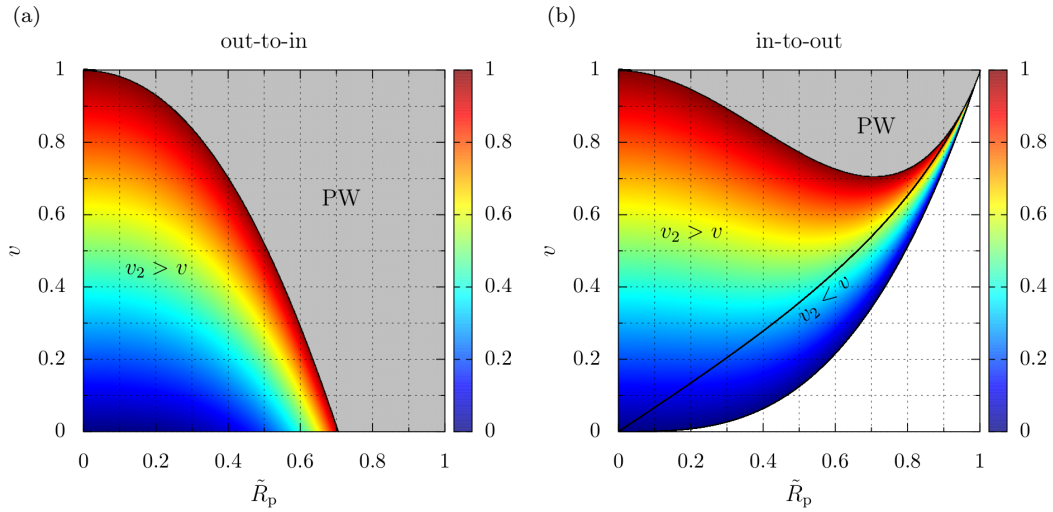

Figure 3.6: Reduced vesicle volumes v_2 after complete wrapping for (a) out-to-in and (b) in-to-out wrapping for various reduced particle sizes $\tilde{R}_\mathrm{p}$ and reduced volumes v prior to wrapping. The black line indicates the parameters for that the reduced volume remains unchanged upon wrapping. Complete-wrapped states are not accessible in the grey-shaded areas due to lack of membrane area; the particle cannot be placed inside the vesicle in the white area.

enough membrane area is available to completely wrap the nanoparticle. The particle will therefore at most attach to the membrane and never reach the complete-wrapped state. For in-to-out wrapping, vesicles with reduced volumes for which the particle volume is larger than the vesicle volume do not exist.

For out-to-in wrapping, the vesicle volume increases by the particle volume, while its membrane area decreases by the particle surface area. Therefore, the vesicles' reduced volumes after complete wrapping are larger than prior to wrapping. For in-to-out wrapping, both the vesicle volume as well as the vesicle area decrease. Here, the reduced volume after wrapping increases in most cases, but decreases if a particle initially occupies a large fraction of the vesicles' volume.

Figure 3.7 shows vesicle shape diagrams for $\tilde{R}_\mathrm{p} = 0.2$ and various v and $\tilde{c}_0$ for all wrapping states of the particle: non-wrapped, partial-wrapped, and complete-wrapped. The vesicle shapes prior to wrapping are taken from Ref. [172], the shapes after complete wrapping are calculated based on Fig. 3.6 and Ref. [172]. For the non-wrapped and the complete-wrapped states, the transitions between prolates, oblates, and stomatocytes, as well as the transitions between stomatocytes and inside vesiculation are indicated by lines, see Figs. 3.7(a) and (b). For both out-to-in and in-to-out wrapping, the parameter regions for stomatocytes, oblates, and prolates shift to smaller reduced volumes after complete wrapping. For example, for $\tilde{c}_0 = -0.063$ prior to wrapping

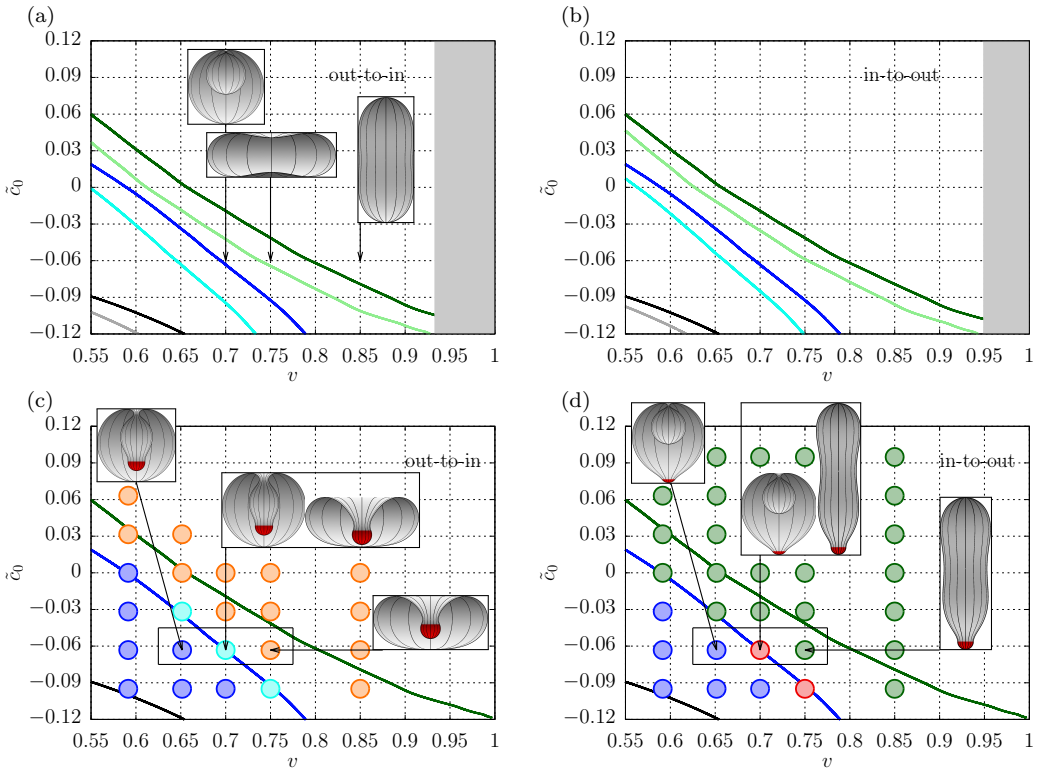

Figure 3.7: Vesicle shapes for $\tilde{R}_\mathrm{p} = 0.2$ for out-to-in and in-to-out wrapping. (a, b) The prolate-oblate (green), the oblate-stomatocyte (blue), and the inside-vesiculation (black) transitions are indicated. The transitions prior to wrapping are indicated by dark colors [172], transitions after complete wrapping by light colors (calculated based on Ref. [172] and Fig. 3.6). Snapshots of stomatocytes, oblates, and prolates prior to wrapping are shown for $\tilde{c}_0 = -0.063$, and $v = 0.7$, 0.75 and 0.85. (c, d) The points indicate the stable shapes for partial-wrapped states: skyblue represents stomatocytes, orange oblates, green prolates, cyan stomatocytes and oblates, and red stomatocytes and prolates. From left to right, the wrapping fractions are $A_\mathrm{ad}/A_\mathrm{p} = 0.54$, 0.55, 0.71 and 0.71 for the snapshots shown in (c), and 0.21, 0.21, 0.5, and 0.5 for the snapshots shown in (d).

stomatocytes are stable for $v < 0.7$, oblates for $0.7 < v < 0.8$, and prolates for $v > 0.8$ [172]. After complete out-to-in wrapping, oblates are stable for $0.65 < v < 0.75$, and after complete in-to-out wrapping for $0.67 < v < 0.76$.

The vesicle shapes for the partial-wrapped states are indicated by the colors of the points, see Figs. 3.7(c) and (d). For partial-wrapped particles, not only reduced volume and spontaneous curvature determine the vesicle shape, but also the boundary conditions at the particle. For out-to-in wrapping, partial-wrapped particles stabilize oblate shapes; for in-to-out wrapping, partial-wrapped particles stabilize prolate shapes. We find direct transitions between stomatocytes and oblates for out-to-in wrapping and between stomatocytes and prolates for in-to-out wrapping. As shown in Fig. 3.3, upon wrapping vesicles may also experience discontinuous shape transitions between two

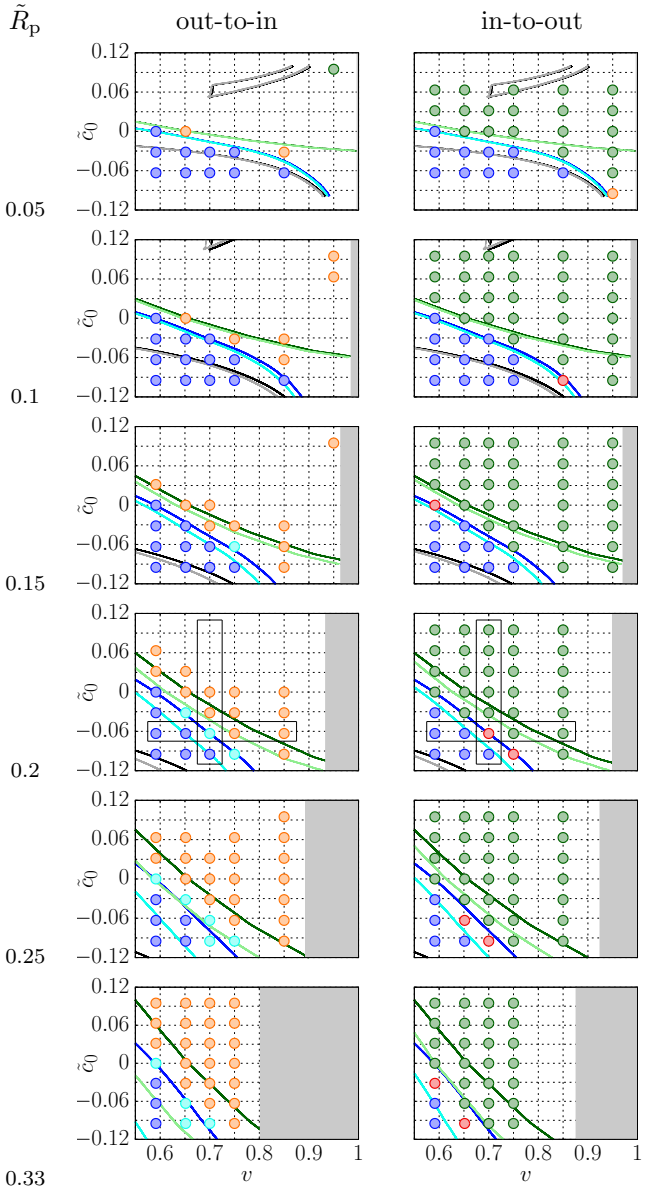

Figure 3.8: Vesicle shapes for different reduced particle sizes $\tilde{R}_\mathrm{p}$, reduced volumes v, and reduced spontaneous curvatures $\tilde{c}_0$. Analogously to Fig. 3.7, shape transitions for non-wrapped and complete-wrapped states are indicated by lines, partial-wrapped states by points. Fission and pear transitions for the non-wrapped and the complete-wrapped states are indicated by the black and grey lines, respectively. The stable shapes shown in Figs. 3.3 and 3.7 are marked.

partial-wrapped states.

For out-to-in wrapping, below the transition, $\tilde{c}_0 \approx 0.4 - 0.65\,v$, stomatocytes are stable; above the transition oblates are stable. For in-to-out wrapping, below the transition, $\tilde{c}_0 \approx 0.25 - 0.45\,v$, stomatocytes are stable; above the transition prolates are stable. Stable shapes for specific values for v and $\tilde{c}_0$ are shown.

Results of similar calculations of the shapes for wide ranges of the vesicle parameters, $0.05 \leq \tilde{R}_\mathrm{p} \leq 0.33$, $0.5915 \leq v \leq 0.95$, and $-0.95 \leq \tilde{c}_0 \leq 0.95$, are summarized in Fig. 3.8, where the data shown in Figs. 3.3 and 3.7 are marked. In addition to stomatocytes, oblates and prolates, we calculate shapes in parameters regimes with inside-vesiculation, fission, and pears. In these regimes, partial-wrapped states may not be stable and are therefore only shown in some cases. The presence of partial-wrapped states at small $\tilde{R}_\mathrm{p}$, high v, and high $\tilde{c}_0$ shows the competition between the actual membrane curvature and the spontaneous membrane curvature. For out-to-in wrapping and vanishing spontaneous curvature, partial-wrapped states are suppressed by the membrane curvature [14], while positive spontaneous curvatures favor partial-wrapped states [13]. For reduced volumes $v = 0.5915$, small $\tilde{R}_\mathrm{p}$, and high $\tilde{c}_0$, attachment of particles induces vesicle fission. Therefore, vesicle shapes are not indicated in this parameter regime.

3.4 Discussion

Minimising the energy for fixed reduced vesicle volume and spontaneous membrane curvature at the same time, brings a new dimension to the study of nanoparticle interactions with biovesicles. In addition to the deformation energy for the membrane wrapping of a nanoparticle, vesicle shapes and shape changes are key to understanding nanoparticle-vesicle interactions. For membrane-bound nanoparticles at planar membranes, the free membrane can assume catenoidal or catenoid-like shapes with only small bending-energy costs; the deformation energy of the free membrane before and after wrapping is unchanged [16]. In contrast, for systems where the vesicle radius is comparable to the radius of the nanoparticle, the free membrane contributes substantially to the energy changes upon wrapping [184]. The deformation energy of the free membrane before and after wrapping are solely determined by the old and new reduced volumes of the vesicles. For example, for $c_0 = 0$, if the effective reduced volume after wrapping has increased, the vesicle shape is closer to the optimal spherical shape, which reduces the deformation energy [172, 183].

The direct binding-envelopment transition without an energy barrier, which is observed for spherical nanoparticles at planar membranes, disappears for membranes that are curved prior to particle attachment [14]. While for out-to-in wrapping of a particle at a tensionless vesicle the combined binding-

envelopment transition becomes discontinuous, for in-to-out wrapping both the binding and the envelopment transitions are continuous. In the latter case, for all wrapping fractions $0 < A_{\mathrm{ad}}/A_{\mathrm{p}} < 1$, stable partial-wrapped states exist.

Not only the membrane curvature prior to wrapping at the place where the nanoparticle attaches, but also a spontaneous curvature of the lipid-bilayer membrane is an important parameter for nanoparticle wrapping. For almost planar membranes, the total energy for the complete-wrapped state is reduced compared with $c_0 = 0$ if the sign of the spontaneous curvature coincides with the curvature of the nanoparticle surface. The combined binding-envelopment transition is discontinuous with an energy barrier [13]. However, if the sign of the spontaneous curvature is opposite to the sign of the particle surface curvature, the energy of the complete-wrapped state increases compared with the $c_0 = 0$ case; both the binding and the envelopment transition are continuous and separated by partial-wrapped states. In agreement with Ref. [13], we find continuous binding transitions at comparatively small adhesion strengths if the spontaneous curvature and the particle surface curvature have the same signs. The binding transitions in these cases occur at higher adhesion strengths than in cases where spontaneous curvature and particle surface curvature have opposite signs.

The distribution of half-adhesive nanoparticles on non-spherical vesicles has been investigated in Ref. [148]. For small $\tilde{R}_{\mathrm{p}} = 0.01$ and reduced volumes in the range $0.4 < v < 0.8$, the deformation-energy differences between different binding locations have been found to be of the order of $0.1\,\kappa$, which drives relocation of partial-wrapped nanoparticles on curved membranes. Contrary to the small values $\tilde{R}_{\mathrm{p}}$ studied in Ref. [148] where the vesicles shape changes upon nanoparticle binding are small, for the systems with high $\tilde{R}_{\mathrm{p}}$ studied in this paper transitions to axisymmetric shapes can be expected to occur during wrapping. The stable oblates that we observe can therefore be expected for out-to-in wrapping in the regime where bare vesicles are prolates, and stable prolates or stomatocytes in the regime where bare vesicles are oblates.

A clear correlation is observed between the adhesion strengths for the transitions, the energy barriers, and the vesicle shapes, see Figs. 3.4, 3.5 and 3.8, respectively, as well as Fig. S2 in the supporting information. For out-to-in wrapping, the binding transition for stomatocytes occurs already at small adhesion strengths $\tilde{w}_1$, because the membrane is strongly curved towards the particle; intermediate values of $\tilde{w}_1$ are found for oblates and high values for prolates. Partial-wrapped states are particularly stable for stomatocytes and a direct binding-envelopment transition occurs for prolates. For in-to-out wrapping, the adhesion strength for the binding transition is comparatively high for oblates and stomatocytes at small particle-to-vesicle size ratios, while high adhesion strengths for the envelopment transition are found both for stomato-

cytes and for prolates at large particle-to-vesicle size ratios. Furthermore, for out-to-in wrapping, a high energy barrier has to be overcome for binding for prolate vesicles in the non-wrapped state, see Fig. 3.5. Similarly, a high energy barrier has to be overcome for envelopment for vesicles with small reduced volumes. For in-to-out wrapping, energy barriers only occur for parameter values close to shape transitions.

We have calculated wrapping transitions for a large variety of axisymmetric nanoparticle-vesicle systems. However, because of the inhomogeneous membrane curvatures for prolates, oblates, and stomatocytes, the optimal position for nanoparticle attachment is not always a position of highest symmetry [185]. In the case of small reduced volumes v, for out-to-in wrapping the nanoparticle is expected to attach in the position of smallest curvature, where we also attach the particles for stomatocytes and oblates in our calculations. However, for prolates the lowest deformation energy costs for small wrapping fractions are expected for an attachment at the side of a vesicle, while we calculate the deformation energy for the highly-curved tip position. Similarly, for in-to-out-wrapping and prolates, the point of highest symmetry at the tip of the vesicle is the lowest-energy position where we place the nanoparticle for our calculations. For oblates, and perhaps also for stomatocytes, the ideal positions are expected to be close to the rim. Thus our axisymmetric calculations describe the system well in most regions of the parameter space.

3.5 Conclusions

Nanoparticles that have an attractive nanoparticle-membrane interaction and that are larger than the thickness of the lipid bilayer can experience passive endocytosis and get wrapped. Nanoparticle attachment and envelopment at small vesicles is affected by vesicle shape and can vice versa affect vesicle shape transitions. We have systematically investigated the interaction of spherical nanoparticles with vesicles for reduced particle sizes in the range $0.05 \leq \tilde{R}_\mathrm{p} \leq 0.33$, for various reduced volumes in the range $0.5915 \leq v \leq 0.95$, and for reduced spontaneous membrane curvatures in the range $-0.095 \leq \tilde{c}_0 \leq 0.095$. As for spherical vesicles, the adhesion strength for the binding transition is reduced if the membrane is curved towards the nanoparticle, while the adhesion strength for the envelopment transition is increased; if the membrane curves away from the nanoparticle, an energy barrier for wrapping occurs [14]. All boundaries in the vesicle shape diagram shift according to the new reduced volume and the new value of $c_0 R_\mathrm{v}$ after complete wrapping. For partial-wrapped states, in addition the boundary conditions at the membrane that are locally imposed by the nanoparticles affect the vesicle shape: partial-wrapped particles stabilize oblates and stomatocytes for out-to-in wrapping and prolates for in-to-out wrapping. Finite spontaneous

membrane curvatures with a sign that is opposite to the particle curvature induce partial-wrapped states, whereas the same sign of spontaneous and particle curvature indicates an energy barrier [13]. The energy difference between the complete-wrapped and the non-wrapped state decreases for alike curvatures and increases for opposite curvatures.

For our non-spherical vesicles with various spontaneous curvatures, several continuous and discontinuous transitions may occur during wrapping and may also be coupled to vesicle shape transitions. Our calculations show that small reduced volumes facilitate the out-to-in binding transition — in particular for negative spontaneous curvatures. Furthermore, even for large $\tilde{R}_\mathrm{p}$, envelopment transitions still occur at small adhesion strengths.A biological mechanism where this might be exploited is autophagy, a main degradation system within cells that helps to balance synthesis and degradation of proteins [186]. Autophagosomes, vesicles with small reduced volumes, encapsulate part of the cytoplasm and then fuse with lysosomes where the encapsulated material is degraded. Although for very small reduced volumes formation of the double-membrane autophagosomes occurs spontaneously, the presence of an adhered nanoparticle or any other aggregate within the autophagosome can help to overcome the energy barrier between the open, oblate and the almost closed, stomatocyte state [187].

A second process, where a small reduced volume is important, is the invasion of the malaria parasite into human erythrocytes [159, 188]. Typical reduced volumes are $v \approx 0.6$ and the reduced particle size is $\tilde{R}_\mathrm{p} \approx 0.3$ [189]. Although the shear modulus induced by the cortical spectrin cytoskeleton and active processes during parasite invasion might reduce the importance of the deformation energy of the membrane, also in this case a small enough reduced volume is of crucial importance to allow particle entry.

Finally, extracellular vesicles have been suggested to play not only key roles in normal physiological processes, such as stem cell maintenance, tissue repair, immune surveillance, and blood coagulation, but also in the pathology of diseases, such as tumorgenesis, and the spread of viruses, amyloid-β-derived peptides, α-synuclein, and the abnormal cell surface prion protein PrP^C [190]. Therefore, extracellular vesicles may be targeted to inhibit their effect in disease propagation, and can be exploited for drug delivery. Size and shape of extracellullar vesicles and potential clustering are debated. Recent advances in superresolution microscopy provide new tools to analyse both small and large vesicles [191]. Nanovesicles with sizes of about 100 nm have recently been systematically characterized experimentally; the studies suggest that the mechanics is pressure dominated and cannot be explained by bending alone. How cytosolic constituents are recruited into extracellular vesicles is still unclear [192]. To this end, our work provides systematic predictions on the interaction of vesicles with particles, which could also be considered as models for protein

aggregates — accounting for a solute concentration/osmotic pressure-induced preferred volume of the vesicles.

Chapter 4

Osmotic pressure matters for nanoparticle-vesicle interactions

Under physiological conditions, high solute concentrations induce high osmotic pressure differences between between biological cells and their environment already for small volume changes. In many cases, the volume of a vesicle or a biological cell is therefore considered fixed. The interaction of nanoparticles with lipid-bilayer membranes can trigger passive endocytosis. In particular for vesicles where the membrane area is fixed, wrapping of the nanoparticle reduces the volume of the vesicle. Therefore in addition to membrane deformation and the particle-membrane adhesion that are usually studied, also osmotic pressures have to be included in the energy minimization. We calculate wrapping energies for spherical nanoparticles that enter and exit spherical vesicles for various initial solute concentrations, particle sizes, and vesicle sizes. The particle-vesicle binding transition is continuous and independent of osmotic pressure. The envelopment transition is discontinuous and is characterized by an energy barrier that increases with both particle-to-vesicle size ratio and osmotic pressure. Finite osmotic pressures therefore increases the stability of partial-wrapped, membrane-bound states of the particle for both entry and exit. The direct transition between the non-wrapped and the complete-wrapped state for particles that enter vesicles is replaced by transitions via partial-wrapped states. Furthermore, the osmotic-pressure difference introduces membrane tension, which can lead to lysis of the vesicles. Experimentally also lysis of bacteria and red blood cells upon interaction with nanostructured surfaces has been observed. Our calculations shed light on the conditions for tension-induced antibacterial membrane-lytic processes.

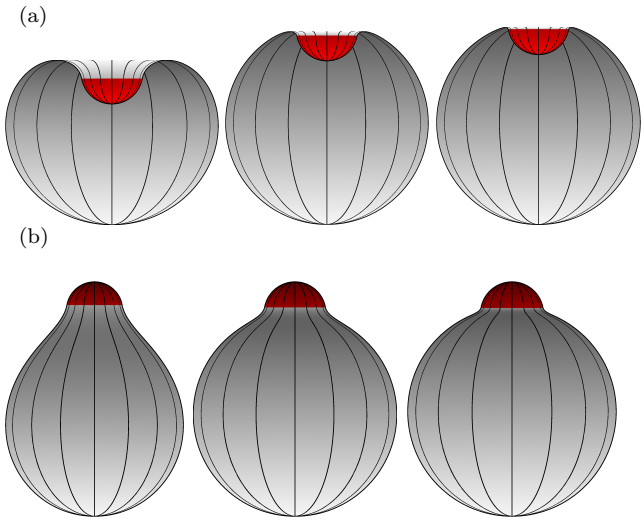

Figure 4.1: Representative shapes of vesicles and spherical nanoparticles with wrapping fractions 0.41 for (a) out-to-in and (b) in-to-out wrapping. The ratio of the radii of particles and spherical vesicles is $R_\mathrm{p}/R_\mathrm{v} = 0.3$. The osmotic constants are $\tilde{n}_\mathrm{v} = 16$, 1.6×10^4 and 1.6×10^5 from left to right. The membrane area is fixed. The adhered membrane is colored red and the free membrane white.

4.1 Introduction

Osmotic pressure is key for vesicular internalization. For instance, the endocytotic internalization rate of cells has been found to decrease linearly with increasing solute concentration in the external medium, and endocytosis is inhibited above a threshold pressure difference [193]. Endocytosis is recovered if a spontaneous curvature is generated by adding lipids to the outside monolayers that assist wrapping. For bovine adrenal medullary cells, hypotonic and hypertonic extracellular solutions lead to an increase and decrease of vesicular secretion, respectively [194]. For plant cells, an increased turgor pressure suppresses endocytosis [195]. For formation of supported lipid bilayers from vesicles, high external salt concentrations promote the formation of the supported lipid bilayer [196, 197]. A recent study, where nanovesicles with sizes of about 100 nm have been deformed using the tip of an atomic force microscope, shows that under physiological conditions the stiffness of adherent vesicles is dominated by osmotic pressure [198]. These experimental studies indicate that the osmotic pressure can be used to control shape, deformability, and stability of vesicles.

Nanoparticles and nanostructures have antibacterial properties. Not in all cases the reason for the toxic effect on bacteria is known and there is certainly more than one possible mechanism. However, antibacterial properties have been demonstrated both for engineered surfaces, as well as for the nanostructured wings of the dragonfly [199–201]. In these cases, the the adhesion to

the nanostructures induces an increased membrane tension that subsequently leads to membrane rupture. For this mechanism, all three contributions, membrane shape and elasticity, nanostructure-membrane adhesion, as well as osmotic pressure, are essential to generate the lytic tension based on the minute volume changes by wrapping by wrapping.

In this chapter, we investigate the interaction of spherical particles with vesicles whose shapes are spherical prior to wrapping, see Fig. 4.1. In addition to the ratio of vesicle curvature to particle curvature, we study in particular the role of osmotic pressure and predict wrapping transitions between non-wrapped, partial-wrapped and complete-wrapped states of the particles. The overall shapes of the vesicles with partial-wrapped particles are more sphere-like for higher osmotic pressures, while the "neck" regions around the nanoparticles are more catenoid-like for lower osmotic pressures. We interpret our data in terms of a membrane tension and predict that for the same particle-to-vesicle size ratio and particle-membrane adhesion strength, larger vesicles burst easier. Furthermore, we observe transitions between narrow-neck and wide-neck states for particle entry and large particle-to-vesicle size ratios that have not been reported previously, both with and without osmotic pressure.

In Sec. 4.2, we introduce the model and the numerical calculation technique. In Sec. 4.3, we discuss the total wrapping-energy costs as function of the wrapping fraction for both particle entry and exit. In Sec. 4.3.2, we present both wrapping transitions and wide neck-narrow neck shape transitions. In Sec. 4.3.3 we discuss the energy barriers for the discontinuous transitions, and in Sec. 4.3.4 we discuss the osmotic pressure-induced membrane tension and lysis induced by particle wrapping. We compare our results for both wrapping and shape transitions with the literature and provide an conclusion in Sec. 4.4.

4.2 Model and calculation technique

4.2.1 Membrane deformation and osmotic pressure energies

We calculate the bending energy based on Eq. (3.1), we assume the bilayer and its environment to be symmetric and use $c_0 = 0$. The energy for a particle that interacts with a vesicle,

$$E = 2\kappa \int_A \mathrm{d}S\, H^2 + E_\mathrm{p} + \gamma A - w \int_{A_\mathrm{ad}} \mathrm{d}S\,, \tag{4.1}$$

where w is the adhesion strength that contributes to the energy over the area A_ad where the membrane is adhered to the particle. A rough estimate for complete wrapping to occur is that the adhesion energy gain has to overcome

the bending energy costs. If there are stable partial-wrapped states, higher adhesion strengths are required than those that balance the deformation energy costs to allow the particle to exit a partial-wrapped state. In addition, we take an osmotic pressure term E_p and a term that fixes the total membrane A of the vesicle into account, with the membrane tension γ as Lagrange multiplier.

The osmotic pressure difference between the buffer and the solution within the vesicle is determined by the difference in the osmotic concentrations for two solutions separated by a semi-permeable membrane. Using the van't Hoff law [202], we find the osmotic pressure difference

$$\Delta\Pi = (c_\mathrm{b} - c_\mathrm{v})\, N_\mathrm{A}\, k_\mathrm{B}T\,, \tag{4.2}$$

for the osmolalities c_b and c_v of the solution within and outside the vesicle, respectively; $N_\mathrm{A} = 6.02 \times 10^{23}\,\mathrm{mol}^{-1}$ is the Avogadro constant. We assume an initially spherical vesicle with volume $V_0 = (4/3)\,\pi\, R_\mathrm{v}^3$ and radius R_v, suspended in a buffer with volume $V_\mathrm{b} \gg V_0$. The number of (dissociated) solute molecules within the vesicle and in the buffer are $n_\mathrm{v} = c_\mathrm{v}\, V_0$ and $n_\mathrm{b} = c_\mathrm{b}\, V_\mathrm{b}$, respectively. The solute concentrations in the solutions are chosen to be equal prior to wrapping.

For a particle entering a vesicle, the energy cost due to the volume change is

$$\begin{aligned} E_\mathrm{p}^\mathrm{out2in} &= \int_{V_0}^{V} \mathrm{d}V_\mathrm{v} \left(\frac{n_\mathrm{b}}{V_\mathrm{b}} - \frac{n_\mathrm{v}}{V_\mathrm{v}}\right) N_\mathrm{A}\, k_\mathrm{B}T \\ &= [\tilde{n}_\mathrm{b}(v-1) - \tilde{n}_\mathrm{v}\,\ln(v)]\, k_\mathrm{B}T \\ &= \tilde{n}_\mathrm{v}[v - \ln(v) - 1]\, k_\mathrm{B}T, \end{aligned} \tag{4.3}$$

where $\tilde{n}_\mathrm{b} = n_\mathrm{b}\, N_\mathrm{A}\, V_0\, /V_\mathrm{b}$, $\tilde{n}_\mathrm{v} = n_\mathrm{v}\, N_\mathrm{A}$, and $v = V/V_0$. For the initially spherical vesicle at $E_\mathrm{p}^\mathrm{out2in}(1) = 0$, such that $\tilde{n}_\mathrm{b} = \tilde{n}_\mathrm{v}$.

Similarly, for a particle exiting a vesicle, the energy cost due to the volume change is

$$\begin{aligned} E_\mathrm{p}^\mathrm{in2out} &= \int_{V_0 - V_\mathrm{p}}^{V - V_\mathrm{p}} \mathrm{d}V_\mathrm{v} \left(\frac{n_\mathrm{b}}{V_\mathrm{b}} - \frac{n_\mathrm{v}}{V_\mathrm{v}}\right) N_\mathrm{A}\, k_\mathrm{B}T \\ &= [\tilde{n}_\mathrm{b}^*(v^* - 1) - \tilde{n}_\mathrm{v}\,\ln(v^*)]\, k_\mathrm{B}T \\ &= \tilde{n}_\mathrm{v}[v^* - \ln(v^*) - 1]\, k_\mathrm{B}T, \end{aligned} \tag{4.4}$$

where V_p is the particle volume, $\tilde{n}_\mathrm{b}^* = n_\mathrm{b}\, N_\mathrm{A}\, (V_0 - V_\mathrm{p})\, /V_\mathrm{b}$ and $v^* = (V - V_\mathrm{p})/(V_0 - V_\mathrm{p})$. For the initial spherical vesicle $E_\mathrm{p}^\mathrm{in2out}(1) = 0$, such that $\tilde{n}_\mathrm{b}^* = \tilde{n}_\mathrm{v}$.

In the following, we use the reduced energy $\tilde{E} = E/(8\pi\kappa)$, the reduced adhesion strength $\tilde{w} = wR_\mathrm{p}^2/(2\kappa)$, and the particle-to-vesicle size ratio $\tilde{R}_\mathrm{p} = R_\mathrm{p}/R_\mathrm{v}$. Experimental values reported in the literature span a broad range $0 < \tilde{n}_v < 10^{13}$ [196, 197, 203]. Normal saline with 9 g of salt per litre and

an osmolality of 308 mOsm/l is almost isotonic. Therefore, under these almost physiological conditions $\tilde{n}_v \approx 10^4$ for a small vesicle with $R_\mathrm{v} = 50\,\mathrm{nm}$, $\tilde{n}_v \approx 10^7$ for a vesicle with $R_\mathrm{v} = 500\,\mathrm{nm}$, and $\tilde{n}_v \approx 10^{10}$ for a vesicle with $R_\mathrm{v} = 5\,\mu\mathrm{m}$. For our calculations, we use values in the range $16 < \tilde{n}_\mathrm{v} < 1.6 \times 10^8$.

4.2.2 Triangulated membranes

Using triangulated membranes [12, 123, 145], we calculate vesicle deformation energy contributions due to membrane deformation and volume change for several wrapping fractions $A_\mathrm{ad}/A_\mathrm{p}$. The optimal vesicle shape and the minimal energy for fixed membrane area are obtained with the help of the freely available software package "Surface Evolver" [182].

4.2.3 Energy contributions for wrapping at low and high osmotic pressures

Figure 4.2 shows reduced bending energies, compression energies, and total energies as function of the wrapping fraction for $\tilde{R}_\mathrm{p} = 0.3$, and $\tilde{n}_\mathrm{v} = 16$ and 1.6×10^4. Furthermore, we plot the change of the reduced volume of the vesicles during wrapping.

For out-to-in wrapping, the total energy increases monotonically with increasing wrapping fraction, see Fig. 4.2(a). For $\tilde{n}_\mathrm{v} = 16$ it is dominated by the bending energy, the compression energy contribution is negligible for all wrapping fractions. Upon out-to-in wrapping, the reduced volume v first decreases from 1 to 0.82 if the wrapping fraction increases from $A_\mathrm{ad}/A_\mathrm{p} = 0$ to 0.7, and subsequently increases to 0.84 until complete wrapping. The minimal total energy prior to wrapping is $\tilde{E} = 1$, the deformation energy for forming a spherical vesicle from an initially planar membrane. Once the particle gets wrapped by the vesicle and deforms it, its volume decreases. The osmolality of the interior solution increases with decreasing vesicle volume, because due to the barrier function of the lipid-bilayer membrane the amount of enclosed solute remains constant. This increases the osmotic pressure difference between the interior and the exterior, such that compression energy costs occur upon further compression. For such a low osmotic pressure the dominance of the bending energy leads to a catenoid-like deformation in the vicinity of the particle, see Fig. 4.1(a).

For in-to-out wrapping the bending energy costs are lower compared with out-to-in wrapping for all wrapping fractions $0 < A_\mathrm{ad}/A < 1$, because the catenoidal deformation in the vicinity of the particle extends over a larger membrane area, see Figs. 4.2(b) and 4.1(b). Also the change of the reduced volume during wrapping in the range between $0.88 \lesssim v^* \leq 1$ is smaller than for out-to-in wrapping.

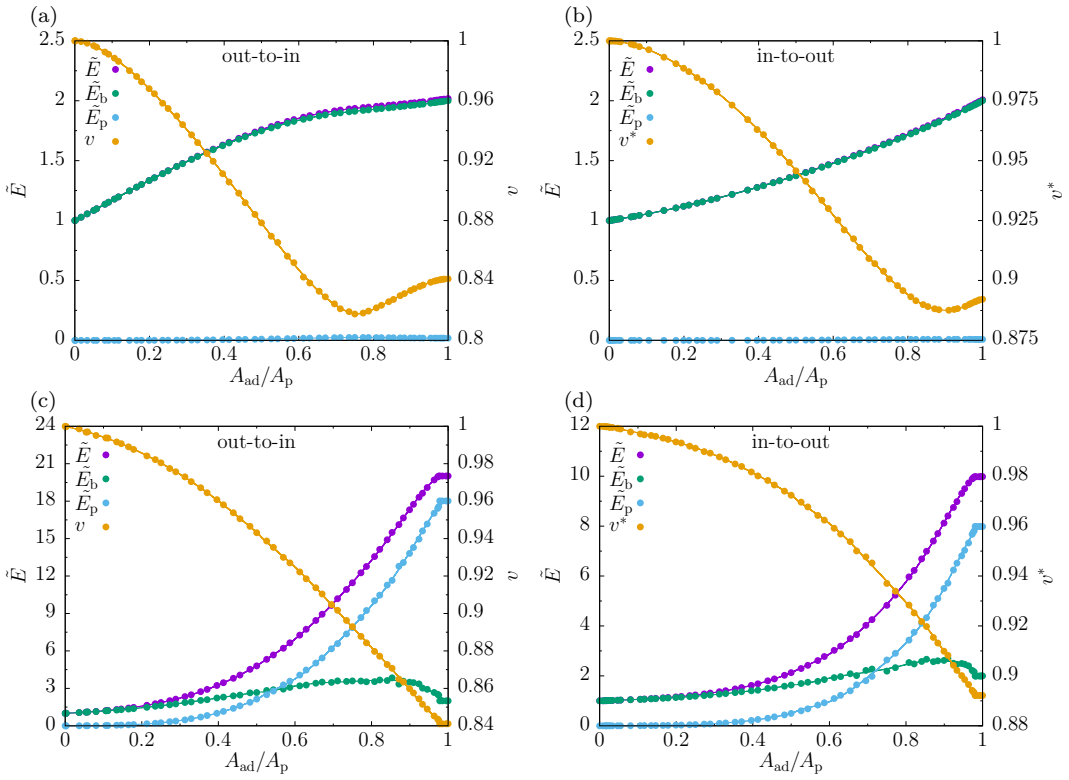

Figure 4.2: Reduced wrapping energies $\tilde{E}$ and reduced vesicle volumes v for particles attached to vesicles as function of the wrapping fraction A_{ad}/A_p for out-to-in and in-to-out wrapping. The reduced particle size is $\tilde{R}_p = 0.3$, and the reduced osmotic constants are (a, b) $\tilde{n}_v = 16$ and (c, d) $\tilde{n}_v = 1.6 \times 10^4$. $\tilde{E}$ is the reduced total energy, $\tilde{E}_b$ is the reduced bending energy, and $\tilde{E}_p$ is the reduced pressure energy. The reduced volume $v = V/V_0$ and $v^* = (V - V_p)/(V_0 - V_p)$, where V_0 and V_p are volume for spherical vesicles and particles with initial radii R_v and R_p, respectively. The numerically calculated data are represented by solid points and the corresponding fit functions are solid lines.

For higher solute concentrations or larger vesicles, $\tilde{n}_v = 1.6 \times 10^4$, both bending energy and compression energy increase weakly for small wrapping fractions, see Figs. 4.2(c) and (d). However, the compression energy significantly exceeds the bending energy for wrapping fractions $A_{ad}/A_p \gtrsim 0.55$ and for $A_{ad}/A_p \gtrsim 0.71$ for out-to-in and in-to-out wrapping, respectively. In both cases, total energy and compression energy increase monotonically with increasing wrapping fraction A_{ad}/A_p. The bending energy increases upon further wrapping for $A_{ad}/A_p \lesssim 0.9$, and decreases for $A_{ad}/A_p \gtrsim 0.9$. The reduced volume decreases monotonically upon wrapping for $A_{ad}/A_p \lesssim 0.98$. For higher wrapping fractions up to complete wrapping, the reduced volume and all energy contributions remain almost constant for wrapping fractions $A_{ad}/A_p \gtrsim 0.98$. The vesicle shapes are more spherical and the membrane deforms strongly within a small area around the particles, see Fig. 4.1; the

membrane deformation in the immediate vicinity becomes even stronger and restricted to an even smaller area in the vicinity of the particle upon further increase of the osmolalities.

4.2.4 Wrapping transitions

The reduced deformation energies $\tilde{E}(A_{\mathrm{ad}}/A_{\mathrm{p}})$ are fit using piecewise functions; the different pieces correspond to different wrapping-fraction regions. In each region, the fit functions are sixth-order polynomials,

$$f\left(\frac{A_{\mathrm{ad}}}{A_{\mathrm{p}}}\right) = \sum_{i=0}^{6} a_i \left(\frac{A_{\mathrm{ad}}}{A_{\mathrm{p}}}\right)^i , \tag{4.5}$$

with the fit parameters a_0, a_1, ..., a_6 and the wrapping fraction $f_{\mathrm{w}} = A_{\mathrm{ad}}/A_{\mathrm{p}}$. For homogeneous adhesion strengths, the total reduced energy at finite reduced adhesion strength $\tilde{w}$ is

$$\tilde{E} = f\left(\frac{A_{\mathrm{ad}}}{A_{\mathrm{p}}}\right) - \tilde{w}\frac{A_{\mathrm{ad}}}{A_{\mathrm{p}}} . \tag{4.6}$$

The wrapping states are determined analogously to the literature [15, 16, 140, 147]. The analysis of extrema and saddle points of the fit functions for various adhesion strengths gives stable states, energy barriers, wrapping transitions, and spinodals.

For all systems that we studied, the sum of deformation and compression energy initially increases with increasing wrapping fraction. Above a threshold value for the wrapping fraction, the sum of both energies stays approximately constant. Therefore, a globally stable non-wrapped state exists for small adhesion strengths. For out-to-in wrapping and small osmolarity, $\tilde{n}_{\mathrm{v}} = 16$, a combined binding-envelopment transition between the non-wrapped and the complete-wrapped state occurs at reduced adhesion strength $\tilde{w}_1$, see Fig. 4.3(a). For $\tilde{w} < \tilde{w}_1$ the non-wrapped state (NW) is stable, for $\tilde{w} > \tilde{w}_1$ the complete-wrapped state (CW) is stable. For in-to-out wrapping, the binding and the envelopment transition occur separately and stable partial-wrapped states (PW) are found for $\tilde{w}_1 < \tilde{w} < \tilde{w}_2$, see Fig. 4.3(b). For $\tilde{w} < \tilde{w}_1$ the non-wrapped state is stable, for $\tilde{w} > \tilde{w}_2$ the complete-wrapped state is stable. For high osmolalities, $\tilde{n}_{\mathrm{v}} = 1.6 \times 10^4$, where compression energy contribution is significant, stable partial-wrapped states are found for both, out-to-in wrapping and in-to-out wrapping, see Figs. 4.3(c) and (d). Furthermore, for high osmolalities the envelopment transition is discontinuous.

Special points for the energy as function of the wrapping fraction are indicated for several wrapping strengths in Fig. 4.3. For the combined binding-envelopment transition W_1 at adhesion strength w_1, where the complete-wrapped

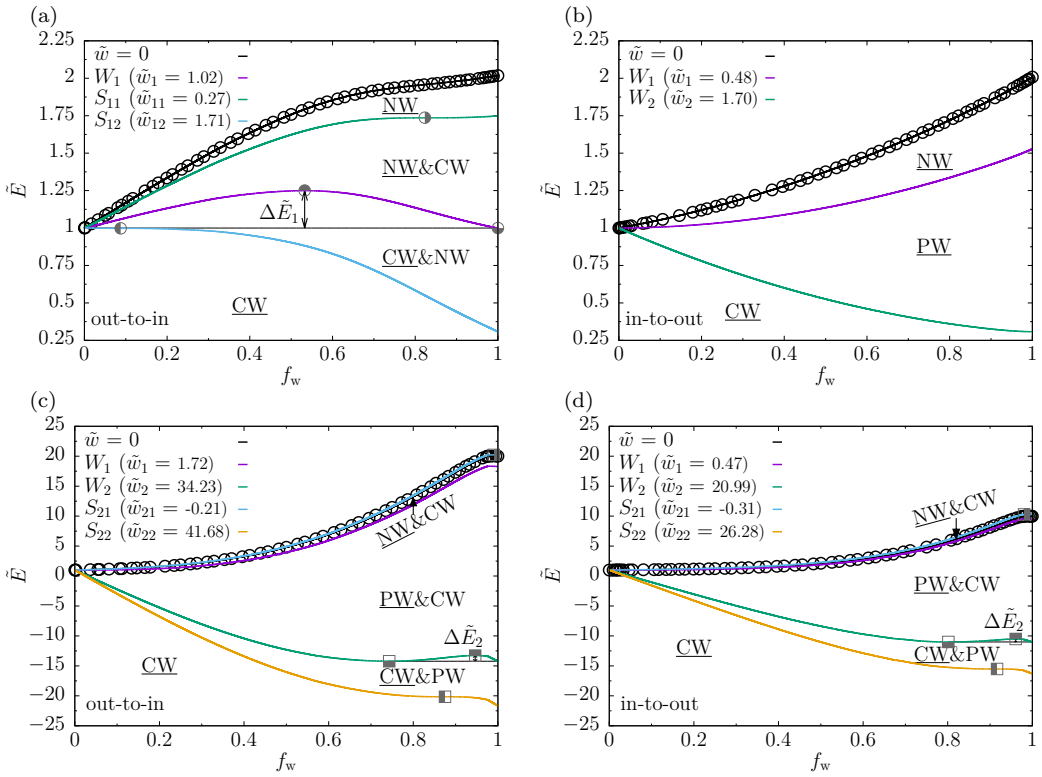

Figure 4.3: Reduced wrapping energies $\tilde{E}$ as function of the wrapping fraction f_w for different reduced adhesion strengths $\tilde{w}$ for out-to-in and in-to-out wrapping. The reduced particle size is $\tilde{R}_p = 0.3$, and the reduced osmotic constants are (a, b) $\tilde{n}_v = 16$ and (c, d) $\tilde{n}_v = 1.6 \times 10^4$. The open circles are numerical results for spherical vesicles wrapping particles. The black lines are fit functions. NW, PW and CW with or without underlines are stable or metastable non-wrapped, partial-wrapped and complete-wrapped states. W_1 is the binding-envelopment transition between NW and CW states (a) or binding transition between NW and PW states (b)-(d), and W_2 is the envelopment transition between PW and CW states; S_{11} and S_{12}, S_{21} and S_{22} are spinodals associated with W_1 and W_2. $\Delta\tilde{E}_1$ and $\Delta\tilde{E}_2$ are energy barriers between NW and CW for W_1, PW and CW for W_2, respectively. For the transition W_1 / W_2, the non-wrapped / partial-wrapped state that corresponds with the complete-wrapped state is indicated by p_1 (◒) / p_5 (⬓) and the energy barrier by p_2 (◓) / p_6 (⬒). The energy barrier vanishes at p_3 (◐) / p_7 (◧) for spontaneous wrapping, and at p_4 (◑) / p_8 (◨) for spontaneous unwrapping.

state at $p_1 = 1$ has the same energy as the non-wrapped state, the energy barrier $\Delta\tilde{E}_1$ is measured at p_2. The saddle points p_3 for adhesion strength w_{12} and p_4 for adhesion strength w_{11} correspond to the spinodals S_{12} and S_{11} where the energy barrier vanishes, respectively. Analogously, for a transition W_2 at adhesion strength w_2, where a partial-wrapped state has the same energy as the complete-wrapped state is indicated by p_5. The corresponding energy maximum $\Delta\tilde{E}_2$ is found at p_6. The points p_7 for adhesion strength w_{22} and p_8 for adhesion strength w_{21} are the saddle points for the spinodals S_{22} and S_{21}, respectively, for which the energy barrier vanishes.

4.3 Results

4.3.1 Wrapping energies

Wrapping energies have been calculated for fixed particle size and various vesicle sizes, and therefore for various reduced particle sizes $\tilde{R}_\mathrm{p}$. Figure 4.4 show the sum of membrane deformation and compression energy as function of the wrapping fraction.

For $\tilde{n}_v = 16$ and out-to-in wrapping, see Fig. 4.4(a), the sum of the energies is larger than $\tilde{E} = 2$ for a bending-only system, which reflects the compression energy contribution. For $\tilde{R}_\mathrm{p} = 0.4$ and 0.5, we find for complete wrapping $\tilde{E} = 2.07$ and 2.22, respectively. These values are comparable to the energies for the partial-wrapped states with $f_\mathrm{w} > 0.63$ ($\tilde{R}_\mathrm{p} = 0.4$) and $f_\mathrm{w} > 0.53$ ($\tilde{R}_\mathrm{p} = 0.5$). We found a shape transition between the regimes where the energy increases with increasing wrapping fraction and where it remains approximately constant that we find also for bending-only systems at high values of $\tilde{R}_\mathrm{p}$. As shown by the snapshots in Fig. 4.4(a), for $\tilde{R}_\mathrm{p} = 0.4$, the vesicle "neck" around the particle is wider for $f_\mathrm{w} = 0.629$ and narrower for $f_\mathrm{w} = 0.646$. Furthermore, the energy for a fixed wrapping fraction increases with increasing reduced particle size if the vesicles wrap a particle to the same wrapping fraction $f_\mathrm{w} > 0$.

For in-to-out wrapping, see Fig. 4.4(b), finite solute concentrations lead to a qualitatively different dependence for the sum of bending and compression energy on $\tilde{R}_\mathrm{p}$ for low and high wrapping fractions. For low osmolalities, $n_v = 164$, the energy decreases with increasing $\tilde{R}_\mathrm{p}$ for $0 < f_\mathrm{w} < 0.88$, but increases with increasing $\tilde{R}_\mathrm{p}$ for $f_\mathrm{w} > 0.98$. It is important to note that all lines do not intersect in the same point; for example, the lines with $\tilde{R}_\mathrm{p} = 0.2$ and 0.25 cross at $f_\mathrm{w} = 0.98$, while the lines with $\tilde{R}_\mathrm{p} = 0.4$ and 0.5 cross at $f_\mathrm{w} = 0.88$. This implies that at finite solute concentrations also for in-to-out wrapping the energy increase with increasing particle size at high wrapping fractions is higher.

For high osmolalities, $\tilde{n}_\mathrm{v} = 1.6 \times 10^4$, the total energies increase strongly with increasing wrapping fraction for both out-to-in and in-to-out wrapping. For $\tilde{R}_\mathrm{p} = 0.4$ and 0.5, adhesion strengths $\tilde{w} > 100$ would be required to completely wrap a particle outside the vesicle, see Fig. 4.4(c). For $\tilde{w} = 100$ the wrapping fractions with lowest energies are $f_\mathrm{w} = 0.67$ and 0.39 for $\tilde{R}_\mathrm{p} = 0.4$ and 0.5, respectively. Therefore, in experiments we expect the particle to stick to a partial-wrapped state. For in-to-out wrapping, see Fig. 4.4(d), the crossing points between the wrapping energies for different $\tilde{R}_\mathrm{p}$ are shifted to smaller wrapping fractions. Although all lines do not cross in a single point, all intersections are found within a narrow range of 'small' wrapping fractions, $0.21 \lesssim f_\mathrm{w} \lesssim 0.27$.

As for low osmolalities, we find a stable partial-wrapped state–with wrapping fraction $f_\mathrm{w} = 0.79$–for $\tilde{R}_\mathrm{p} = 0.5$ and $\tilde{w} = 100$. All systems with smaller

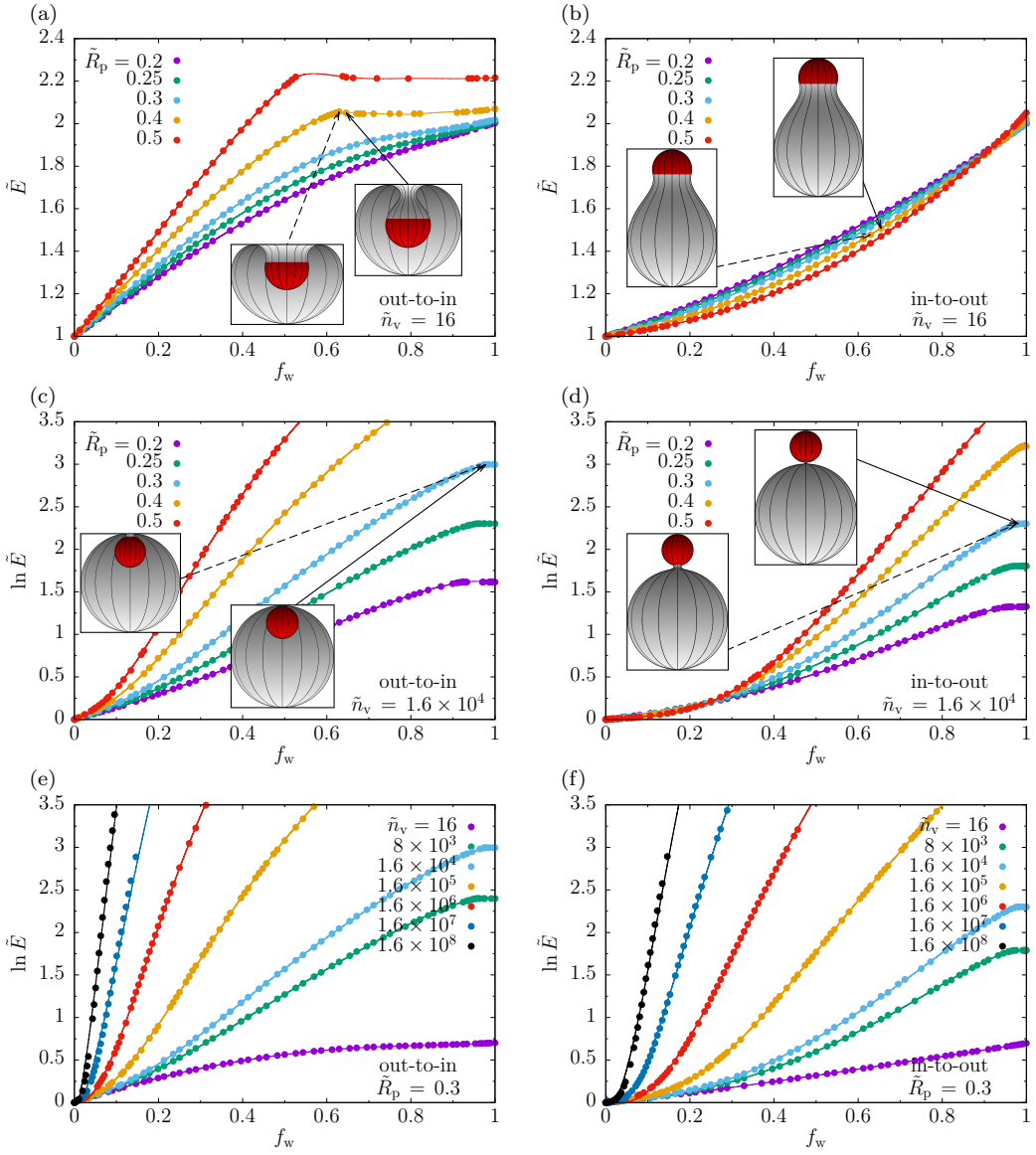

Figure 4.4: Reduced wrapping energies $\tilde{E}$ as a function of the wrapping fraction f_w for (a, b) reduced osmotic constant $\tilde{n}_v = 16$, and (c, d) $\tilde{n}_v = 1.6 \times 10^4$, and different reduced particle sizes $\tilde{R}_p$, and (e, f) reduced particle size $\tilde{R}_p = 0.3$ and different reduced osmotic constants $\tilde{n}_v$. Parameters are same as that in Fig. 4.2. The snapshots for the shape transitions between open and narrow "necks" around the particles are shown. The wrapping fractions f_w from left to right for (a) are 0.629 and 0.646, for (b) 0.629 and 0.655, for (c) 0.976 and 0.978, and for (d) 0.976 and 0.981.

$\tilde{R}_p$ that we simulated are complete wrapped for $\tilde{w} = 100$. Furthermore, we find a regime where the vesicle deformation energy is almost independent of the wrapping fraction, but also for smaller particle-to-vesicle size rations. Also in these cases a shape transition between the wide and narrow "necks" are

found, e.g. for wrapping fractions $f_{\mathrm{w}} \approx 0.97$ for $\tilde{R}_{\mathrm{p}} = 0.3$, see Fig. 4.4(c). Similarly, for $\tilde{R}_{\mathrm{p}} = 0.3$ the vesicle neck is "wide" for $f_{\mathrm{w}} = 0.976$, and "narrow" for $f_{\mathrm{w}} = 0.981$.

A systematic comparison of the vesicle deformation energies as function of the wrapping fraction for $\tilde{R}_{\mathrm{p}} = 0.3$ is shown in Fig. 4.4(e) and (f). The total energies increase with increasing osmolality. For $n_v \gtrsim 1.6 \times 10^5$, we find that a nanoparticle cannot be completely wrapped for $\tilde{w} = 100$. The particles remain attached to the vesicle in a partial-wrapped state with–for out-to-in wrapping–$f_{\mathrm{w}} = 0.45$, 0.19, 0.09 and 0.04 for $\tilde{n}_{\mathrm{v}} = 1.6 \times 10^5, 1.6 \times 10^6, 1.6 \times 10^7$ and 1.6×10^8, respectively. For in-to-out wrapping, where the deformation energies are smaller than that for out-to-in wrapping, we find higher wrapping fractions for the same adhesion strength: $f_{\mathrm{w}} = 0.71$, 0.36, 0.18 and 0.09.

4.3.2 Wrapping and shape transitions

Particle wrapping is best characterized by wrapping diagrams based on calculations for various adhesion strengths and osmolalities. Figure 4.5 shows the wrapping transitions W_1 and W_2 between non-wrapped, partial-wrapped, and complete-wrapped states. For out-to-in wrapping, we find for low solute concentrations a direct binding-envelopment transition from the non-wrapped state to the complete-wrapped state, and for high solute concentrations a continuous binding transition and a separate, discontinuous envelopment transition. For in-to-out wrapping, binding transition and envelopment transition are separate for all osmolalities. The binding transition is always continuous. The envelopment transition is continuous and essentially independent on the adhesion strength for small osmolalities, and it becomes discontinuous and strongly dependent on the adhesion strength for high osmolalities.

We study wrapping for various values of $\tilde{R}_{\mathrm{p}}$ and find that the wrapping diagrams differ only quantitatively. However, the shifts of the transitions in the phase diagram for different are qualitatively different for out-to-in and in-to-out wrapping. For out-to-in wrapping both the binding transition and the envelopment transition shift to higher adhesion strengths for increasing $\tilde{R}_{\mathrm{p}}$. For in-to-out wrapping, particle binding occurs at lower adhesion strengths for larger $\tilde{R}_{\mathrm{p}}$, while the envelopment transition is shifted to higher adhesion strengths. This increase of the regime with partial-wrapped states, which has already been been reported in the literature for the bending-only case, is even larger for the regime where the envelopment transition is discontinuous at high osmolalities than for the regime where it is continuous at low osmolalities.

The continuous transitions and the combined binding-envelopment transition can be predicted analytically, see appendix B. We can therefore also analytically predict the minimal osmolality for that a partial-wrapped state occurs for out-to-in wrapping, which is the intersection point of the direct

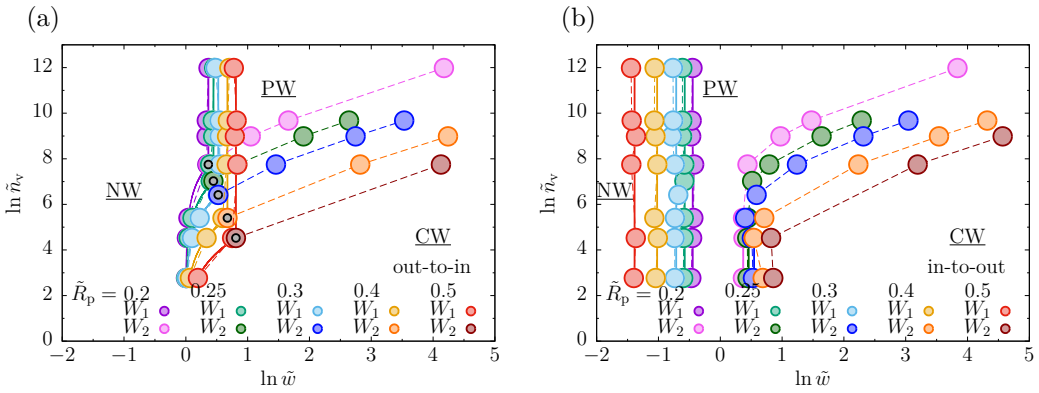

Figure 4.5: Wrapping states for spherical particles with reduced adhesion strengths $\tilde{w}$, and different reduced osmotic constants $\tilde{n}_v$ and reduced particle sizes $\tilde{R}_p$ for (a) out-to-in and (b) in-to-out wrapping. Stable non-wrapped states (NW), partial-wrapped states (PW) and complete-wrapped states (CW) are found. W_1 is the binding-envelopment transition separating the stable NW and CW states, or the binding transition separating the stable NW and PW states, W_2 is the envelopment transition separating the stable PW and CW states. The solid straight lines are the analytical data given by the Eq. (B1) for (a) out-to-in wrapping,and Eqs. (B2) and (B3) for (b) in-to-out wrapping in the Appendix cited from Ref. [13]. The solid curved lines are the analytical data given by Eq. (B5) in the appendix. The dashed lines are the numerical data from our calculations. For (a) out-to-in wrapping, the solid and dashed lines meet at black points that separate the binding-envelopment, binding and envelopment transitions.

binding-envelopment transition and the continuous binding transition. For out-to-in wrapping, the combined binding-envelopment transition W_1 occurs for $\tilde{w} = \tilde{n}_v\,(v - \ln v - 1)/(8\pi\kappa) + 1$, and the continuous binding transition occurs for $\tilde{w} = (1 + R_p/R_v)^2$ [13, 14]. For in-to-out wrapping, the continuous binding transition occurs for smaller adhesion strengths compared with out-to-in wrapping at $\tilde{w} = (1 - R_p/R_v)^2$ [13, 14]. The continuous envelopment transition at low solvent concentrations occurs at $\tilde{w} = (1 + R_p/(R_v(1 - R_p^2/R_v^2)^{1/2}))^2$. Our numerical calculations show excellent agreement with these analytical predictions.

In Fig. 4.6, the wrapping fractions f_w for the intersections between the deformation energy for wide necks at small wrapping fractions and the deformation energy for narrow necks at large wrapping fractions are plotted as function of the osmolalities. The threshold wrapping fractions for low osmolality systems–that also occur without solute–are disconnected from the threshold wrapping fractions for high osmolalities, see also Figs. 4.4(a), (c) and (d). Whereas the former occur for wrapping fractions $0.5 \lesssim f_w \lesssim 0.7$, the latter are mostly found for wrapping fractions $f_w > 0.8$. Furthermore, the values of f_w shift to higher wrapping fractions for higher osmolalities and for larger $\tilde{R}_p$. All shape changes are accompanied by discontinuous wrapping transitions.

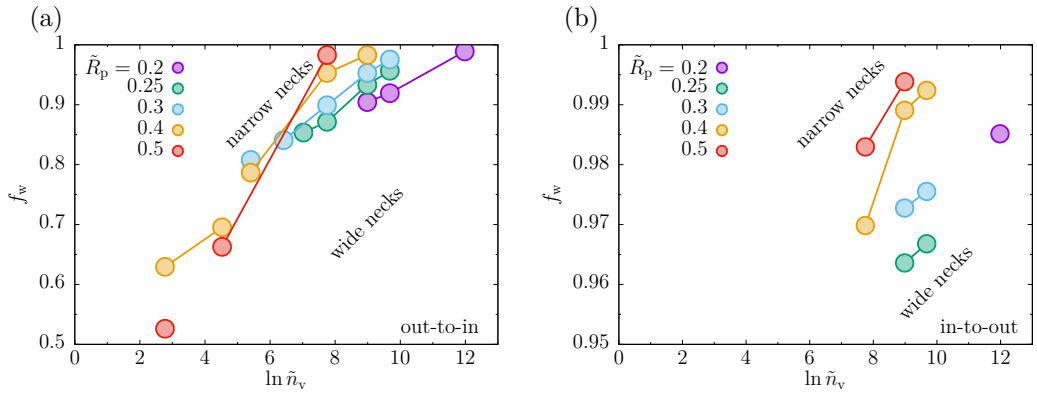

Figure 4.6: Wrapping fractions f_w as a function of the osmotic constant $\tilde{n}_v$ for different reduced particle sizes $\tilde{R}_p$ for (a) out-to-in and (b) in-to-out wrapping. The shape transitions between wide and narrow necks for the binding-envelopment transition W_1 are disconnected from those for the envelopment transitions W_2 for reduced particle sizes $\tilde{R}_p = 0.3$, 0.4 and 0.5 in (a); the critical osmotic constants separating W_1 and W_2 indicated by the black points in Fig 4.5(a). Wide necks occur at footnotesize wrapping fractions while narrow necks occur at large wrapping fractions; examples for wide and narrow necks are shown in Figs. 4.4(a), (c) and (d).

4.3.3 Energy barriers

Figure 4.7 shows the energy barriers for the discontinuous wrapping transitions. The energy barriers monotonically increase with increasing osmolality. For out-to-in wrapping, the values of the energy barriers $\Delta\tilde{E}_1$ for the combined binding-envelopment transition smoothly connect to those for the energy barriers $\Delta\tilde{E}_2$ for the envelopment transition at higher osmolalities when the binding transition becomes continuous. Whereas the dependence of the height of the energy barrier on the osmolality is weak for the binding-envelopment transition, it strongly increases with increasing osmolality for the envelopment transition. Both energy barriers, $\Delta\tilde{E}_1$ and $\Delta\tilde{E}_2$, increase with increasing reduced particle size $\tilde{R}_p$. This implies that for particles of given size, the required activation energies to overcome the energy barriers are higher the smaller the vesicle is. An analogous dependence of the energy barrier on osmolality and particle size is found for the envelopment transitions for in-to-out wrapping, see Fig. 4.5(b). However, the energy barriers for in-to-out wrapping are generally smaller than for out-to-in wrapping. Furthermore, the envelopment transition for in-to-out wrapping is continuous for small osmolalities and for small $\tilde{R}_p$, e.g. for $\tilde{R}_p = 0.2$ for $\tilde{n}_v < 2324.56$ ($\ln \tilde{n}_v < 7.75$).

The wrapping fractions of specific points that are related to the wrapping transitions are plotted in Fig. 4.8: the partial-wrapped state to that the system transitions from the non-wrapped state or the complete-wrapped state, the maximal height of the energy barriers, and the points where the energy vanishes. These points are marked in $\tilde{E}(f_w)$ plots in Fig. 4.3 for four exemplary

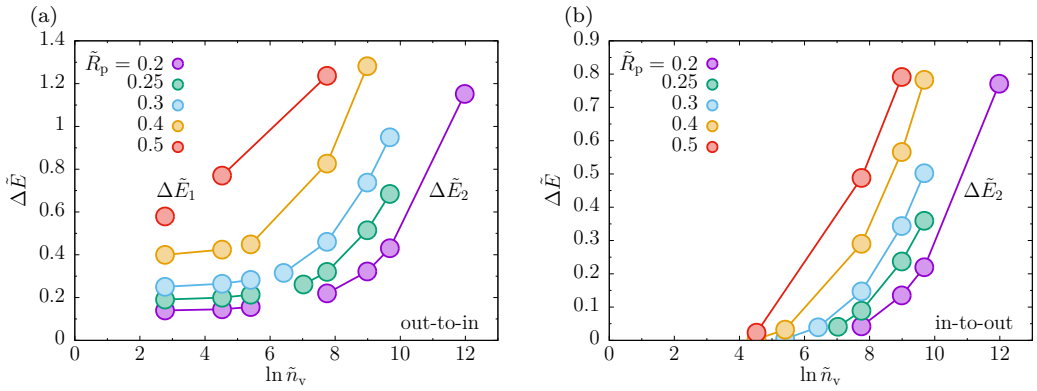

Figure 4.7: Energy barriers $\Delta\tilde{E}$ as function of the reduced osmotic constant $\tilde{n}_v$ for different reduced particle sizes $\tilde{R}_p$ for (a) out-to-in and (b) in-to-out wrapping. $\Delta\tilde{E}_1$ is the barrier for the binding-envelopment transition W_1 between the non-wrapped and the complete-wrapped state, $\Delta\tilde{E}_2$ is the barrier for the envelopment transition W_2 between the partial-wrapped and the complete-wrapped state. The solid lines connect the numerical data from our calculations.

systems.

Figure 4.8(a) shows that for out-to-in wrapping, the wrapping fractions for the energy maxima, for the spinodals, and for the partial-wrapped state that has the same energy as the complete-wrapped state increase with increasing osmolality. The wrapping fraction for the partial-wrapped state for the W_2 transition increases monotonically from $f_w = 0$ to high wrapping fractions. For in-to-out-wrapping, see Fig. 4.8(b), we find the partial-wrapped state for W_2 only for wrapping fractions $f_w > 0.6$.

For fixed osmolality, $\tilde{n} = 8 \times 10^3$, all specific points that are connected with the envelopment transition W_2 increase with increasing $\tilde{R}_p$, see Figs. 4.8(c)-(d). All specific points connected with the binding transition W_1, however, are almost independent of $\tilde{R}_p$.

4.3.4 Membrane tension and vesicle lysis

With the help of the Laplace pressure,

$$\Delta\Pi = \Pi_v - \Pi_b = 2\gamma H \tag{4.7}$$

the osmotic pressure difference between interior and exterior of a vesicle is connected with the membrane tension γ. Assuming that the area of the vesicle does not change upon wrapping, the reduced osmotic pressure for out-to-in

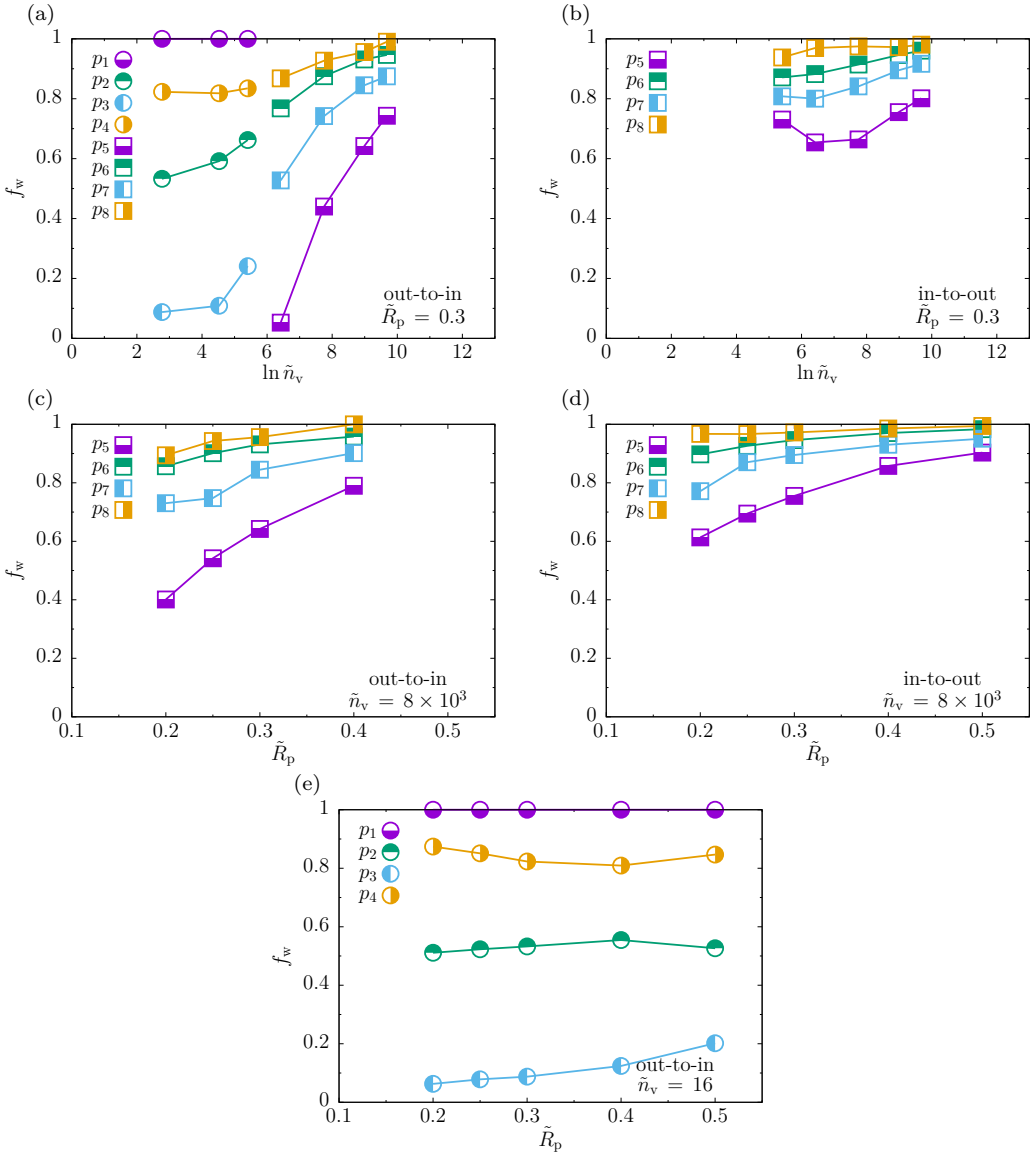

Figure 4.8: Wrapping fractions f_w for special points $p_1 - p_8$ labeled on the wrapping-energy functions in Fig. 4.3 for (a, b) reduced particle size $\tilde{R}_p = 0.3$ and different osmotic constants $\tilde{n}_v$, and (c, d) reduced osmotic constant $\tilde{n}_v = 8 \times 10^3$ and (e) $\tilde{n}_v = 16$, and different reduced particle sizes $\tilde{R}_p$. At adhesion strength w_1, the complete-wrapped state is found at wrapping faction p_1 and the energy maximum at wrapping faction p_2 for the binding-envelopment transition W_1, the energy barrier between the non-wrapped and the complete-wrapped states vanishes at wrapping factions p_3 and p_4 for spinodals S_{12} and S_{11}, respectively. At adhesion strength w_2, the partial-wrapped state is found at p_5 and the energy maximum at p_6 for the envelopment transition W_2, the energy barrier between the partial-wrapped and the complete-wrapped states vanishes at p_7 and p_8 for spinodals S_{22} and S_{21}, respectively.

wrapping is

$$\begin{aligned}\Delta\tilde{\Pi} &= \frac{\Delta\Pi\, R_{\mathrm{v}}^3}{k_{\mathrm{B}}T} \\ &= \left(\frac{n_{\mathrm{v}}}{V_{\mathrm{v}}} - \frac{n_{\mathrm{b}}}{V_{\mathrm{b}}}\right) N_{\mathrm{A}}\, R_{\mathrm{v}}^3 \\ &= \frac{3}{4\pi}\left(\frac{1}{v} - 1\right)\tilde{n}_{\mathrm{v}}\,.\end{aligned} \tag{4.8}$$

Therefore, we find for the reduced, pressure-induced tension

$$\tilde{\gamma} \;=\; \frac{\gamma R_{\mathrm{v}}^2}{k_B T} = \frac{\Delta\Pi R_{\mathrm{v}}^3}{2\, k_{\mathrm{B}}T} = \frac{1}{2}\Delta\tilde{\Pi}\,, \tag{4.9}$$

here, we suppose the radius of vesicle during wrapping is same as the initial radius of spherical vesicle R_{v}. Analogously, for in-to-out wrapping

$$\begin{aligned}\Delta\tilde{\Pi}^* &= \frac{\Delta\Pi\, \left(R_{\mathrm{v}}^3 - R_{\mathrm{p}}^3\right)}{k_{\mathrm{B}}T} \\ &= \left(\frac{n_{\mathrm{v}}}{V_{\mathrm{v}} - V_{\mathrm{p}}} - \frac{n_{\mathrm{b}}}{V_{\mathrm{b}}}\right) N_{\mathrm{A}}\, \left(R_{\mathrm{v}}^3 - R_{\mathrm{p}}^3\right) \\ &= \frac{3}{4\pi}\left(\frac{1}{v^*} - 1\right)\tilde{n}_{\mathrm{v}}\,,\end{aligned} \tag{4.10}$$

and

$$\tilde{\gamma}^* \;=\; \frac{\gamma\, \left(R_{\mathrm{v}}^3 - R_{\mathrm{p}}^3\right)}{R_{\mathrm{v}}\, k_B T} = \frac{\Delta\Pi\, \left(R_{\mathrm{v}}^3 - R_{\mathrm{p}}^3\right)}{2\, k_{\mathrm{B}}T} = \frac{1}{2}\Delta\tilde{\Pi}^*\,. \tag{4.11}$$

For the constant osmotic pressure difference $\tilde{n}_{\mathrm{v}}$, the vesicle raptures if the maximal membrane tension γ is larger than the lytic tension γ_ℓ: $\gamma \gtrsim \gamma_\ell$, from which and Eq. (4.9), we can define a vesicle radius $R_{\mathrm{v}}|_{\tilde{n}_{\mathrm{v}}}$ associated with lysis for out-to-in wrapping as

$$\begin{aligned}R_{\mathrm{v}} &\lesssim \sqrt{\frac{\tilde{\gamma} k_{\mathrm{B}}T}{\gamma_\ell}}\,, \\ &\lesssim \sqrt{\frac{3\,(1-v)\;\tilde{n}_{\mathrm{v}}\, k_{\mathrm{B}}T}{8\pi v\, \gamma_\ell}} := R_{\mathrm{v}}|_{\tilde{n}_{\mathrm{v}}}\,.\end{aligned} \tag{4.12}$$

Similarly, for in-to-out wrapping, according to $\gamma \gtrsim \gamma_\ell$ and Eq. (4.11), the vesicle radius $R_{\mathrm{v}}^*|_{\tilde{n}_{\mathrm{v}}}$ for lysis is

$$\begin{aligned}R_{\mathrm{v}} &\lesssim \sqrt{\frac{\tilde{\gamma}^* k_{\mathrm{B}}T}{\left(1 - \tilde{R}_p^3\right)\gamma_\ell}}\,, \\ &\lesssim \sqrt{\frac{3\,(1-v^*)\;\tilde{n}_{\mathrm{v}}\, k_{\mathrm{B}}T}{8\pi\left(1 - \tilde{R}_{\mathrm{p}}^3\right) v^*\, \gamma_\ell}} := R_{\mathrm{v}}^*|_{\tilde{n}_{\mathrm{v}}}\,.\end{aligned} \tag{4.13}$$

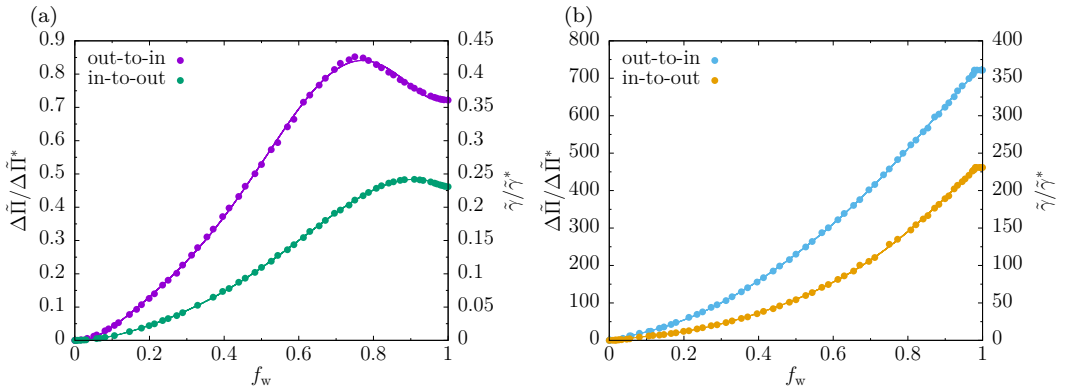

Figure 4.9: Reduced osmotic pressure difference $\Delta\tilde{\Pi}$ and $\Delta\tilde{\Pi}^*$, and membrane tension $\tilde{\gamma}$ and $\tilde{\gamma}^*$ as a function of wrapping fraction f_w for out-to-in and in-to-out wrapping, respectively. The reduced particle size is $\tilde{R}_p = 0.3$, and the reduced osmotic constant is (a) $\tilde{n}_v = 16$, and (b) $\tilde{n}_v = 1.6 \times 10^4$.

We now discuss exemplarily membrane tension and vesicle lysis for a system with $\tilde{R}_p = 0.3$ for both out-to-in and in-to-out wrapping. For constant $\tilde{n}_v = 16$, see Fig. 4.9(a), the maximal membrane tension $\gamma_{max} \approx 0.425$ and $\gamma^*_{max} \approx 0.25$ for out-to-in and in-to-out wrapping, respectively. The membrane lytic tension is $\gamma_\ell = 2.5\, k_B T/\text{nm}^2$ [204], according to Eqs. (4.12) and (4.13), the vesicle radii for lysis are $R_v|_{\tilde{n}_v} = 0.41\,\text{nm}$ and $R^*_v|_{\tilde{n}_v} = 0.32\,\text{nm}$. For constant $\tilde{n}_v = 1.6\times10^4$, see Fig. 4.9(b), the vesicle lyses if $R_v \lesssim 12\,\text{nm}$ and $R_v \lesssim 9.62\,\text{nm}$ for out-to-in and in-to-out wrapping, respectively.

4.4 Conclusions

The first essential step for large nanoparticles to accomplish a beneficial or toxic function in cells is adsorption of the particles to the plasma membrane, which is followed by the wrapping of the particles by the membrane.

We systematically investigated the roles of the reduced particle size $\tilde{R}_p$ and osmotic constants $\tilde{n}_v$ on the wrapping of spherical particles by vesicles. The vesicle shapes prior to wrapping are spheres as there are no osmotic pressure differences. Depending on the initial positions of particles, we studied two distinct wrapping processes, out-to-in and in-to-out wrapping: particles initially located outside or inside the vesicles enter or exit the vesicles, respectively.

The reduced bending and osmotic energy of the membrane is calculated as a function of the wrapping fraction. We found three stable wrapping regimes including non-wrapped, partial-wrapped and complete-wrapped states for different reduced adhesion strengths. If a stable partial-wrapped state is found, the binding transition refers a transition between a stable non-wrapped and partial-wrapped state, while the envelopment transition is a transition between a stable partial-wrapped and complete-wrapped state. There is also a

direct binding-envelopment transition from the non-wrapped to the complete-wrapped state. Whereas a continuous wrapping transition does not need to overcome an energy barrier, a discontinuous transition is characterized by an energy barrier.

Our numerical calculations indicate that for out-to-in wrapping, for lower osmotic constants $\tilde{n}_{\mathrm{v}}$, the binding-envelopment transition between the non-wrapped and the complete-wrapped state is characterized by an energy barrier, which increases with increasing $\tilde{R}_{\mathrm{p}}$ and $\tilde{n}_{\mathrm{v}}$. This means that it is easier for a large particle to attach to the membrane and to reach the complete-wrapped state. For higher osmotic constants $\tilde{n}_{\mathrm{v}}$, a continuous binding transition between the non-wrapped to a stable partial-wrapped state without an energy barrier is found, but the envelopment transition between a stable partial-wrapped state and the complete-wrapped state is discontinuous with an energy barrier, which increases with both increasing $\tilde{R}_{\mathrm{p}}$ and $\tilde{n}_{\mathrm{v}}$.

For in-to-out wrapping, the reduced adhesion strength decreases with increasing $\tilde{R}_{\mathrm{p}}$ for the binding transition, but increases with increasing $\tilde{R}_{\mathrm{p}}$ for the envelopment transition. It demonstrates that the onset of wrapping is easier for a small vesicle, but meanwhile it is more difficult to completely wrap the entire particle. Furthermore, a low $\tilde{n}_{\mathrm{v}}$ helps to lower the adhesion strength for the envelopment transition. Both continuous binding transition and envelopment transition which have no energy barriers are like to occur at vesicles with low $\tilde{n}_{\mathrm{v}}$ and small $\tilde{R}_{\mathrm{p}}$.

To gain better understanding of nanoparticle wrapping by vesicles, the surface tension and the line tension can be taken into account. Furthermore, non-spherical particles such as ellipsoidal, rod-like and cube-like particles are needed to integrate into the next calculations. As the membrane is a fluid and dynamic structure, it is important to consider the deformation energy for a non-symmetric vesicle wrapping a nanoparticle. Our calculation might provide some meaningful predictions of the bending and osmotic energy for such vesicles in nanoparticle uptake.

Chapter 5

Tether-mediated nanoparticle interaction

Membrane tethers are essential for cargo trafficking in endoplasmic reticulum, Golgi apparatus, endosome and plasma membrane. Biological substances, such as proteins, macromolecules and viruses, and engineered materials, such as particles, can adhere to membrane tethers and trigger physiological and pathological processes in living cells. We study membrane-mediated interactions between spherical nanoparticles that are initially located outside or inside tethers. Depending on particle-to-tether radii ratio, particle separation distance, membrane bending rigidity, and membrane tension, both attractive and repulsive interactions between nanoparticles mediated by tether deformations are found for inside particles. Instead of forming compact linear aggregates along the longitudinal axis of tethers, the nanoparticles stay at their lowest-energy positions with finite distances from each other. Energy barriers have to be overcome for outside particles to transition from non-wrapped to complete-wrapped states. Our results suggest that membrane-mediated nanoparticle interactions can alter the wrapping transitions between non-wrapped, partial-wrapped, and complete-wrapped states. Above a threshold distance, the adhesion strengths for these transitions do not strongly depend on the particle separation distances. Deformation of the contact lines where the unbound detach from the particles can be used to characterize the influence of the curved membrane; they can also be a measure for the influence of the neighboring particles on the wrapping. The largest deformations of the contact lines between adhered membrane and free membrane are always found for small particle distances.

5.1 Introduction

Membrane tethers, highly-curved tubular structures, can be extracted from synthetic vesicles (giant uniamellar vesicles) or living cells (e.g. red blood cells

and neuronal growth cones) using micropipettes [205, 206], optical tweezers [207, 208], or fluid drag [209, 210] *in vitro*. Tethers are used to measure elastic properties of membranes like bending rigidity and membrane tension, as well as the adhesion strength between membrane and cytoskeleton [211, 212]. For the networks of endoplasmic reticulum, Golgi apparatus, endosome and plasma membrane *in vivo*, the tethers are formed by the application of a force exerted on a membrane. In vivo, this force can be generated by clusters of attached motor proteins that walk along the microtubules of cytoskeleton [213–215]. Polymerizing forces created by the membrane cytoskeleton alone are also able to draw the tethers out [216, 217]. Many biological processes are involved in formation and deformation of membrane tethers, such as intracellular transport during endocytosis and exocytosis, intercellular trafficking between the organelles, endosome fusion, and neurotransmitter release in synapses [212, 218, 219]. Previous studies show that the radii of tethers are determined by the bending rigidity κ and tension σ of the membrane [211, 220], which gives $R_t = \sqrt{\kappa/(2\sigma)}$. They fall into the range $5 - 50\,\mathrm{nm}$ [221, 222] and remain constant during extraction [223].

The functions of membrane tethers require a panoply of proteins that can efficiently interact with the highly-curved membranes and induce local deformations of the lipid bilayers [224]. An example of these proteins are Bin-Amphiphysin-Rvs (BAR) domain proteins with N-terminal amphipathic helices (N-BAR). A recent study shows that membrane-mediated protein interactions influence the localization of proteins and scaffolds on membrane tubes [225]. Another experiment reveals that the coupling of the amphiphysin (N-BAR protein) with membranes depends on the density of the proteins [226].

Membrane-mediated interactions and aggregations of nanoparticles adhered to tethers are important for the application of nanoparticles in nanotechnology, which, for instance, can facilitate the transport of the drug-loaded nanoparticle delivery systems. Furthermore, nanoparticle-tether interactions play a key role in biological and chemical sensors [227, 228], as catalysts for biochemical reactions [229, 230], as well as potential hybrid materials in living cells [231, 232]. Therefore a good characterization of adsorption, wrapping, and other engulfment processes that enable us to measure the role of geometric and elastic parameters on nanoparticle-tether interactions is required. Among these processes endocytosis and exocytosis for nanoparticle-tether interactions have to be studied [10, 233]: endocytosis is responsible for high targeting efficiency of a designed nanoparticle, while exocytosis is important for removal and clearance of nanoparticles to reduce cellular toxicity [10].

In addition to proteins, also particles and the macromolecules experience membrane-mediated interactions due to local elastic deformations. For planar membranes, cooperative interactions between particles and macromolecules adhering to the membrane drive stable clustering and self-organization in lin-

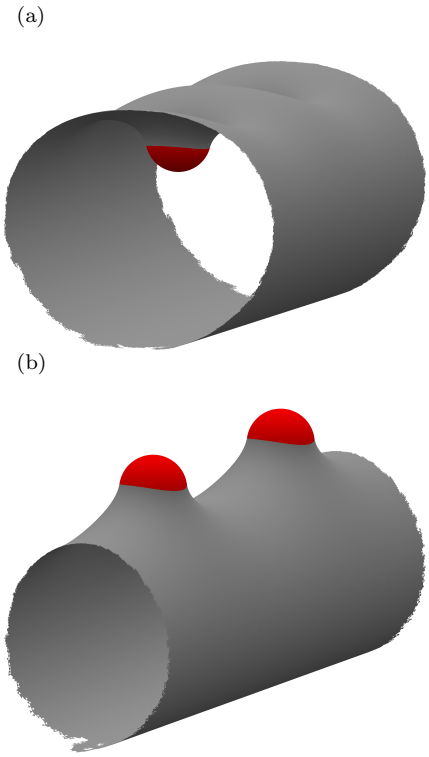

Figure 5.1: Representative shapes of membrane tethers and spherical nanoparticles for (a) out-to-in and (b) in-to-out wrapping. The ratio of the radii of particles and tethers is $R_\mathrm{p}/R_\mathrm{t} = 0.3$, the ratio of the distance of the particle centers and particle radio is $D/R_\mathrm{p} = 7.5$. The adhered membrane A_ad is colored red and the free membrane gray, separated by the contact line. The wrapping fraction is $A_\mathrm{ad}/A_\mathrm{p} = 0.41$, where A_p is the surface area of the particle.

ear or tubular aggregates [234–238]. For curved membranes, multiple spherical particles always attract each other and form ring-like structures along the maximal curvature direction [234, 235, 239]. The interactions between two ring-shaped and rod-shaped inclusions can be attractive or repulsive depending on the separation distances, while many point-like inclusions tend to form linear aggregates [240]. Spherical nanoparticles self assemble into minimal-energy linear configurations adhering to membrane tubes. The transition from the linearly-aggregated state to the state where the particles are completely wrapped by membrane, is easier for increased of tube radius and particle concentration, and for decreased bending rigidity of the membrane [241]. Rings or helical structures are found for spherical nanoparticles attached to the outer tube membrane [242].

The interplay of nanoparticles wrapping and membrane-mediated interactions between particles adhered to membrane tethers is not well understood. In this chapter, we investigate the interactions between spherical particles and membrane tethers with periodic boundary conditions along the longitudinal

axis direction. In addition to the ratio of tether curvature to particle curvature, $c_\mathrm{t}/c_\mathrm{p} = R_\mathrm{p}/R_\mathrm{t}$, we also consider the role of the distance D of the centers of two adjacent particles. Wrapping transitions between non-wrapped, partial-wrapped and complete-wrapped states of the particles are predicted by our calculations. Furthermore, we find both attractive and repulsive interactions for nanoparticle wrapping, depending on particle-to-tether radii ratio, particle separation distance, and adhesion strength. Figure 5.1 displays membrane tether shapes for partial-wrapped particles for $R_\mathrm{p}/R_\mathrm{t} = 0.3$ and $D/R_\mathrm{p} = 7.5$ for out-to-in and in-to-out wrapping.

In Sec. 5.2, we discuss exemplary the bending energy as function of the wrapping fraction for out-to-in and in-to-out wrapping. In Sec. 5.3.1, the adhesion strengths for the wrapping transitions between non-wrapped, partial-wrapped and complete-wrapped states, and shallow-deep transitions with small and large wrapping fractions between two stable partial-wrapped states are presented. The dependence of adhesion strengths on particle-to-tether radii ratio and particle separation distance are discussed. The energy barriers associated with discontinuous wrapping transitions are shown in Sec. 5.3.2. Membrane-mediated nanoparticle interaction as well as the wrapping fractions for stable partial-wrapped states are analyzed in Sec. 5.3.3 for particles initially located inside the tethers. In Sec. 5.3.4, we study the heights of the deformed contact lines for different wrapping fractions. We compare our results for both wrapping transitions and particle interactions with the literature and provide conclusions in Sec. 5.4.

5.2 Model and calculation technique

5.2.1 Energy contributions

For particle wrapping, the bending energy is calculated based on Eq. (3.1), and in particular the membrane tension σ is considered in the deformation energy costs for the symmetric lipid bilayer,

$$E = \int_A \mathrm{d}S \, \left(2\kappa H^2 + \sigma\right) - w \int_{A_\mathrm{ad}} \mathrm{d}S \,. \tag{5.1}$$

To investigate the interactions between nanoparticles, we use different distances D of the centers of two adjacent nanoparticles in periodic boundary conditions. For an infinitely long membrane tether wrapping infinitely many nanoparticles, the distances D between two adjacent particles are fixed. Figure 5.1 shows the snapshots of membrane tethers and particles for $\tilde{R}_\mathrm{p} = 0.3$ and $\tilde{D} = 7.5$ for (a) out-to-in and (b) in-to-out wrapping.

In the following, we use dimensionless parameters $\tilde{E} = E/(8\pi\kappa)$, $\tilde{w} = wR_\mathrm{p}^2/(2\kappa)$, $\tilde{R}_\mathrm{p} = R_\mathrm{p}/R_\mathrm{t}$, and $\tilde{D} = D/R_\mathrm{p}$ for energy, adhesion strength, reduced particle radius, and reduced distance, respectively. We also calculate the wrapping energy for a single particle wrapped by a single vesicle with radius $R_\mathrm{v} = 2R_\mathrm{t}$, the reduced particle size for vesicle-particle system is $\tilde{R}_\mathrm{p} = R_\mathrm{p}/R_\mathrm{v}$; the membrane area A of a vesicle is fixed in our simulations.

The reduced total energies of the membrane relative to the unwrapped state are denoted by $\Delta\tilde{E}(A_\mathrm{ad}/A_\mathrm{p})$, and the reduced deformation energies are fit with sixth order polynomials,

$$f\left(\frac{A_\mathrm{ad}}{A_\mathrm{p}}\right) = \sum_{i=0}^{6} a_i \left(\frac{A_\mathrm{ad}}{A_\mathrm{p}}\right)^i , \tag{5.2}$$

using the fit parameters a_0, a_1, ..., a_6. The total reduced energy at finite reduced adhesion strength $\tilde{w}$ is

$$\Delta\tilde{E} = f\left(\frac{A_\mathrm{ad}}{A_\mathrm{p}}\right) - \tilde{w}\frac{A_\mathrm{ad}}{A_\mathrm{p}} . \tag{5.3}$$

The analysis of extreme and saddle points of the fit functions for various adhesion strengths gives stable states, energy barriers, wrapping transitions, and spinodals. For simplicity, we use the symbol f_w to represent the wrapping fraction $A_\mathrm{ad}/A_\mathrm{p}$.

For both out-to-in wrapping and in-to-out wrapping, the total energies increase with increasing wrapping fraction. For homogeneous adhesion strengths, the adhesion energy is proportional to the wrapping fraction. Wrapping states are determined analogously to the literature [15, 16, 140, 147]. A globally stable non-wrapped state exists for small adhesion strengths. For out-to-in wrapping with reduced particle size $\tilde{R}_p = 0.1$ and reduced distance $\tilde{D} = 2.5$, see Fig. 5.2(a), binding-envelopment transitions W_1 between non-wrapped and complete-wrapped states occur at reduced adhesion strength $\tilde{w}_1$, for which the total energy of the non-wrapped state is equal to that of the complete-wrapped state. For $\tilde{w} < \tilde{w}_1$ the non-wrapped state (NW) is stable, for $\tilde{w} > \tilde{w}_1$ the complete-wrapped state (CW) is stable. For in-to-out wrapping with same reduced particle size and distance, see Fig. 5.2(b), a stable partial-wrapped state (PW) is found for $\tilde{w}_1 < \tilde{w} < \tilde{w}_2$. For $\tilde{w} < \tilde{w}_1$ the non-wrapped state is stable, for $\tilde{w} > \tilde{w}_2$ the complete-wrapped state is stable. For $\tilde{w} = \tilde{w}_1$, binding transitions W_1 exist where the total energies of the non-wrapped and a partial-wrapped states are equal; for $\tilde{w} = \tilde{w}_2$ envelopment transitions W_2 are found for which the total energies of the complete-wrapped and a partial-wrapped states are equal. For $\tilde{w}_1 < \tilde{w} < \tilde{w}_2$, shallow-deep transitions W_3 between two stable partial-wrapped states are found.

As shown in Fig. 5.2, for adhesion strength w_1, where the complete-wrapped (see Fig. 5.2(a)) or a partial-wrapped state (see Fig. 5.2(b)) at wrapping frac-

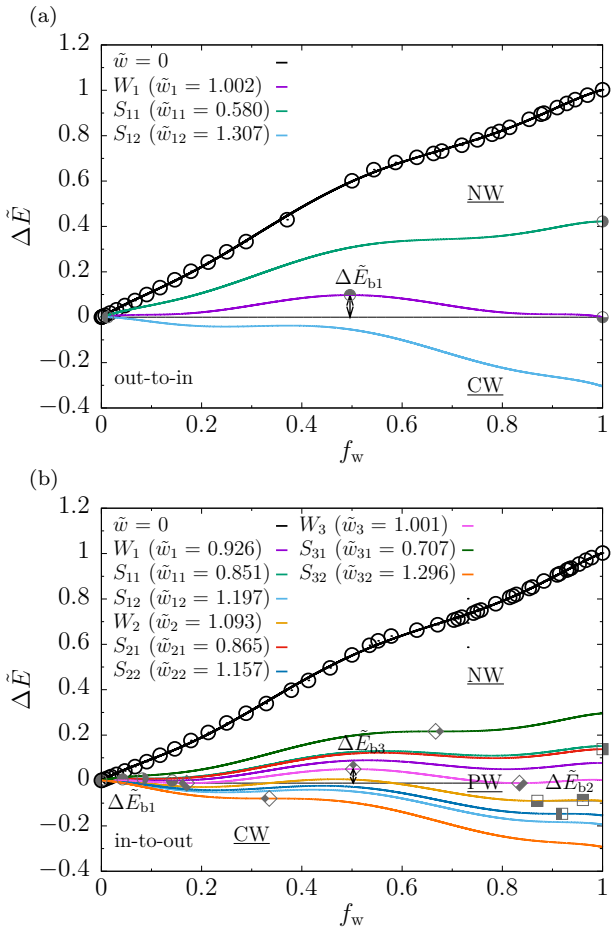

Figure 5.2: Reduced wrapping energies $\Delta\tilde{E}$ as function of the wrapping fraction f_w for (a) out-to-in and (b) in-to-out wrapping. The reduced particle size is $\tilde{R}_p = 0.1$, and the reduced distance is $\tilde{D} = 2.5$. Different reduced adhesion strengths $\tilde{w}$ associated with wrapping transitions are shown. The open circles are numerical results for membrane tethers wrapping particles. The black lines are fit functions. NW, PW and CW with underlines are globally stable non-wrapped, partial-wrapped and complete-wrapped states. W_1 is the binding-envelopment transition between NW and CW states in (a), or the binding transition between NW and PW states in (b), W_2 is the envelopment transition between PW and CW states, and W_3 is the wrapping transition between two PW states; S_{11} and S_{12}, S_{21} and S_{22}, S_{31} and S_{32} are spinodals associated with W_1, W_2 and W_3, respectively. $\Delta\tilde{E}_{b1}$, $\Delta\tilde{E}_{b2}$, and $\Delta\tilde{E}_{b3}$ are energy barriers between NW and CW or PW for W_1, PW and CW for W_2, and two PW for W_3, respectively. For the transition W_1 / W_2 / W_3, the non-wrapped / partial-wrapped / partial-wrapped state that corresponds with the complete-wrapped or partial-wrapped state is indicated by p_1 (◒) / p_5 (⬓) / p_9 (◆) and p_{10} (◆), and the energy barrier by p_2 (◓) / p_6 (⬒) / p_{11} (◈). The energy barrier vanishes at p_3 (◐) / p_7 (◧) / p_{12} (◈) for spontaneous wrapping, and at p_4 (◑) / p_8 (◨) / p_{13} (◈) for spontaneous unwrapping.

tion $p_1 = 1$ have the same energy as the non-wrapped state, the energy barrier $\Delta\tilde{E}_{b1}$ is measured at wrapping fraction p_2. The saddle points p_3 and p_4

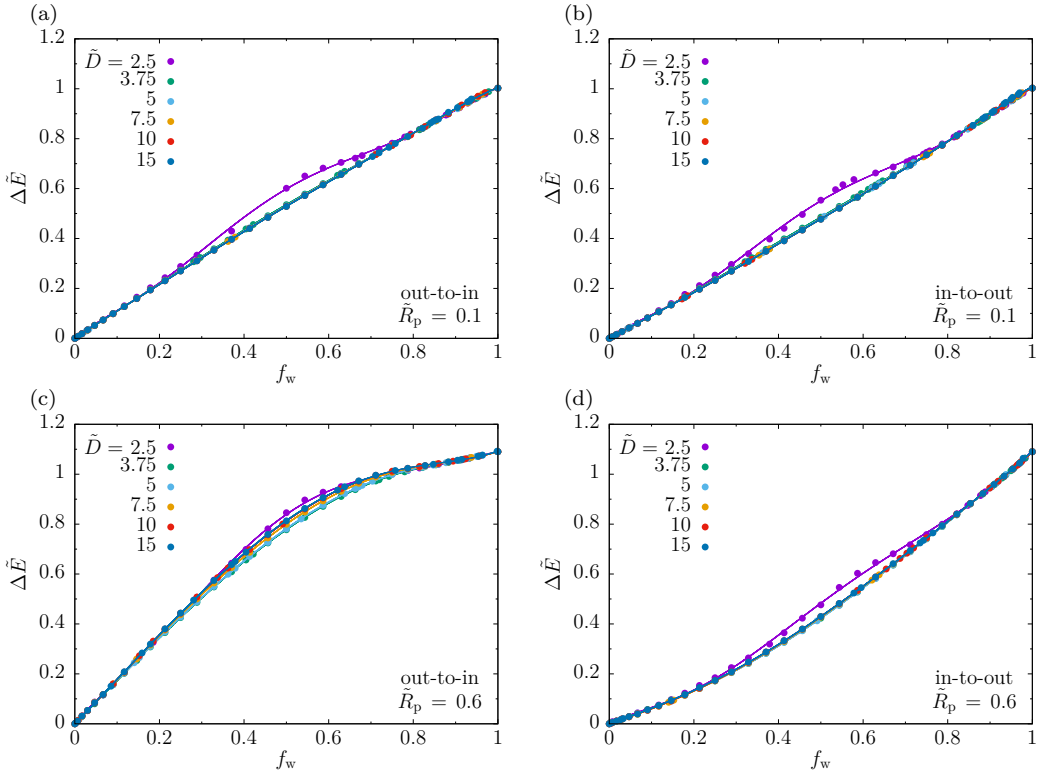

Figure 5.3: Reduced wrapping energies $\Delta\tilde{E}$ as a function of the wrapping fraction f_w for different reduced distances $\tilde{D}$ for (a, c) out-to-in and (b, d) in-to-out wrapping. The reduced particle size is $\tilde{R}_p = 0.1$ and 0.6 for (a, b) and (c, d), respectively. Parameters are same as that in Fig. 5.2.

correspond to the spinodals S_{12} and S_{11} where the energy barrier vanishes, respectively. Analogously, for adhesion strength w_2 the partial-wrapped state at point p_5 (see Fig. 5.2(b)) has an equal energy as the complete-wrapped state. The corresponding energy maximum $\Delta\tilde{E}_{b2}$ is found at the point p_6. At the saddle points p_7 and p_8 for the spinodals S_{22} and S_{21}, the energy barrier vanishes. Therefore, for adhesion strength w_3 two partial-wrapped states (see Fig. 5.2(b)) with same energies are indicated by the points p_9 and p_{10}, the corresponding energy maximum $\Delta\tilde{E}_{b3}$ is found at the point p_{11}. The saddle points are p_{12} and p_{13}, where the energy barrier vanishes for the spinodals S_{32} and S_{31}.

For out-to-in wrapping, as shown in Fig. 5.2(a), the binding-envelopment transition W_1 is discontinuous with an energy barrier $\Delta\tilde{E}_{b1}$. For in-to-out wrapping, as shown in Fig. 5.2(b), both the binding transition W_1 and envelopment transition W_2 are discontinuous and characterized by the energy barriers $\Delta\tilde{E}_{b1}$ and $\Delta\tilde{E}_{b2}$, respectively. For the shallow-deep transition W_3, the two stable partial-wrapped states are separated by energy barriers $\Delta\tilde{E}_{b3}$.

An energy barrier $\Delta\tilde{E}_{b1}$ between the non-wrapped and the complete-wrapped

or a partial-wrapped state indicates that the binding-envelopment or the binding transition W_1 is discontinuous. Decreasing or increasing the adhesion strength further, the energy barrier $\Delta\tilde{E}_{\rm b1}$ vanishes at adhesion strengths w_{11} and w_{12} for the spinodals S_{11} or S_{12}, respectively. For adhesion strengths $w_{11} < \tilde{w} < \tilde{w}_1$, a metastable complete-wrapped (CW) or partial-wrapped (PW) coexists with the stable non-wrapped (NW) state. For adhesion strength $\tilde{w}_1 < \tilde{w} < w_{12}$, the metastable non-wrapped state coexists with a stable complete-wrapped or partial-wrapped state. Similarly, an energy barrier $\Delta\tilde{E}_{\rm b2}$ between a stable partial-wrapped and the complete-wrapped state indicates that the envelopment transition W_2 is discontinuous. S_{21} and S_{22} are spinodals; for adhesion strengths $w_{21} < \tilde{w} < \tilde{w}_2$, a stable partial-wrapped state coexists with a metastable complete-wrapped state, for adhesion strengths $\tilde{w}_2 < \tilde{w} < w_{22}$, the stable complete-wrapped state coexists with a metastable partial-wrapped state. Also, the shallow-deep transition W_3 is discontinuous and S_{31} and S_{32} are spinodals for which energy barriers $\Delta\tilde{E}_{\rm b3}$ vanish.

Wrapping energies relative to the non-wrapped states $\Delta\tilde{E}$ have been calculated for fixed reduced particle size $\tilde{R}_{\rm p}$ and various reduced distances $\tilde{D}$. Figures 5.3(a) and (b) show membrane deformation energies as function of the wrapping fraction $f_{\rm w}$ for $\tilde{R}_{\rm p} = 0.1$. For out-to-in wrapping, at the complete-wrapped state, $f_{\rm w} = 1$, the lines with different distances $\tilde{D}$ focus on a point that is slightly larger than $\Delta\tilde{E} = 1$, as the reduced bending energies relative to the non-wrapped states are 1, and the reduced tension energies relative to the non-wrapped states are $\tilde{R}_{\rm p}^2\,/\,4$, which are smaller than the reduced bending energies. For distance $\tilde{D} = 2.5$, the deformation energies are largest for wrapping fractions $0.2 < f_{\rm w} < 0.8$. For in-to-out wrapping, the deformation energies are smaller than that for out-to-in wrapping for same wrapping fractions $0 < f_{\rm w} < 1$. The largest energies are also found for $\tilde{D} = 2.5$ for $0.2 < f_{\rm w} < 0.8$.

For $\tilde{R}_{\rm p} = 0.6$, as shown in Figs. 5.3(c) and (d), the deformation energies at the complete-wrapped states are $\Delta\tilde{E} = 1.09$. For out-to-in wrapping, the energies increase sharply for $0 < f_{\rm w} < 0.8$, and increase slowly for $0.8 < f_{\rm w} < 1$. The smallest energies for $0.3 < f_{\rm w} < 0.8$ are found for $\tilde{D} = 3.75$, which indicates an optimal distance for particle wrapping. For in-to-out wrapping, the deformation energies are smaller than that for out-to-in wrapping. The energies for $0.3 < f_{\rm w} < 0.8$ are larger for $\tilde{D} = 2.5$ than that for other distances.

5.3 Results

5.3.1 Wrapping transitions

We focus on the adhesion strengths for the wrapping transitions W_1 and W_2, see Fig. 5.4. Three regimes with different combination of stable non-wrapped,

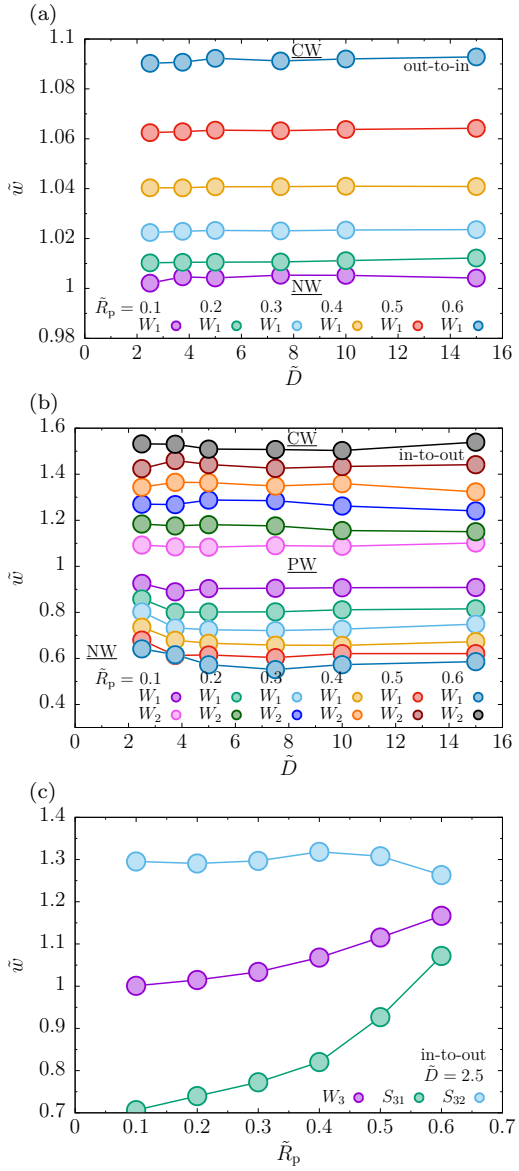

Figure 5.4: Wrapping states for particles with reduced adhesion strengths $\tilde{w}$, reduced distances $\tilde{D}$, and reduced particle sizes $\tilde{R}_p$ for (a) out-to-in and (b, c) in-to-out wrapping. W_1 is the binding-envelopment transition separating stable NW and CW states, or the binding transition separating the stable NW and PW states, W_2 is the envelopment transition separating stable PW and CW states, and W_3 is the wrapping transition separating the two stable PW states. S_{31} and S_{32} are spinodals for which energy barriers vanish.

partial-wrapped, and complete-wrapped states can be identified. For out-to-in wrapping, see Fig. 5.4(a), a direct transition between the non-wrapped and the complete-wrapped states takes place at adhesion strength $\tilde{w}_1$. The values of $\tilde{w}_1$ increase linearly with $\tilde{R}_p^2$ and are independent of $\tilde{D}$: $\tilde{w}_1 = 1 + \tilde{R}_p^2 / 4$. Our numerical results are consistent with the analytical values (data for analytical

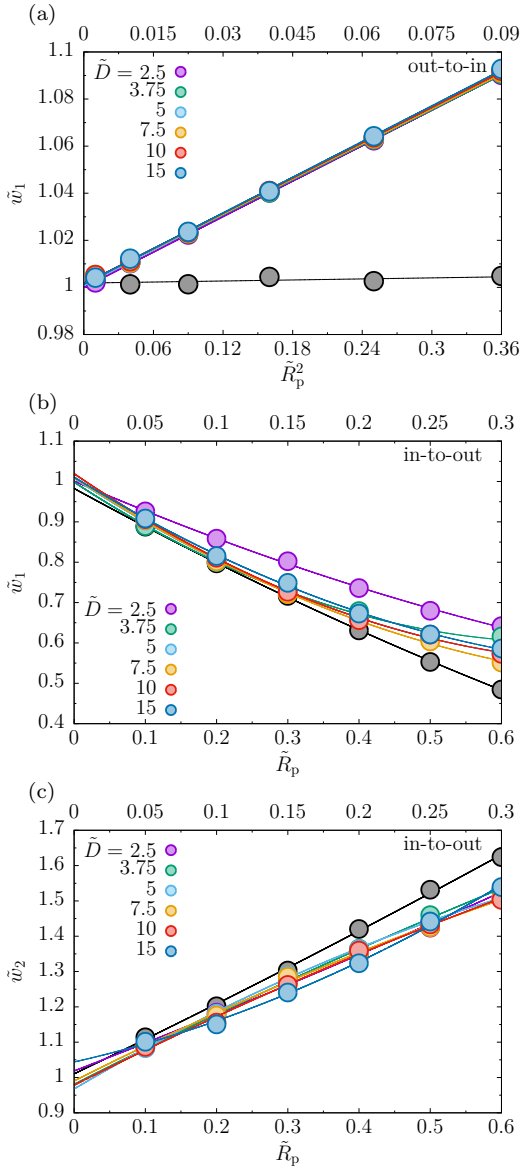

Figure 5.5: Reduced adhesion strengths $\tilde{w}$ as function of the reduced particle size $\tilde{R}_\mathrm{p}$ for (a) out-to-in and (b, c) in-to-out wrapping. The black points are numerical results for a spherical vesicle wrapping a spherical nanoparticle; the ratio of the radii of the particle and the vesicle is $\tilde{R}_\mathrm{p} = R_\mathrm{p}/R_\mathrm{v}$, where $R_\mathrm{v} = 2R_\mathrm{t}$. The lines are polynomial fit functions with degree 1 for (a) and 2 for (b, c).

results are not shown). This indicates that complete-wrapping is easier for small $\tilde{R}_\mathrm{p}$. For in-to-out wrapping, a stable partial-wrapped state is found for all different $\tilde{R}_\mathrm{p}$ and $\tilde{D}$, see Fig. 5.4(b). The adhesion strengths $\tilde{w}_1$ for the binding transitions W_1 are smaller compared with out-to-in wrapping. The values of $\tilde{w}_1$ decrease with increasing reduced distance for $\tilde{D} \leq 5$ and are independent of the reduced distance for $\tilde{D} > 5$. The values of $\tilde{w}_2$ for the

envelopment transitions W_2 are also independent of $\tilde{D}$.

Shallow-deep transitions W_3 between two stable partial-wrapped states with small and large wrapping fractions are found for $\tilde{D} = 2.5$ and in-to-out wrapping, see Fig. 5.4(c). The values of $\tilde{w}_3$, associated with W_3, increase with increasing reduced particle size $\tilde{R}_\mathrm{p}$. The adhesion strengths for spinodals S_{31} and S_{32}, for which the energy barriers vanish, increase and decrease with increasing $\tilde{R}_\mathrm{p}$.

The adhesion strengths $\tilde{w}_1$ and $\tilde{w}_2$, for a single spherical vesicle wrapping a single spherical nanoparticle, are shown in Fig. 5.5. For out-to-in wrapping, the adhesion strengths for the binding-envelopment transitions W_1 are $\tilde{w}_1 = 1$ for various vesicle-particle radii ratios $\tilde{R}_\mathrm{p} = R_\mathrm{p}/R_\mathrm{v}$ where $R_\mathrm{v} = 2R_\mathrm{t}$, see the black points in Fig. 5.5(a). This is different from the linear relationship for membrane tethers and particles. For in-to-out wrapping, the binding transition W_1 between the non-wrapped and a partial-wrapped state occurs at the adhesion strength $\tilde{w}_1$ that is almost independent on the reduced distance $\tilde{D} > 2.5$. For $\tilde{D} = 2.5$, $\tilde{w}_1$ shifts to larger values. For increasing $\tilde{R}_\mathrm{p} = R_\mathrm{p}/R_\mathrm{v}$, the onset of wrapping occurs for decreasing adhesion strength [14], which indicates that a small vesicle facilitates the attachment of the particle to the membrane, see the black points in Fig. 5.5(b). The values of $\tilde{w}_1$ for membrane tethers with reduced particle sizes $\tilde{R}_\mathrm{p} > 0.3$ are larger than that for vesicles. For $\tilde{R}_\mathrm{p} = 0$, the binding transition occurs at $\tilde{w}_1 \approx 1$ as expected for a planar membrane. The adhesion strength $\tilde{w}_2$, associated with the envelopment transitions W_2, increases with increasing $\tilde{R}_\mathrm{p}$, and is also not strongly dependent on $\tilde{D}$. For reduced particle sizes $\tilde{R}_\mathrm{p} > 0.3$, $\tilde{w}_2$ is smaller for tether-particle systems compared with vesicle-particle systems, see Fig. 5.5(c). Again, as expected for a spherical particle at a planar membrane, the adhesion strengths occurs at $\tilde{w}_2 \approx 1$ for $\tilde{R}_\mathrm{p} = 0$.

5.3.2 Energy barriers

Figure 5.6 shows energy barriers for both out-to-in and in-to-out wrapping. The binding-envelopment transitions W_1 for out-to-in wrapping are discontinuous, characterized by energy barriers $\Delta\tilde{E}_\mathrm{b1}$, see Fig. 5.6(a). For a given reduced particle size $\tilde{R}_\mathrm{p}$, the maximal heights of $\Delta\tilde{E}_\mathrm{b1}$ are found for $\tilde{D} = 2.5$. For $\tilde{D} \neq 2.5$, the heights of energy barriers are independent of reduced distance $\tilde{D}$ for $\tilde{R}_\mathrm{p} = 0.1$, 0.2 and 0.3; For $\tilde{R}_\mathrm{p} = 0.4$, 0.5 and 0.6, the heights of energy barriers increase with increasing $\tilde{D}$. This indicates that there is an optimal distance for particle wrapping. Also, tethers with larger $\tilde{R}_\mathrm{p}$ have larger energy barriers $\Delta\tilde{E}_\mathrm{b1}$. For in-to-out wrapping, as shown in Fig. 5.6(b), energy barrier $\Delta\tilde{E}_\mathrm{b1}$ for the binding transitions W_1 is only found for small reduced distance $\tilde{D} = 2.5$, no matter how large the reduced particle sizes $\tilde{R}_\mathrm{p}$ are. Continuous envelopment transitions W_2 without energy barriers $\Delta\tilde{E}_\mathrm{b2}$ are found for

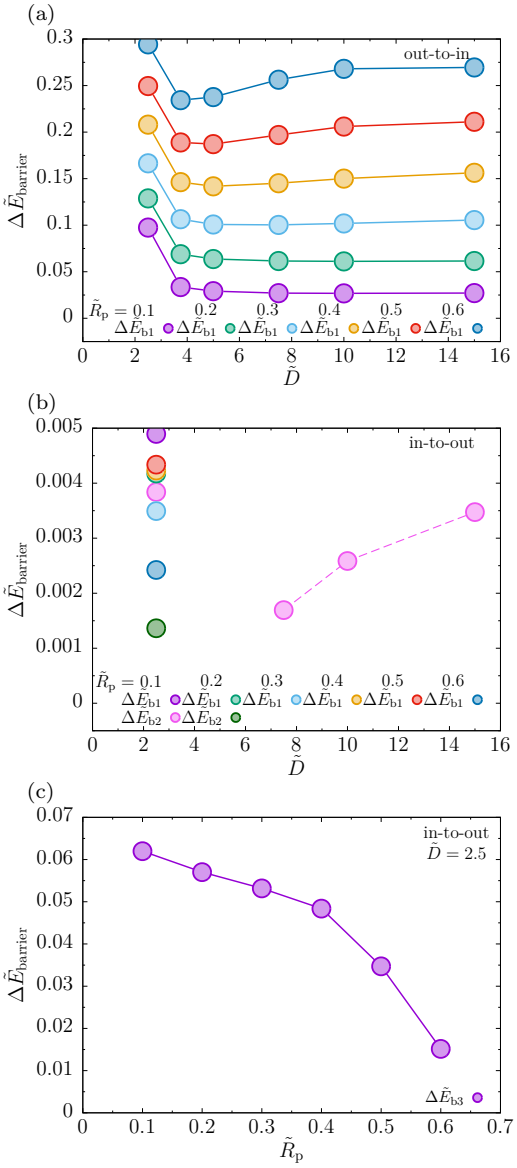

Figure 5.6: Energy barriers $\Delta\tilde{E}$ as function of the reduced distance $\tilde{D}$, and the reduced particle size $\tilde{R}_{\rm p}$ for (a) out-to-in wrapping and (b, c) in-to-out wrapping. $\Delta\tilde{E}_1$ is the barrier for the binding-envelopment or the binding transition W_1 between the non-wrapped and the complete-wrapped state or the partial-wrapped state; $\Delta\tilde{E}_2$ is the barrier for the envelopment transition W_2 between the partial-wrapped and the complete-wrapped state; $\Delta\tilde{E}_3$ is the barrier for the shallow-deep transition W_3 between two partial-wrapped states.

$\tilde{R}_{\rm p} = 0.3$, 0.4, and 0.5. For $\tilde{R}_{\rm p} = 0.2$, only a small energy barrier $\Delta\tilde{E}_{\rm b2}$ is found for $\tilde{D} = 2.5$; for $\tilde{R}_{\rm p} = 0.1$, the values of $\Delta\tilde{E}_{\rm b2}$ increase with increasing $\tilde{D} \geq 7.5$. Compared to out-to-in wrapping, the heights of energy barriers are only about 1/100 of the energy barriers for in-to-out wrapping.

Energies barriers $\Delta\tilde{E}_{\rm b3}$ associated with shallow-deep transitions W_3 are

found for $\tilde{D} = 2.5$ and in-to-out-wrapping, see Fig. 5.6(c). The values of $\Delta\tilde{E}_{\mathrm{b3}}$ increase with increasing $\tilde{R}_{\mathrm{p}}$ and are much smaller than those for out-to-in wrapping.

5.3.3 Membrane-mediated nanoparticle interactions

As discussed in Sec. 5.3.1, stable partial-wrapped states are found for all tether-particle systems for in-to-out wrapping, despite the diverse values of reduced particle size $\tilde{R}_{\mathrm{p}}$ and reduced distance $\tilde{D}$. To investigate the membrane-mediated particle interactions for different sizes of tethers, we choose the adhesion strengths $0.933 \leq \tilde{w} \leq 1.083$ for which the particles are found in stable partial-wrapped states, see Fig. 5.4(b). For reduced particle size $\tilde{R}_{\mathrm{p}} = 0.1$, as shown in Fig. 5.7(a), the minimal reduced total energies $\Delta\tilde{E}$ are non-monotonic with reduced distances $\tilde{D}$. For $0.933 \leq \tilde{w} \leq 1.008$, $\Delta\tilde{E}$ decreases with increasing $\tilde{D}$. The mutual repulsion of the nanoparticles increases with decreasing separation $\tilde{D}$. For $1.033 \leq \tilde{w} \leq 1.058$, the interaction of neighboring particles is weakly attractive for $2.5 \leq \tilde{D} \leq 5$. If $\tilde{D}$ increases, the particle interaction becomes slightly repulsive. For $\tilde{w} = 1.083$, the membrane-mediated interaction for nanoparticles is attractive for all $\tilde{D}$. An attractions that leads to linear rod-like aggregation along the cylinder axis, has been reported in both experimental and theoretical studies [234–242]. For $\tilde{R}_{\mathrm{p}} = 0.3$, as shown in Fig. 5.7(b), in the short reduced-distance range, $\Delta\tilde{E}$ decreases rapidly with increasing reduced distance $\tilde{D}$, and increases slightly with long-distance range. The lowest energy $\Delta\tilde{E}$ is found for reduced distance $\tilde{D} = 7.5$; representative snapshots are shown in Fig. 5.1(b). For $\tilde{R}_{\mathrm{p}} = 0.6$, see Fig. 5.7(c), the dependence of the reduced total energy $\Delta\tilde{E}$ on the distance $\tilde{D}$ is quantitatively similar to that for $\tilde{R}_{\mathrm{p}} = 0.3$; strong short-distance repulsive and weak long-distance attractive interactions. Instead of forming a compact linear aggregation along axis direction, we predict an optimal reduced separation $\tilde{D} = 5$.

Wrapping fractions f_{w} for stable partial-wrapped states are shown in Figs. 5.7 (d) - (f) and in Fig. S1 of the supporting information. For fixed adhesion strength, the wrapping fractions can be non-monotonic with increasing reduced distances $\tilde{D}$ for small reduced particle size $\tilde{R}_{\mathrm{p}} = 0.1$, see Fig. 5.7(d). For $0.933 \leq \tilde{w} \leq 0.983$, f_{w} increases with increasing $\tilde{D}$. However, the wrapping fractions f_{w} for the stable partial-wrapped states are always well below 0.4. For $1.008 \leq \tilde{w} \leq 1.083$, f_{w} decreases with increasing $\tilde{D}$, and the wrapping fractions f_{w} lie in a wider regime $0.6 \leq f_{\mathrm{w}} \leq 0.9$. Similarly, for $\tilde{R}_{\mathrm{p}} = 0.3$ and short reduced distances $\tilde{D} \leq 5$, the wrapping fraction f_{w} increases rapidly with increasing distance $\tilde{D}$ when the reduced adhesion strengths are small $0.933 \leq \tilde{w} \leq 1.033$. For large adhesion strengths $1.058 \leq \tilde{w} \leq 1.083$, the wrapping fractions f_{w} decrease with increasing $\tilde{D}$. For long reduced distances $\tilde{D} > 5$, the wrapping fractions f_{w} are not strongly dependent on the reduced

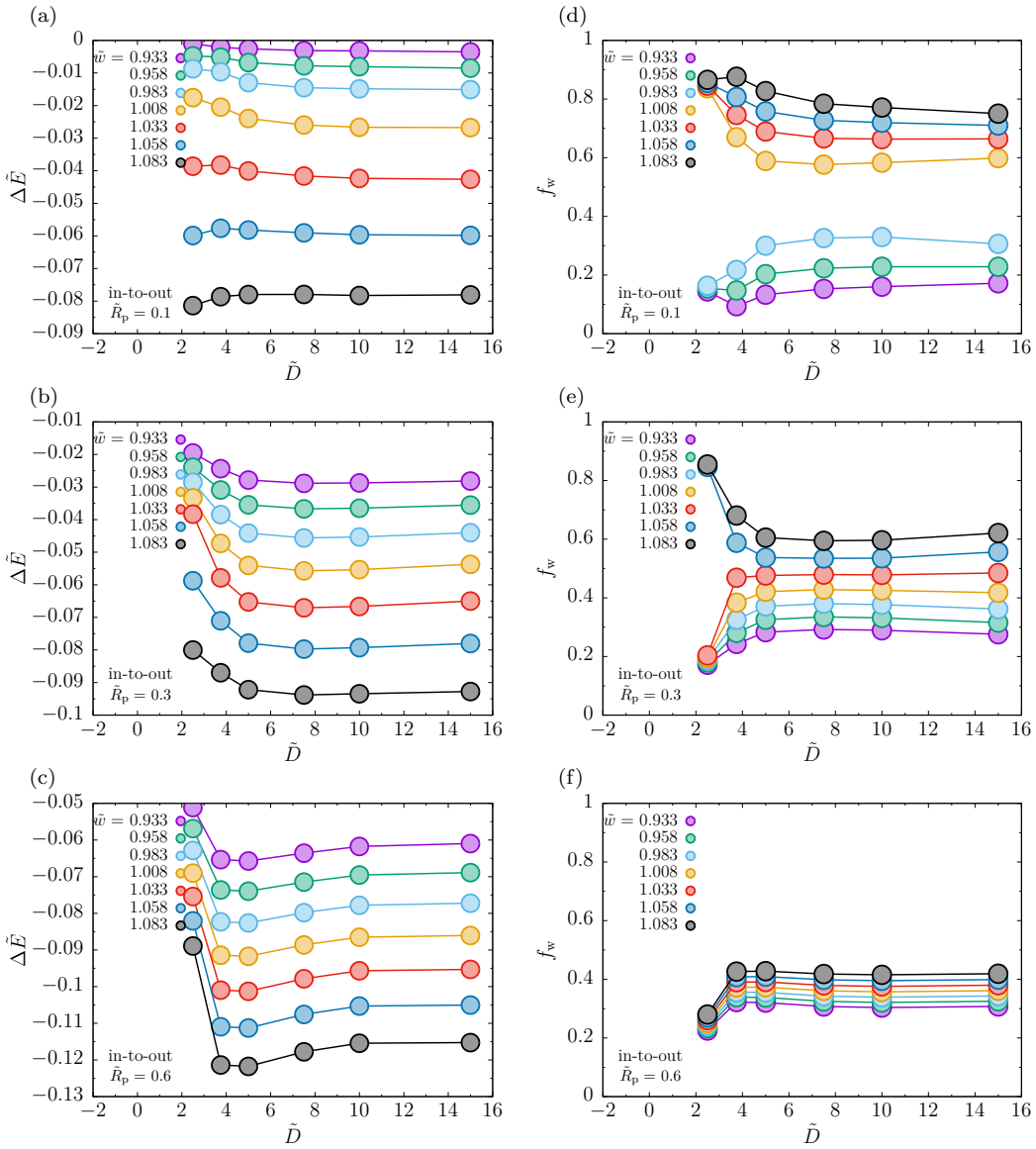

Figure 5.7: Reduced wrapping energies $\Delta\tilde{E}$ and wrapping fractions f_w as functions of reduced distance $\tilde{D}$ for (a, d) $\tilde{R}_p = 0.1$, (b, e) $\tilde{R}_p = 0.3$, and (c, f) $\tilde{R}_p = .6$ for in-to-out wrapping.

distance $\tilde{D}$. For $\tilde{R}_p = 0.6$, the wrapping fractions f_w for stable partial-wrapped states are more similar for the various reduced adhesion strengths $\tilde{w}$ than for the other systems that we studied. For reduced distance $\tilde{D} = 2.5$, the lowest energies are found for wrapping fractions $f_w \approx 0.2$; for distance $\tilde{D} > 2.5$, the wrapping fractions for lowest energies are $0.3 < f_w < 0.5$.

5.3.4 Contact-line deformations

In this chapter, we study for the first time a system that is not cylindrically symmetric. Therefore the contact line where the membrane detaches from the particles is not circular. We therefore characterize nanoparticle wrapping membrane tether, in addition, by using the difference of the maximal and minimal height along the contact line at the particle, Δh, see Fig. C2 in the appendix C. Figure 5.8 shows the variation of $\Delta\tilde{h} = \Delta h/R_\mathrm{p}$ with f_w for membrane tethers with various $\tilde{R}_\mathrm{p}$ and $\tilde{D}$. For out-to-in wrapping and $\tilde{R}_\mathrm{p} = 0.1$, as shown in Fig. 5.8(a), $\Delta\tilde{h}$ grows non-linearly from zero with increasing wrapping fraction, attains a peak value, and finally vanishes for $f_\mathrm{w} = 1$. For reduced distance $\tilde{D} = 2.5$, the peak occurs at wrapping fraction $f_\mathrm{w} \approx 0.4$, and the height of the peak is $\Delta\tilde{h} \approx 0.4$. For increasing $\tilde{D}$, the peak shifts to larger $f_\mathrm{w} \approx 0.5$ for $\tilde{D} = 3.75$ and 5 to smaller $f_\mathrm{w} \approx 0.2$ for $3.75 \leq \tilde{D} \leq 15$. Here, the height of the peak, which in the range of $0.05 < \Delta\tilde{h} < 0.1$, depends non-monotonically on $\tilde{D}$. For in-to-out wrapping, see Fig. 5.8(b), the position of the peak is $f_\mathrm{w} \approx 0.4$ and its height decreases from $\Delta\tilde{h} \approx 0.45$ for $\tilde{D} = 2.5$ to $\Delta\tilde{h} \approx 0.05$ for $\tilde{D} = 15$.

For out-to-in wrapping and $\tilde{R}_\mathrm{p} = 0.3$, as shown in Fig. 5.8(c), both position and height of the peak are not linearly dependent on the reduced distance $\tilde{D}$. The maximal height $\Delta\tilde{h} \approx 0.3$ is found for wrapping fraction $f_\mathrm{w} \approx 0.4$ where $\tilde{D} = 2.5$; while the minimal height $\Delta\tilde{h} \approx 0.05$ is found for $f_\mathrm{w} \approx 0.2$, where $\tilde{D} = 3.75$. For in-to-out wrapping, see Fig. 5.8(d), the peak height decreases monotonically with increasing reduced distance $\tilde{D}$. It is slightly larger than in Fig. 5.8(b) for fixed $\tilde{D}$. The positions are in the range $0.3 < f_\mathrm{w} < 0.4$.

Figure 5.8(e) shows that for out-to-in wrapping and $\tilde{R}_\mathrm{p} = 0.6$, the peak heights for different reduced distances $\tilde{D}$ are similar. It is $0.1 < \Delta\tilde{h} < 0.2$, while the wrapping factions varies also in a small range $0.3 < f_\mathrm{w} < 0.4$. Intriguingly, three local maximal height differences $\Delta\tilde{h}$ are found for reduced distance $\tilde{D} = 2.5$. For in-to-out wrapping as shown in Fig. 5.8(f), the peak heights for $\tilde{R}_\mathrm{p} = 0.6$ are larger than that for $\tilde{R}_\mathrm{p} = 0.1$ and 0.3 for same reduced distances $\tilde{D}$. The maximal height $\Delta\tilde{h} \approx 0.6$ is found for $f_\mathrm{w} \approx 0.4$ at reduced distance $\tilde{D} = 2.5$.

5.4 Conclusions

We can see from Fig. 5.4(a) that for out-to-in wrapping, the reduced adhesion strength $\tilde{w}_1$ for the binding-envelopment transition W_1 increases linearly with the reduced particle size $\tilde{R}_\mathrm{p}$. It is independent of the reduced distance $\tilde{D}$. For in-to-out wrapping, see Fig. 5.4(b), the value of the adhesion strength $\tilde{w}_1$ associated with the binding transition W_1 is shifted to larger values for short distances $\tilde{D}$, and remains constant for long distances. For the envelopment transition W_2, the reduced adhesion strength $\tilde{w}_2$ increases with increasing $\tilde{R}_\mathrm{p}$,

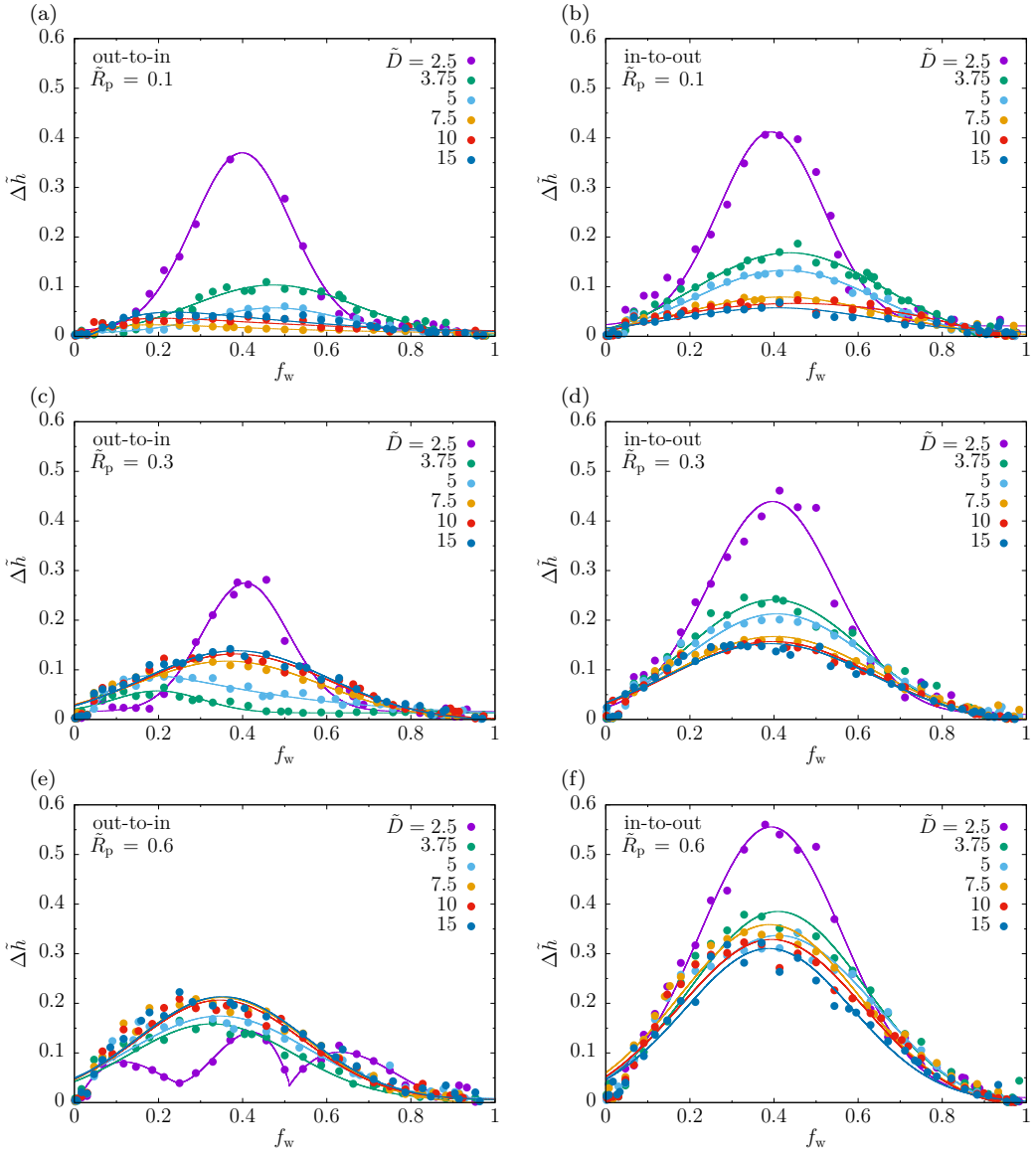

Figure 5.8: Reduced maximal height differences $\Delta\tilde{h}$ along the contact lines as function of wrapping fraction f_w for (a, c, e) out-to-in and (b, d, f) in-to-out wrapping. The solid lines are Gaussian or Lognormal Gaussian fit functions. For $\tilde{D} = 2.5$ in subfigure (e), the fit function is piece-wise polynomial with degree 3.

which is in contrast to the change of the adhesion strength $\tilde{w}_1$ with $\tilde{R}_p$. Therefore, the range of adhesion strengths for which a stable partial-wrapped state exists increases with increasing $\tilde{R}_p$. Furthermore, $\tilde{w}_2$ is independent of the distance $\tilde{D}$. For the shallow wrapped-deep wrapped transitions W_3 in Fig. 5.4(c), the transition between two partial-wrapped states at adhesion strength $\tilde{w}_3$ is only found for short distance $\tilde{D} = 2.5$ and for in-to-out wrapping. Tethers with large $\tilde{R}_p$ have large values of $\tilde{w}_3$.

Compared to the adhesion strengths for a single spherical vesicle wrapping a particle, for out-to-in wrapping, as shown in Fig. 5.5(a), the binding-envelopment transition occurs at $\tilde{w}_1 = 1$ for different reduced particle size $\tilde{R}_\mathrm{p}$. For in-to-out wrapping, as shown in Figs. 5.5(b) and (c), the values of $\tilde{w}_1$ are larger and $\tilde{w}_2$ are smaller for particle-tether than particle-vesicle systems, especially for large reduced particle size $\tilde{R}_\mathrm{p}$.

Figures 5.4 and 5.6 characterize the discontinuous binding-envelopment transitions W_1 between the non-wrapped and complete-wrapped state. Most of the binding transitions W_1 between the non-wrapped and a stable partial-wrapped, and the envelopment transitions W_2 between a stable partial-wrapped and the complete-wrapped states are continuous. The energy barriers $\Delta\tilde{E}_\mathrm{b1}$ associated with binding-envelopment transitions are non-monotonic with the reduced distance $\tilde{D}$, the minimum is found for $\tilde{D} = 5$. For a given distance $\tilde{D}$, the tethers with small $\tilde{R}_\mathrm{p}$ have small energy barriers. Regarding the shallow-deep transitions W_3 between two stable partial-wrapped states, the heights of the energy barriers decrease with increasing $\tilde{R}_\mathrm{p}$.

Previous studies in Refs. [234–242] show that for both planar membranes and curved membranes, particles always attract. Linear aggregates, such as ring, rod and helical shapes on the membrane are found. In our numerical simulations of highly-curved tethers where the particles are initially located inside the tethers, see Fig. 5.7, we find complex interaction behavior: particles attract or repel each other, depending on the values of reduced particle size $\tilde{R}_\mathrm{p}$, the reduced distance $\tilde{D}$, and the reduced adhesion strength $\tilde{w}$.

We also discussed maximal height differences of the contact lines for the tethers that wrap particles. As shown in Fig. 5.8, the maximal heights are found for $\tilde{D} = 2.5$ where the wrapping fraction is $f_\mathrm{w} \approx 0.4$. The heights and the positions of the maximal peaks are non-monotonic with both $\tilde{R}_\mathrm{p}$ and $\tilde{D}$ for out-to-in wrapping, while the heights of peaks decrease with decreasing $\tilde{R}_\mathrm{p}$ and increasing $\tilde{D}$, and the wrapping fractions of peaks are in a small range $0.3 \leq f_\mathrm{w} \leq 0.4$ for in-to-out wrapping.

We investigated the roles of the reduced particle size $\tilde{R}_\mathrm{p}$ and the reduced distance $\tilde{D}$ on the wrapping of spherical particles by highly curved tethers. The tethers prior to wrapping are cylinders with constant radii $R_\mathrm{t} = \sqrt{\kappa/(2\sigma)}$. Depending on the initial positions of particles, we studied two distinct wrapping processes which are respectively named as out-to-in and in-to-out wrapping: particles initially located outside or inside the tethers enter or exit the tethers, respectively.

For in-to-out wrapping, the reduced adhesion strength decreases with increasing $\tilde{R}_\mathrm{p}$ for the binding transition, but increases with increasing $\tilde{R}_\mathrm{p}$ for the envelopment transition. It demonstrates that the onset of wrapping is easier for a small tube, but more difficult to completely wrap the entire particle. Continuous binding and envelopment transition without energy barriers are found

for large $\tilde{R}_{\mathrm{p}}$ and large $\tilde{D}$. A rich mixture of attractive and repulsive interactions between nanoparticles is found to be related to the geometric and elastic parameters, such as $\tilde{R}_{\mathrm{p}}$, $\tilde{D}$ and $\tilde{w}$, for membrane-mediated local deformations.

Chapter 6

Conclusions

Components, structures, types, and mechanical and physicochemical properties for nanoparticle-membrane systems have been discussed and studied in detail. A thorough understanding of nanoparticle-membrane interactions is important for at least two reasons. One one hand, the information obtained from nanoparticle-membrane interactions helps to develop new generations of nanomaterials. For instance, efficient drug delivery systems can be engineered by tuning the adhesion and wrapping properties of the nanoparticles that are used as delivery vector. On the other hand, nanoparticle-membrane interactions are key to understand mechanisms how biological cells control nano-scale cargoes entering and exiting, in order to regulate the balance of material inside the cell. My research focused on the roles of biophysical parameters (e.g. size, shape, and elastic curvature) of both nanoparticle and vesicles for wrapping and provides hints how to control nanoparticle-transport processes across membranes,such as endocytosis and exocytosis.

Computer simulations are versatile tools to study the interactions between nanoparticles and membranes. Depending on the system of interest, a variety of models accounting for different length and time scales have been developed. Popular approaches include quantum models, all-atom or coarse-grained models, and continuum membrane models. Here, a continuum membrane model based on Helfrich Hamiltonian has been used to study membrane deformation energies and stable states for nanoparticle wrapping at vesicles and membrane tethers. Three stable wrapping states are found: the non-wrapped, the partial-wrapped, and the complete-wrapped state. Furthermore, vesicle shape transitions have been calculated depending on the wrapping state of the particle. If stable partial-wrapped states are found, separate binding and envelopment transitions exist, otherwise a combined binding-envelopment transition is found. The transitions can be continuous without an energy barrier or discontinuous with an energy barrier.

For nanoparticle uptake by vesicles, complex wrapping have been systematically calculated for various particle sizes, vesicle sizes and shapes, reduced

vesicle volumes, membrane spontaneous curvatures, as well as for out-to-in and in-to-out particle wrapping. Nanoparticle wrapping transitions are found to be coupled to vesicle shape transitions. Stable partial-wrapped states for nanoparticle wrapping induce vesicle shapes that can be different from the stable shapes without particles for the same vesicle sizes and reduced volumes, and membrane spontaneous curvatures. Shape transitions are always found to be discontinuous. For vesicles with variable volume under physiological conditions, an important factor that affects the wrapping behavior of vesicles is an osmotic pressure difference between the interior and the exterior. Osmotic pressure leads to a new type of shape transitions between "wide necks" and "narrow necks" around the particles that is otherwise only reported for large particle size to vesicle size ratios. For high solute concentrations, stable partial-wrapped states are found both for nanoparticles entering into and exiting from vesicle. This is different from wrapping without solute at spherical vesicles, where stable partial-wrapped states are only found for in-to-out wrapping. The energy barrier for the discontinuous envelopment transition increases with increasing solute concentration. For nanoparticles interacting with membrane tethers, the calculations for nanoparticle wrapping by the highly-curved cylindrical membranes predict both attractive and repulsive membrane-mediated interactions between nanoparticles, which depend on the distance between the particles, the ratio of particle radius and tube radius, as well as on the particle-membrane adhesion strength. The deformation of the contact lines between the adhered and the free vesicle membrane can be used to characterize the influence of neighboring nanoparticles on the wrapping state of the nanoparticle under consideration.

The calculations in this thesis provide systematic studies and reveal qualitatively new aspects for passive nanoparticle-membrane interactions. Further studies may include also active, and assisting biological processes, which can extend this work for model systems to nanoparticles at biological cells.

Appendix A

Nanoparticle wrapping by non-spherical vesicles

This appendix provides supplementary materials for Chapter 3 "Nanoparticle wrapping by non-spherical vesicles", and it contains calculational details for the energy minimisation including volume and area constraints, and the equations for calculating reduced volumes prior to and after wrapping. We plot spinodals for out-to-in and in-to-out wrapping for reduced particle size $\tilde{R}_{\mathrm{p}} = 0.2$, reduced volume $v = 0.7$, and reduced spontaneous curvature $\tilde{c}_0 = -0.063$.

A.1 Volume and area constraints

Both vesicle volume and total membrane area have target values during the energy minimisation. For each minimization step, Surface Evolver attempts to achieve these values by additional vertex moves. The procedure works analogously for both volume and area constraints and is described in the following exemplarily for a volume constraint [182].

As part of the energy minimization, a first step corrects for the deviation of the actual volume from the target volume. Assuming that the actual volume V of the vesicle deviates from the target volume by $\delta V = \mid V - V_{\mathrm{tar}} \mid$, the vertices are moved by

$$\mathbf{R}_i = c_{\mathrm{V}}\, \mathbf{g}_{\mathrm{Vi}} \text{ for each vertex } i\,, \tag{A1}$$

where $\mathbf{g}_{\mathrm{Vi}}$ is the gradient of the volume for the coordinates of each vertex i of the triangular membrane. Here, the desired volume correction $\delta V = -\sum_i (c_{\mathrm{V}}\, \mathbf{g}_{\mathrm{Vi}}) \cdot \mathbf{g}_{\mathrm{V_{tar,i}}}$ determines

$$c_{\mathrm{V}} = -\frac{\delta V}{\sum_i \mathbf{g}_{\mathrm{Vi}} \cdot \mathbf{g}_{\mathrm{V_{tar,i}}}}\,. \tag{A2}$$

In a second step, the positions of the vertices are optimised in while preserving the vesicle volume. For a total force F_i on the vertex i, the projection of this force on the subspace of volume-preserving motions is

$$\mathbf{F}_\mathrm{i,proj} = F_\mathrm{i} - \sum_i p\,\mathbf{g}_\mathrm{Vi} \text{ for each vertex } i\,. \tag{A3}$$

The condition $\sum_i \mathbf{F}_\mathrm{i,proj} \cdot \mathbf{g}_\mathrm{Vi} = 0$ is used to determine the excess pressure

$$p = \frac{\sum_i \mathbf{F}_\mathrm{i,proj} \cdot \mathbf{g}_\mathrm{Vi}}{\sum_i \mathbf{g}_\mathrm{Vi} \cdot \mathbf{g}_\mathrm{Vtari}}\,. \tag{A4}$$

in the vesicle at equilibrium.

A.2 Reduced volumes after complete wrapping

For a vesicle prior to wrapping a particle, the reduced volume is given by Eq. (3.5). When a particle enters the vesicle completely, the vesicle volume $V = 4/3\pi R_\mathrm{v}^3$ effectively increases by the particle volume V_p while its membrane area A decreases by the surface area of the particle A_p. The effective reduced volume after wrapping,

$$v_2 = \frac{6\sqrt{\pi}\,(V + V_\mathrm{p})}{(A - A_\mathrm{p})^{3/2}} = \frac{v + (R_\mathrm{p}/R_\mathrm{v})^3}{[1 - (R_\mathrm{p}/R_\mathrm{v})^2]^{3/2}}\,, \tag{A5}$$

has therefore increased compared with the reduced volume prior to wrapping. When a particle exits a vesicle completely, the reduced volume after wrapping,

$$v_2 = \frac{6\sqrt{\pi}\,(V - V_\mathrm{p})}{(A - A_\mathrm{p})^{3/2}} = \frac{v - (R_\mathrm{p}/R_\mathrm{v})^3}{[1 - (R_\mathrm{p}/R_\mathrm{v})^2]^{3/2}}\,, \tag{A6}$$

can both decrease and increase, see Fig. 3.6.

A.3 Spinodals for wrapping transitions

Figure A1 shows, in addition to the data shown in Fig. 3.3 in the main text, regimes for metastable non-wrapped, partial-wrapped, and complete-wrapped states. For discontinuous transitions spinodals indicate the adhesion strengths at that wrapping and unwrapping transitions take place spontaneously. For $\tilde{R}_\mathrm{p} = 0.2$, $v = 0.7$, and out-to-in wrapping, see Fig. A1(a), for negative $\tilde{c}_0$

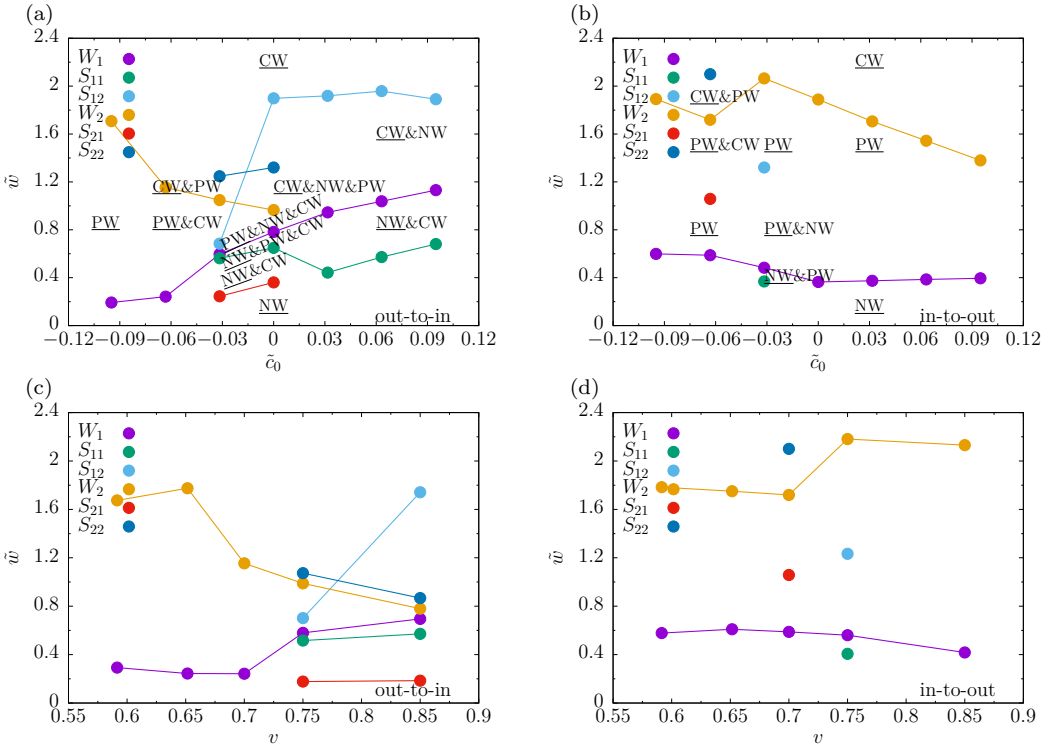

Figure A1: Reduced adhesion strengths $\tilde{w}$ for reduced particle size $\tilde{R}_\mathrm{p} = 0.2$, (a, b) for $v = 0.7$, as function of the reduced spontaneous curvature $\tilde{c}_0$, (c, d) for $\tilde{c}_0 = -0.063$ as function of the reduced volume v for out-to-in and in-to-out wrapping. In addition to the adhesion strengths for the transitions shown in Fig. 3.3 of the main text, also the spinodals S_{11} and S_{12} for W_1 and S_{21} and S_{22} for W_2 are shown. S_{11} and S_{21} denote unwrapping spinodals, S_{12} and S_{22} wrapping spinodals. Complete-wrapped (CW), partial-wrapped (PW), and non-wrapped (NW) states are indicated. Globally stable states are underlined in order to distinguish them from metastable states.

continuous binding and envelopment transitions occur, followed by discontinuous binding and envelopment transitions, and finally discontinuous combined binding-envelopment transitions with increasing $\tilde{c}_0$. For $\tilde{R}_\mathrm{p} = 0.2$, $v = 0.7$, and in-to-out wrapping, see Fig. A1(b), separate binding and envelopment transitions occur for all values of $\tilde{c}_0$; they are discontinuous only for combined wrapping and shape transitions. Also for $\tilde{R}_\mathrm{p} = 0.2$ and $\tilde{c}_0 = -0.063$, see Figs. A1(c, d), we find separate binding and envelopment transitions for all reduced volumes that are only discontinuous if they are combined with shape transitions.

Appendix B

Osmotic pressure matters for nanoparticle-vesicle interaction

This appendix provides supplementary materials for Chapter 4 "Osmotic pressure matters for nanoparticle-vesicle interactions", and it contains calculational details for the adhesion strengths of individual binding and envelopment transitions, and the relationship between the osmotic constant $\tilde{n}_{\mathrm{v}}$ and the reduced adhesion strength $\tilde{w}$ for the combined binding-envelopment transition.

B.1 Binding and envelopment transitions

The continuous binding transition between the non-wrapped and a stable partial-wrapped state is independent of the osmotic pressure, the reduced adhesion strength $\tilde{w}$ associated with the binding transition is expressed as a function of the particle-vesicle radii ratio $\tilde{R}_{\mathrm{p}}$ [13],

$$\tilde{w} = (1 + R_{\mathrm{p}}/R_{\mathrm{v}})^2 \tag{B1}$$

for out-to-in wrapping, and

$$\tilde{w} = (1 - R_{\mathrm{p}}/R_{\mathrm{v}})^2 \tag{B2}$$

for in-to-out wrapping.

Similarly, the reduced adhesion strength for the continuous envelopment transition between a stable partial-wrapped state and the complete-wrapped state is expressed as

$$\tilde{w} = \left(1 + \frac{R_{\mathrm{p}}/R_{\mathrm{v}}}{\sqrt{1 - (R_{\mathrm{p}}/R_{\mathrm{v}})^2}}\right)^2 \tag{B3}$$

for in-to-out wrapping.

B.2 Binding-envelopment transition

For the non-wrapped state, the spherical vesicle has a membrane area A and the outside nanoparticle has an area A_p. The bending energy of the vesicle is $8\pi\kappa$ and the osmotic pressure is zero as the reduced volume $v = 1$. For the complete-wrapped state, the nanoparticle is connected to the vesicle with a patch of infinitely small catenoid-like membrane of vanishing bending energy cost, both the adhered membrane and the free membrane form sphere deformations, which gives the bending energy $16\pi\kappa$. The osmotic energy can be calculated by substituting the following equation into Eq. (4.3),

$$\begin{aligned} v &= \frac{4}{3}\pi \left[\left(\frac{A - A_\mathrm{p}}{4\pi} \right)^{3/2} - R_\mathrm{p}^3 \right] \Big/ \left[\frac{4}{3}\pi \left(\frac{A}{4\pi} \right)^{3/2} \right] \\ &= \left[1 - (R_\mathrm{p}/R_\mathrm{v})^2 \right]^{3/2} - (R_\mathrm{p}/R_\mathrm{v})^3 \,, \end{aligned} \tag{B4}$$

where $R_\mathrm{p} = \sqrt{A_\mathrm{p}/(4\pi)}$ and $R_\mathrm{v} = \sqrt{A/(4\pi)}$.

Suppose the total energy for the non-wrapped state is equal to the complete-wrapped state, we can get the relationship between the osmotic constant $\tilde{n}_\mathrm{v}$ and the reduced adhesion strength $\tilde{w}$ for the binding-envelopment transition,

$$\tilde{n}_\mathrm{v} = \frac{(\tilde{w} - 1) \cdot 8\pi\kappa}{v - \ln v - 1} \tag{B5}$$

as we combine the Eq. (B4) with Eq. (4.1).

Appendix C

Tether-mediated nanoparticle interaction

This appendix provides supplementary materials for Chapter 5 "Tether-mediated nanoparticle interaction". It shows the minimal reduced energies $\Delta\tilde{E}$ and wrapping fractions f_{w} for different reduced adhesion strengths $0.933 \leq \tilde{w} \leq 1.083$ for in-to-out wrapping, as well as the deformation of the contact line on a spherical particle that is partially wrapped by the membrane of tether for out-to-in and in-to-out wrapping for reduced particle size $\tilde{R}_{\mathrm{p}} = 0.3$ and reduced distance $\tilde{D} = 7.5$.

C.1 Minimal energies and wrapping fractions for specific adhesion strengths

For in-to-out wrapping, stable partial-wrapped states are found for adhesion strengths $0.933 \leq \tilde{w} \leq 1.083$. The minimal reduced energies $\Delta\tilde{E}$ as a function of the wrapping fraction f_{w} for different adhesion strengths $\tilde{w}$ are shown for $\tilde{R}_{\mathrm{p}} = 0.3$ and $\tilde{D} = 7.5$ in Fig. C1. Figure 5.7 in Chapter 5 shows an overview over the reduced energies $\Delta\tilde{E}$ and wrapping fractions f_{w} for a variety of $\tilde{R}_{\mathrm{p}}$ and $\tilde{D}$.

C.2 Contact line deformations for nanoparticles

Figure C2 shows the deformation of the contact line on a spherical nanoparticle wrapped by the membrane of tether, see Fig. 5.1 for the representative snapshots. The contact line is pulled up along y-axis (the longitudinal axis of tethers), and is pulled down along the x-axis. The difference of the highest

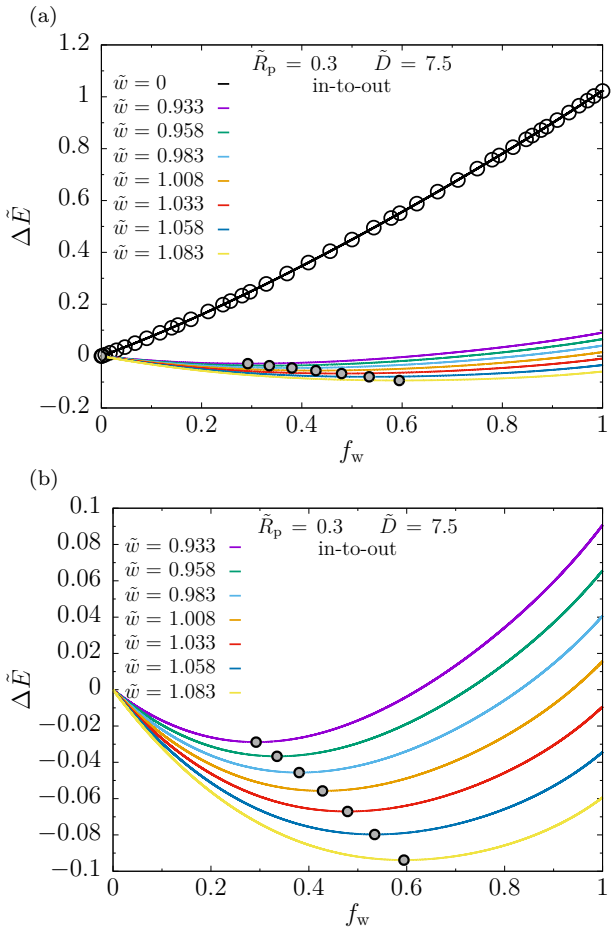

Figure C1: Reduced wrapping energies $\Delta\tilde{E}$ for reduced particle size $\tilde{R}_p = 0.3$ and reduced distance $\tilde{D} = 7.5$ as function of wrapping fraction for in-to-out wrapping. For subfigure (a), the numerical results for deformation energies with adhesion strength $\tilde{w} = 0$ are shown as open circle points, and solid black line is the fit function; the minimal reduced energies are marked by the solid gray points for adhesion strengths $0.933 \leq \tilde{w} \leq 1.083$. For subfigure (b), only the minimal total energies $\Delta\tilde{E}$ for stable partial-wrapped states with adhesion strengths $0.933 \leq \tilde{w} \leq 1.083$ are shown.

(half-above filled circle) and lowest (half-below filled circle) points along the contactline, normalized by the radius of the particle, $\Delta\tilde{h} = \Delta h/R_p$, characterizes the membrane deformation of the tether around the nanoparticle. The reduced height $\Delta\tilde{h}$ along the contact line is shown as a function of wrapping fraction f_w in Fig. 5.8 in Chapter 5.

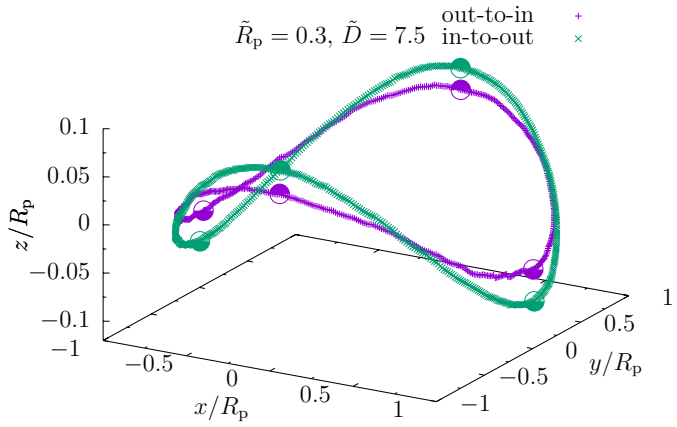

Figure C2: Contact-line deformations for a spherical particle of reduced particle size $\tilde{R}_\mathrm{p} = 0.3$ and reduced distance $\tilde{D} = 7.5$ at a membrane tether with wrapping fraction $f_\mathrm{w} = 0.41$ for both out-to-in (purple points) and in-to-out (green points) wrapping. The highest and lowest positions are indicated by circles that are half-above and half-below filled.

References

[1] D. P. Cormode, P. A. Jarzyna, W. J. Mulder, Z. A. Fayad, *Adv. Drug Deliv. Rev.* **2010**, *62*, 329–338.

[2] B. M. Simonet, M. Valcárcel, *Anal. Bioanal. Chem.* **2009**, *393*, 17.

[3] L. Marks, L Peng, *J. Phys. Condens. Matter* **2016**, *28*, 053001.

[4] I. Khan, K. Saeed, I. Khan, *Arab. J. Chem.* **2017**.

[5] S. Bhatia in Natural Polymer Drug Delivery Systems: Nanoparticles, Plants, and Algae, Springer, **2016**, pp. 33–93.

[6] K. Letchford, H. Burt, *Eur. J. Pharm. Biopharm.* **2007**, *65*, 259–269.

[7] G. L. Nicolson, *Biochim. Biophys. Acta.* **2014**, *1838*, 1451–1466.

[8] C Monzel, K Sengupta, *J. Phys. D* **2016**, *49*, 243002.

[9] L.-G. Wu, E. Hamid, W. Shin, H.-C. Chiang, *Annu. Rev. Physiol.* **2014**, *76*, 301–331.

[10] N. Oh, J.-H. Park, *Int. J. Nanomed.* **2014**, *9*, 51–63.

[11] U. Seifert, R. Lipowsky, *Phys. Rev. A* **1990**, *42*, 4768.

[12] P. B. Sunil Kumar, G Gompper, R Lipowsky, *Phys. Rev. Lett.* **2001**, *86*, 3911–3914.

[13] J. Agudo-Canalejo, R. Lipowsky, *ACS Nano* **2015**, *9*, 3704–3720.

[14] A. H. Bahrami, R. Lipowsky, T. R. Weikl, *Soft Matter* **2016**, *12*, 581–587.

[15] S. Dasgupta, T. Auth, G. Gompper, *Nano Lett.* **2014**, *14*, 687–693.

[16] S. Dasgupta, T. Auth, G. Gompper, *Soft Matter* **2013**, *9*, 5473–5482.

[17] B. D. Chithrani, A. A. Ghazani, W. C. Chan, *Nano Lett.* **2006**, *6*, 662–668.

[18] B. D. Chithrani, W. C. Chan, *Nano Lett.* **2007**, *7*, 1542–1550.

[19] W. Helfrich, *Z. Naturforsch. C* **1973**, *28*, 693–703.

[20] P. B. Canham, *J. Theor. Biol.* **1970**, *26*, 61–81.

[21] M. Deserno, *Chem. Phys. Lipids.* **2015**, *185*, 11–45.

[22] D. Argudo, N. P. Bethel, F. V. Marcoline, M. Grabe, *Biochim. Biophys. Acta.* **2016**, *1858*, 1619–1634.

[23] R. Lipowsky, E. Sackmann in Structure and Dynamics of Membranes, (Eds.: R. Lipowsky, E. Sackmann), Elsevier, **1995**.

[24] G. A. Jamieson, D. M. Robinson in Mammalian Cell Membranes: Surface Membranes of Specific Cell Types v. 3, (Eds.: G. A. Jamieson, D. M. Robinson), Butterworths, **1977**.

[25] M. D. Birch, PhD thesis, **2016**.

[26] R. B. Gennis in Biomembranes: Molecular Structure and Function, (Ed.: R. B. Gennis), Springer-Verlag New York Inc., **2013**.

[27] K. M. Bushell, C. Söllner, B. Schuster-Boeckler, A. Bateman, G. J. Wright, *Genome Res.* **2008**, *18*, 622–630.

[28] C. M. Sanderson, *Brief Funct. Genomic. Proteomic.* **2009**, *8*, 1–11.

[29] S. Curry, *Interdiscip Sci. Rev.* **2015**, *40*, 308–328.

[30] P. J. Stansfeld, J. E. Goose, M. Caffrey, E. P. Carpenter, J. L. Parker, S. Newstead, M. S. Sansom, *Structure* **2015**, *23*, 1350–1361.

[31] Q. Cui, L. Zhang, Z. Wu, A. Yethiraj, *Curr. Opin. Solid State Mater. Sci.* **2013**, *17*, 164–174.

[32] R. W. Tourdot, N Ramakrishnan, R. Radhakrishnan, *Phys. Rev. E* **2014**, *90*, 022717.

[33] T. R. Graham, M. M. Kozlov, *Curr. Opin. Cell Biol.* **2010**, *22*, 430–436.

[34] J. Bigay, B. Antonny, *Dev. Cell* **2012**, *23*, 886–895.

[35] J. Zimmerberg, M. M. Kozlov, *Nat. Rev. Mol. Cell Biol.* **2006**, *7*.

[36] H. T. McMahon, J. L. Gallop, *Nature* **2005**, *438*, 590–596.

[37] T. Baumgart, B. R. Capraro, C. Zhu, S. L. Das, *Annu. Rev. Phys. Chem.* **2011**, *62*, 483–506.

[38] V. K. Bhatia, N. S. Hatzakis, D. Stamou in Seminars in Cell & Developmental Biology, *Vol. 21*, Elsevier, **2010**, pp. 381–390.

[39] G. Khelashvili, D. Harries, H. Weinstein, *Biophys. J.* **2009**, *97*, 1626–1635.

[40] G. M. Cooper in The Cell: A Molecular Approach, *Vol. 85*, (Eds.: G. M. Cooper, R. E. Hausman), Sinauer Associates Sunderland, **2000**.

[41] R. A. Dwek, *Chem. Rev.* **1996**, *96*, 683–720.

[42] J. Clamp, G Dawson, L Hough, *Biochim. Biophys. Acta Gen. Subj.* **1967**, *148*, 342–349.

[43] G. L. Nicolson, *Biochim. Biophys. Acta Rev. Biomembr.* **1976**, *457*, 57–108.

[44] F Contreras, L. Sánchez-Magraner, A. Alonso, F. M. Goñi, et al., *FEBS Lett.* **2010**, *584*, 1779–1786.

[45] D. Duque, X.-j. Li, K. Katsov, M. Schick, *J. Chem. Phys.* **2002**, *116*, 10478–10484.

[46] O. G. Mouritsen, M. Bloom, *Biophys. J.* **1984**, *46*, 141–153.

[47] G. L'heureux, M Fragata, *Biophys. Chem.* **1988**, *30*, 293–301.

[48] A De la Maza, J. L. Parra, *Biochem. J.* **1994**, *303*, 907–914.

[49] A. C. Woodka, P. D. Butler, L. Porcar, B. Farago, M. Nagao, *Phys. Rev. Lett.* **2012**, *109*, 058102.

[50] S Tristram-Nagle, R Zhang, R. Suter, C. Worthington, W. Sun, J. Nagle, *Biophys. J.* **1993**, *64*, 1097–1109.

[51] R. Vácha, F. J. Martinez-Veracoechea, D. Frenkel, *Nano Lett.* **2011**, *11*, 5391–5395.

[52] Z. G. Qu, X. C. He, M. Lin, B. Y. Sha, X. H. Shi, T. J. Lu, F. Xu, *Nanomedicine* **2013**, *8*, 995–1011.

[53] A. A. Alabi, R. W. Tsien, *Annu. Rev. Physiol.* **2013**, *75*, 393–422.

[54] E. L. Clayton, M. A. Cousin, *J. Neurochem.* **2009**, *111*, 901–914.

[55] N. C. Harata, A. M. Aravanis, R. W. Tsien, *J. Neurochem.* **2006**, *97*, 1546–1570.

[56] J. A. Pickett, J. M. Edwardson, *Traffic* **2006**, *7*, 109–116.

[57] J. Heuser, T. Reese, *J. Cell Biol.* **1981**, *88*, 564–580.

[58] J. H. Hurley, E. Boura, L.-A. Carlson, B. Różycki, *Cell* **2010**, *143*, 875–887.

[59] J. S. Bonifacino, J. Lippincott-Schwartz, *Nat. Rev. Mol. Cell Biol.* **2003**, *4*, 409–414.

[60] M. Bremser, W. Nickel, M. Schweikert, M. Ravazzola, M. Amherdt, C. A. Hughes, T. H. Söllner, J. E. Rothman, F. T. Wieland, *Cell* **1999**, *96*, 495–506.

[61] S. M. Stagg, C. Gürkan, D. M. Fowler, P. LaPointe, T. R. Foss, C. S. Potter, B. Carragher, W. E. Balch, *Nature* **2006**, *439*, 234.

[62] S. Chiantia, N. Kahya, J. Ries, P. Schwille, *Biophys. J.* **2006**, *90*, 4500–4508.

[63] H. Heller, M. Schaefer, K. Schulten, *J. Phys. Chem.* **1993**, *97*, 8343–8343.

[64] R. Lipowsky, *J. Phys. II* **1992**, *2*, 1825–1840.

[65] W. Römer, L. Berland, V. Chambon, K. Gaus, B. Windschiegl, D. Tenza, M. R. Aly, V. Fraisier, J.-C. Florent, D. Perrais, et al., *Nature* **2007**, *450*, 670–675.

[66] S. Horikoshi, N. Serpone, *MWI* **2013**, 1–24.

[67] T. Noda, H. Ebihara, Y. Muramoto, K. Fujii, A. Takada, H. Sagara, J. H. Kim, H. Kida, H. Feldmann, Y. Kawaoka, *PLoS Pathog.* **2006**, *2*, e99.

[68] X. Yi, H. Gao, *ACS Biomater. Sci. Eng.* **2017**, DOI 10.1021/acsbiomaterials.6b00815.

[69] W. Gao, C.-M. J. Hu, R. H. Fang, L. Zhang, *J. Mater. Chem. B* **2013**, *1*, 6569–6585.

[70] G. A. Hughes, *Nanomed. Nanotechnol. Biol. Med.* **2005**, *1*, 22–30.

[71] S Dasgupta, T Auth, G Gompper, *J. Phys.: Condens. Matter* **2017**, *29*, 373003.

[72] R. Zaouk, B. Y. Park, M. J. Madou, *Microfluid. Technol.* **2006**, 5–15.

[73] D. Guo, G. Xie, J. Luo, *J. Phys. D: Appl. Phys* **2014**, *47*, 013001.

[74] B. Ji, J. Maeda, M. Higuchi, K. Inoue, H. Akita, H. Harashima, T. Suhara, *Life Sci.* **2006**, *78*, 851–855.

[75] J. Kreuter, *J. Nanosci. Nanotechnol.* **2004**, *4*, 484–488.

[76] Y. Kato, Y. Sugiyama, *Crit. Rev. Ther. Drug* **1997**, *14*.

[77] W. M. Pardridge, *Nat. Rev. Drug Discovery* **2002**, *1*.

[78] G. Sharma, A. R. Sharma, J.-S. Nam, G. P. C. Doss, S.-S. Lee, C. Chakraborty, *J. Nanobiotechnology* **2015**, *13*, 74.

[79] C. Gomes, R. G. Moreira, E. Castell-Perez, *J. Food Sci.* **2011**, *76*.

[80] J. Wang, M. Sui, W. Fan, *Curr. Drug Metab.* **2010**, *11*, 129–141.

[81] J. M. de la Fuente, C. C. Berry, M. O. Riehle, A. S. Curtis, *Langmuir* **2006**, *22*, 3286–3293.

[82] D. P. Cormode, P. A. Jarzyna, W. J. Mulder, Z. A. Fayad, *Adv. Drug Delivery Rev.* **2010**, *62*, 329–338.

[83] K. Lee, D. Kelly, F. O'Neal, J. Stadler, G. Kennedy, *Fundam. Appl. Toxicol.* **1988**, *11*, 1–20.

[84] Y. Wang, S. A. Shaikh, E. Tajkhorshid, *Physiology* **2010**, *25*, 142–154.

[85] C. K. Haluska, K. A. Riske, V. Marchi-Artzner, J.-M. Lehn, R. Lipowsky, R. Dimova, *Proc. Natl. Acad. Sci. U.S.A* **2006**, *103*, 15841–15846.

[86] H. Noguchi, *J. Phys. Soc. Jpn.* **2009**, *78*, 041007–041007.

[87] H. I. Ingólfsson, C. Arnarez, X. Periole, S. J. Marrink, *J. Cell Sci.* **2016**, *129*, 257–268.

[88] G. S. Ayton, G. A. Voth, *Curr. Opin. Struct. Biol.* **2009**, *19*, 138–144.

[89] K. M. Merz Jr, *Acc. Chem. Res.* **2014**, *47*, 2804–2811.

[90] M. González, *JDN* **2011**, *12*, 169–200.

[91] G. Groenhof in Biomolecular Simulations, (Eds.: L. Monticelli, E. Salonen), New York Humana Press, **2013**.

[92] H. J. Berendsen in Simulating the Physical World: Hierarchical Modeling from Quantum Mechanics to Fluid Dynamics, Cambridge University Press, **2007**.

[93] K. Kappel, Y. Miao, J. A. McCammon, *Q. Rev. Biophys.* **2015**, *48*, 479–487.

[94] A. J. Clark, P. Tiwary, K. Borrelli, S. Feng, E. B. Miller, R. Abel, R. A. Friesner, B. Berne, *J. Chem. Theory Comput.* **2016**, *12*, 2990–2998.

[95] M. Chavent, A. L. Duncan, M. S. Sansom, *Curr. Opin. Struct. Biol.* **2016**, *40*, 8–16.

[96] W. L. Ash, M. R. Zlomislic, E. O. Oloo, D. P. Tieleman, *Biochim. Biophys. Acta.* **2004**, *1666*, 158–189.

[97] N. M. Luscombe, R. A. Laskowski, J. M. Thornton, *Nucleic Acids Res.* **2001**, *29*, 2860–2874.

[98] Q. Yu, W. Ye, C. Jiang, R. Luo, H.-F. Chen, *J. Phys. Chem. B* **2014**, *118*, 12426–12434.

[99] Q. Yu, W. Ye, W. Wang, H.-F. Chen, *PloS one* **2013**, *8*, e59627.

[100] J. Gay, B. Berne, *J. Chem. Phys.* **1981**, *74*, 3316–3319.

[101] X. Liu, X. Zhang, G. Zhou, X. Yao, S. Zhang, *Science China Chemistry* **2012**, 1–7.

[102] S. Hug in Biomolecular Simulations, (Eds.: L. Monticelli, E. Salonen), New York Humana Press, **2013**.

[103] W. Shinoda, R. DeVane, M. L. Klein, *J. Phys. Chem. B* **2010**, *114*, 6836–6849.

[104] M. Orsi, M. G. Noro, J. W. Essex, *J. Royal Soc. Interface* **2011**, *8*, 826–841.

[105] S. J. Marrink, D. P. Tieleman, *Chem. Soc. Rev.* **2013**, *42*, 6801–6822.

[106] T. Bereau, Z.-J. Wang, M. Deserno, *J. Chem. Phys.* **2014**, *140*, 03B615_1–11220.

[107] W. Noid, *J. Chem. Phys.* **2013**, *139*, 09B201_1.

[108] H. I. Ingolfsson, C. A. Lopez, J. J. Uusitalo, D. H. de Jong, S. M. Gopal, X. Periole, S. J. Marrink, *Wiley Interdiscip. Rev. Comput. Mol. Sci.* **2014**, *4*, 225–248.

[109] Z. Wu, W. Pang, G. M. Coghill, *Soft computing* **2015**, *19*, 1595–1610.

[110] F. J.-M. De Meyer, M. Venturoli, B. Smit, *Biophys. J.* **2008**, *95*, 1851–1865.

[111] J.-M. Frédérick, J. M. Rodgers, T. F. Willems, B. Smit, *Biophys. J.* **2010**, *99*, 3629–3638.

[112] M. Müller, K. Katsov, M. Schick, *Phys. Rep.* **2006**, *434*, 113–176.

[113] J. Yoo, M. B. Jackson, Q. Cui, *Biophys. J.* **2013**, *104*, 841–852.

[114] M. Baaden, S. J. Marrink, *Curr. Opin. Struct. Biol.* **2013**, *23*, 878–886.

[115] A. Renevey, S. Riniker, *J. Chem. Phys.* **2017**, *146*, 124131.

[116] S. Riniker, J. R. Allison, W. F. van Gunsteren, *Phys. Chem. Chem. Phys.* **2012**, *14*, 12423–12430.

[117] G Gompper, T Ihle, D. Kroll, R. Winkler in Advanced Computer Simulation Approaches For Soft Matter Sciences III, Springer, **2009**, pp. 1–87.

[118] M Ripoll, K Mussawisade, R. Winkler, G Gompper, *EPL* **2004**, *68*, 106.

[119] M. Simunovic, A. Srivastava, G. A. Voth, *Proc. Natl. Acad. Sci. U.S.A* **2013**, *110*, 20396–20401.

[120] H. Yu, K. Schulten, *PLOS Comput. Biol.* **2013**, *9*, e1002892.

[121] C. Wu, J.-E. Shea, *Curr. Opin. Struct. Biol.* **2011**, *21*, 209–220.

[122] A. Morriss-Andrews, F. L. Brown, J.-E. Shea, *J. Phys. Chem. B* **2014**, *118*, 8420–8432.

[123] G. Gompper, D. M. Kroll in Statistical Mechanics of Membranes and Surfaces, (Eds.: D. R. Nelson, T. Piran, S. Weinberg), World Scientific, Singapore, **2004**.

[124] G Gompper, D. Kroll, *J. Phys.: Condens. Matter* **1997**, *9*, 8795.

[125] T.-P. Fries, H. Matthies, *Informatikbericht Scientific Computing Univ. Braunschweig* **2004**.

[126] J.-M. Drouffe, A. Maggs, S Leibler, *Science* **1991**, 1353–1356.

[127] H. Noguchi, G. Gompper, *Phys. Rev. E* **2006**, *73*, 021903.

[128] C Peco, A Rosolen, M Arroyo, *J. Comput. Phys.* **2013**, *249*, 320–336.

[129] M. Ariane, M. H. Allouche, M. Bussone, F. Giacosa, F. Bernard, M. Barigou, A. Alexiadis, *PloS one* **2017**, *12*, e0174795.

[130] A. D. Pezzutti, D. A. Vega, *Phys. Rev. E* **2011**, *84*, 011123.

[131] K. Crane, Discrete Differential Geometry: An Applied Introduction, **2017**.

[132] S. A. Safran in Statistical thermodynamics of surfaces, interfaces, and membranes, *Vol. 90*, Perseus Books, **1994**.

[133] E. A. Evans, *Biophys. J.* **1974**, *14*, 923–931.

[134] M. I. Bloor, M. J. Wilson, *Phys. Rev. E* **2000**, *61*, 4218.

[135] E. Evans, V. Heinrich, F. Ludwig, W. Rawicz, *Biophys. J.* **2003**, *85*, 2342–2350.

[136] J. F. Nagle, *Faraday Discuss.* **2013**, *161*, 11–29.

[137] F David in Statistical Mechanics of Membranes and Surfaces, (Eds.: D. R. Nelson, T. Piran, S. Weinberg), World Scientific, **2004**.

[138] T. Auth, G. Gompper, *Phys. Rev. E* **2005**, *72*, 031904.

[139] S. A. Nowak, T. Chou, *Phys Rev. E* **2008**, *78*, 021908.

[140] M. Deserno, T. Bickel, *Europhys. Lett.* **2003**, *62*, 767.

[141] M. Deserno, *J. Phys. Condens. Matter.* **2004**, *16*, S2061.

[142] S. Mkrtchyan, C. Ing, J. Z. Chen, *Phys. Rev. E* **2010**, *81*, 011904.

[143] K. Khairy, J. Howard, *Soft Matter* **2011**, *7*, 2138–2143.

[144] W. Góźdź, G Gompper, *EPL* **2001**, *55*, 587.

[145] D. Kroll, G. Gompper, *Science* **1992**, *255*, 968.

[146] K. A. Brakke, Surface evolver manual, **1994**.

[147] M. Deserno, *Phys. Rev. E* **2004**, *69*, 031903.

[148] J. Agudo-Canalejo, R. Lipowsky, *Soft Matter* **2017**, *13*, 2155–2173.

[149] T. Auth, G. Gompper, *Phys. Rev. E* **2009**, *80*, 031901.

[150] B. J. Reynwar, G. Illya, V. A. Harmandaris, M. M. Müller, K. Kremer, M. Deserno, *Nature* **2007**, *447*, 461–464.

[151] E. Atilgan, S. X. Sun, *J. Chem. Phys.* **2007**, *126*, 095102.

[152] C. Saraiva, C. Praça, R. Ferreira, T. Santos, L. Ferreira, L. Bernardino, *J. Controlled Release* **2016**, *235*, 34–47.

[153] L. Guan, L. Rizzello, G. Battaglia, *Nanomed.* **2015**, *10*, 2757–2780.

[154] B. Pelaz, C. Alexiou, R. A. Alvarez Puebla, F. Alves, A. M. Andrews, S. Ashraf, L. P. Balogh, L. Ballerini, A. Bestetti, C. Brendel, et al., *ACS Nano* **2017**, *11*, 2313–2381.

[155] C. Xu, S. Sun, *Adv. Drug Delivery Rev.* **2013**, *65*, 732–743.

[156] S. Rose, A. Prevoteau, P. Elzière, D. Hourdet, A. Marcellan, L. Leibler, *Nature* **2014**, *505*, 382–385.

[157] D. K. Cureton, R. H. Massol, S. Saffarian, T. L. Kirchhausen, S. P. Whelan, *PLoS Pathog.* **2009**, *5*, e1000394.

[158] P. Ge, J. Tsao, S. Schein, T. J. Green, M. Luo, Z. H. Zhou, *Science* **2010**, *327*, 689–693.

[159] S. Dasgupta, T. Auth, N. S. Gov, T. J. Satchwell, E. Hanssen, E. S. Zuccala, D. T. Riglar, A. M. Toye, T. Betz, J. Baum, G. Gompper, *Biophys. J.* **2014**, *107*, 43–54.

[160] C. Théry, *F1000 Biol. Rep.* **2011**, *3*, 15.

[161] D. Zabeo, A. Cvjetkovic, C. Lässer, M. Schorb, J. Lötvall, J. L. Höög, *J. Extracell. Vesicles* **2017**, *6*, 1329476.

[162] P. Vader, E. A. Mol, G. Pasterkamp, R. M. Schiffelers, *Adv. Drug Delivery Rev.* **2016**, *106*, 148–156.

[163] E. Naumovska, S. Ludwanowski, N. Hersch, T. Braun, R. Merkel, B. Hoffmann, A. Csiszár, *Acta Biomater.* **2014**, *10*, 1403–1411.

[164] R. Langer, *Science* **1990**, 1527–1533.

[165] X. Yi, X. Shi, H. Gao, *Phys. Rev. Lett.* **2011**, *107*, 098101.

[166] J. Zimmerberg, M. M. Kozlov, *Nat. Rev. Mol. Cell Bio.* **2006**, *7*, 9–19.

[167] M. A. Churchward, T. Rogasevskaia, D. M. Brandman, H. Khosravani, P. Nava, J. K. Atkinson, J. R. Coorssen, *Biophys. J.* **2008**, *94*, 3976–3986.

[168] E. E. Kooijman, V. Chupin, N. L. Fuller, M. M. Kozlov, B. de Kruijff, K. N. Burger, P. R. Rand, *Biochemistry* **2005**, *44*, 2097–2102.

[169] B. D. Chithrani, A. A. Ghazani, W. C. Chan, *Nano Lett.* **2006**, *6*, 662–668.

[170] H. Yuan, J. Li, G. Bao, S. Zhang, *Phys. Rev. Lett.* **2010**, *105*, 138101.

[171] H. Gao, W. Shi, L. B. Freund, *Proc. Natl. Acad. Sci. U.S.A.* **2005**, *102*, 9469–9474.

[172] U. Seifert, K. Berndl, R. Lipowsky, *Phys. Rev. A* **1991**, *44*, 1182.

[173] R. Gupta, B. Rai, *Nanoscale* **2017**, *9*, 4114–4127.

[174] Y. Guo, E. Terazzi, R. Seemann, J. B. Fleury, V. A. Baulin, *Sci. Adv.* **2016**, *2*, e1600261.

[175] J. Barnoud, G. Rossi, L. Monticelli, *Phys. Rev. Lett.* **2014**, *112*, 068102.

[176] H. Noguchi, M. Takasu, *Biophys. J.* **2002**, *83*, 299–308.

[177] H. Noguchi, G. Gompper, *Proc. Natl. Acad. Sci. U.S.A.* **2005**, *102*, 14159–14164.

[178] T. Auth, G. Gompper, *Phys. Rev. E* **2003**, *68*, 051801.

[179] H. W. G. Lim, M. Wortis, R. Mukhopadhyay, *Proc. Natl. Acad. Sci. U.S.A.* **2002**, *99*, 16766–16769.

[180] S. T. Milner, S. Safran, *Phys. Rev. A* **1987**, *36*, 4371.

[181] P. Janmey, P. Kinnunen, *Trends Cell Biol.* **2006**, *16*, 538–546.

[182] K. A. Brakke, *Exp. Math.* **1992**, *1*, 141–165.

[183] H.-G. Döbereiner, *Curr. Opin. Colloid Int. Sci.* **2000**, *5*, 256–263.

[184] W. Góźdź, *Langmuir* **2007**, *23*, 5665–5669.

[185] C. Si-Qin, W. Guang-Hong, J. Z. Y. Chen, *Chin. Phys. B* **2015**, *24*, 098702.

[186] M. Schwarten, J. Mohrlüder, P. Ma, M. Stoldt, Y. Thielmann, T. Stangler, N. Hersch, B. Hoffmann, R. Merkel, D. Willbold, *Autophagy* **2009**, *5*, 690–698.

[187] R. L. Knorr, R. Dimova, R. Lipowsky, *PLoS One* **2012**, *7*, e32753.

[188] M. Koch, J. Baum, *Cell. Microbiol.* **2016**, *18*, 319–329.

[189] D. A. Fedosov, H. Noguchi, G. Gompper, *Biomech. Model. Mechanobiol.* **2014**, *13*, 239–258.

[190] S. El Andaloussi, I. Mäger, X. O. Breakefield, M. J. Wood, *Nat. Rev. Drug Discovery* **2013**, *12*, 347.

[191] M. Colombo, G. Raposo, C. Théry, *Annu. Rev. Cell Dev. Biol.* **2014**, *30*, 255–289.

[192] G. Raposo, W. Stoorvogel, *J. Cell. Biol.* **2013**, *200*, 373–383.

[193] C. Rauch, E. Farge, *Biophys. J.* **2000**, *78*, 3036–3047.

[194] R. Borges, E. R. Travis, S. E. Hochstetler, R. M. Wightman, *J. Biol. Chem.* **1997**, *272*, 8325–8331.

[195] T Meckel, A. Hurst, G Thiel, U Homann, *Protoplasma* **2005**, *226*, 23–29.

[196] E. Reimhult, F. Hoeoek, B. Kasemo, *Langmuir* **2003**, *19*, 1681–1691.

[197] J. A. Jackman, J.-H. Choi, V. P. Zhdanov, N.-J. Cho, *Langmuir* **2013**, *29*, 11375–11384.

[198] D. Vorselen, F. C. MacKintosh, W. H. Roos, G. J. Wuite, *ACS Nano* **2017**, *11*, 2628–2636.

[199] J. Hasan, R. J. Crawford, E. P. Ivanova, *Trends Biotechnol.* **2013**, *31*, 295–304.

[200] E. P. Ivanova, J. Hasan, H. K. Webb, G. Gervinskas, S. Juodkazis, V. K. Truong, A. H. Wu, R. N. Lamb, V. A. Baulin, G. S. Watson, et al., *Nat. Commun.* **2013**, *4*.

[201] S. Pogodin, J. Hasan, V. A. Baulin, H. K. Webb, V. K. Truong, T. H. P. Nguyen, V. Boshkovikj, C. J. Fluke, G. S. Watson, J. A. Watson, et al., *Biophys. J.* **2013**, *104*, 835–840.

[202] J. van't Hoff, *Nobel Lecture* **1901**, 5–10.

[203] K. oglkecka, P. Rangamani, B. Liedberg, R. S. Kraut, A. N. Parikh, *Elife* **2014**, *3*, e03695.

[204] A. Upadhyaya, M. P. Sheetz, *Biophys. J.* **2004**, *86*, 2923–2928.

[205] A. Karlsson, R. Karlsson, M. Karlsson, A.-S. Cans, A. Strömberg, F. Ryttsén, O. Orwar, *Nature* **2001**, *409*, 150.

[206] T. R. Powers, G. Huber, R. E. Goldstein, *Phys Rev E.* **2002**, *65*, 041901.

[207] J. White, L. Johannes, F. Mallard, A. Girod, S. Grill, S. Reinsch, P. Keller, B. Tzschaschel, A. Echard, B. Goud, et al., *J. Cell Biol.* **1999**, *147*, 743–760.

[208] J. Dai, M. P. Sheetz, *Biophys. J.* **1999**, *77*, 3363–3370.

[209] R. E. Waugh, *Biophys. J.* **1982**, *38*, 29–37.

[210] R. M. Hochmuth, N Mohandas, P. Blackshear, *Biophys. J.* **1973**, *13*, 747–762.

[211] F. Hochmuth, J.-Y. Shao, J. Dai, M. P. Sheetz, *Biophys. J.* **1996**, *70*, 358–369.

[212] F Brochard-Wyart, N Borghi, D Cuvelier, P Nassoy, *Proc. Natl. Acad. Sci. U.S.A* **2006**, *103*, 7660–7663.

[213] G. Koster, M. VanDuijn, B. Hofs, M. Dogterom, *Proc. Natl. Acad. Sci. U.S.A* **2003**, *100*, 15583–15588.

[214] C. Leduc, O. Campàs, J.-F. Joanny, J. Prost, P. Bassereau, *Biochim. Biophys. Acta.* **2010**, *1798*, 1418–1426.

[215] P. M. Shaklee, T. Idema, G. Koster, C. Storm, T. Schmidt, M. Dogterom, *Proc. Natl. Acad. Sci. U.S.A* **2008**, *105*, 7993–7997.

[216] C. M. Waterman-Storer, E. Salmon, *Curr. Biol.* **1998**, *8*, 798–807.

[217] Y. Shibata, J. Hu, M. M. Kozlov, T. A. Rapoport, *Annu. Rev. Cell Dev. Biol.* **2009**, *25*, 329–354.

[218] P. Z. C. Chia, P. A. Gleeson, *F1000Prime Rep.* **2014**, *6*.

[219] W. H. Toh, P. A. Gleeson, *Front Cell Dev Biol.* **2016**, *4*.

[220] R. E. Waugh, J. Song, S. Svetina, B Zeks, *Biophys. J.* **1992**, *61*, 974–982.

[221] R. Hochmuth, C. Evans, H. Wiles, J. McCown, *Science* **1983**, *220*, 101–102.

[222] J. Dai, M. P. Sheetz, *Biophys. J.* **1995**, *68*, 988–996.

[223] E Evans, A Yeung, *Chem. Phys. Lipids.* **1994**, *73*, 39–56.

[224] M. Angelova, S Soléau, P. Méléard, F Faucon, P Bothorel in Trends in Colloid and Interface Science VI, Springer, **1992**, pp. 127–131.

[225] M. Simunovic, E. Evergren, I. Golushko, C. Prévost, H.-F. Renard, L. Johannes, H. T. McMahon, V. Lorman, G. A. Voth, P. Bassereau, *Proc. Natl. Acad. Sci. U.S.A* **2016**, 201606943.

[226] B. Sorre, A. Callan-Jones, J. Manzi, B. Goud, J. Prost, P. Bassereau, A. Roux, *Proc. Natl. Acad. Sci. U.S.A* **2012**, *109*, 173–178.

[227] L.-C. Jiang, W.-D. Zhang, *Biosens. Bioelectron.* **2010**, *25*, 1402–1407.

[228] B.-S. Kong, D.-H. Jung, S.-K. Oh, C.-S. Han, H.-T. Jung, *J. Phys. Chem. C* **2007**, *111*, 8377–8382.

[229] H. T. Chung, J. H. Won, P. Zelenay, *Nat. Commun.* **2013**, *4*, 1922.

[230] W. Yang, X. Liu, X. Yue, J. Jia, S. Guo, *J. Am. Chem. Soc.* **2015**, *137*, 1436–1439.

[231] C. H. Lee, S. W. Rhee, H. W. Choi, *Nanoscale Res. Lett.* **2012**, *7*, 48.

[232] X. Li, Y. Liu, L. Fu, L. Cao, D. Wei, Y. Wang, *Adv. Funct. Mater.* **2006**, *16*, 2431–2437.

[233] A. Albanese, P. S. Tang, W. C. Chan, *Annu. Rev. Biomed. Eng.* **2012**, *14*, 1–16.

[234] A. Šarić, A. Cacciuto, *Phys. Rev. Lett.* **2012**, *108*, 118101.

[235] A. Šarić, A. Cacciuto, *Phys. Rev. Lett.* **2012**, *109*, 188101.

[236] M. Raatz, R. Lipowsky, T. R. Weikl, *Soft Matter* **2014**, *10*, 3570–3577.

[237] K. Xiong, J. Zhao, D. Yang, Q. Cheng, J. Wang, H. Ji, *Soft Matter* **2017**, *13*, 4644–4652.

[238] A. B. Petrova, C. Herold, E. P. Petrov, *Soft Matter* **2017**.

[239] A. Vahid, A. Saric, T. Idema, *Soft Matter* **2017**.

[240] A. Vahid, T. Idema, *Phys. Rev. Lett.* **2016**, *117*, 138102.

[241] J. A. Napoli, A. Šarić, A. Cacciuto, *Soft Matter* **2013**, *9*, 8881–8886.

[242] J. C. Pàmies, A. Cacciuto, *Phys. Rev. Lett.* **2011**, *106*, 045702.

Acknowledgements

I thank Prof. Dr. Gerhard Gompper for his kind support and guidance in my doctoral research. Special thanks go to Dr. Thorsten Auth, who provides great support in both scientific and daily life during my time in Juelich. Gratefully I acknowledge Dr. Sabyasachi Dasgupta (University of Toronto) for the suggestions and discussions for the calculations, and Dr. Kenneth Brakke (Susquehanna University) for his advice on Surface Evolver and numerical techniques. Thanks for the scientific help from my colleges, administrative help from Mrs. Meike Kleinen, and computing technique help from Mrs. Dorothea Henkel at Forschungszentrum Juelich. Finally, I would like to thank the thesis committee members (Prof. Dr. Gerhard Gompper, Prof. Dr. Jan K. G. Dhont, and Prof. Dr. Markus Braden) on their reviews and feedbacks on the thesis.

Ich versichere, daß ich die von mir vorgelegte Dissertation selbständig angefertigt, die benutzten Quellen und Hilfsmittel vollständig angegeben und die Stellen der Arbeit — einschließlich Tabellen, Karten und Abbildungen —, die anderen Werken im Wortlaut oder dem Sinn nach entnommen sind, in jedem Einzelfall als Entlehnung kenntlich gemacht habe; daß diese Dissertation noch keiner anderen Fakultät oder Universität zur Prüfung vorgelegen hat; daß sie — abgesehen unten angegebenen Teilpublikationen — noch nicht veröffentlicht worden ist sowie, daß ich eine solche Veröffentlichung vor Abschluß des Promotionsverfahrens nicht vornehmen werde. Die Bestimmungen der Promotionsordnung sind mir bekannt. Die von mir vorgelegte Dissertation ist von Prof. Dr. Gerhard Gompper betreut worden.

Jülich, den 22. Oktober 2017